2023-05-01

# Tibial-fibular morphology: variation, sexual dimorphism, and mechanical implications

Bruce, Olivia Leigh

UNIVERSITY OF CALGARY

# Tibial-fibular morphology: variation, sexual dimorphism, and mechanical implications

by

Olivia Leigh Bruce

A THESIS

SUBMITTED TO THE FACULTY OF GRADUATE STUDIES

IN PARTIAL FULFILMENT OF THE REQUIREMENTS FOR THE

DEGREE OF DOCTOR OF PHILOSOPHY

GRADUATE PROGRAM IN BIOMEDICAL ENGINEERING

CALGARY, ALBERTA

MAY, 2023

# Abstract

Stress fractures are common injuries among runners and military personnel associated with the mechanical fatigue of load-bearing bone. The tibia is the most frequently fractured site and females are at much greater risk than males. Bone geometry and density are hypothesized risk factors for stress fracture and are thought to contribute to the disparity in risk between sexes via their influence on bone strain magnitude which is strongly related to the rate of mechanical fatigue. However, covariation between these two complex factors and their influence on the strain environment of the tibia are not well characterised. The overarching goal of this thesis was to develop a more nuanced understanding of the mechanical implications of tibial-fibular geometry and density variations present in young active adults. A series of studies were performed utilizing a combination of advanced medical imaging, statistical approaches, gait data, and the finite element method to characterise and quantify covariations in whole-bone tibial-fibular geometry and density distributions and their influence on bone strain. Transverse diaphyseal geometry and sagittal curvature were identified as key features that likely influence stress fracture risk, demonstrating substantial effects on finite element-predicted bone strain. Additionally, the average female illustrated a narrower tibia which resulted in elevated bone strain when compared to the average male, suggesting that bone geometry likely contributes to the disparity in stress fracture risk between sexes. As we work towards improving predictive models and developing effective screening tools for stress fracture risk, these findings provide insights into key features of bone geometry and density that will need to be accurately characterised. Landmark- and anthropometric-based predictions of tibial-fibular geometry and density were not sufficiently accurate, indicating that some level of advanced medical imaging data will be necessary to generate personalized models or characterise geometry and density features associated with stress fracture risk.

# Preface

Chapters 3, 4, 5, and 6 are based on scientific manuscripts that are in preparation, submitted, or published.

Chapter 3 is based on:

> Bruce, O.L., Baggaley, M., Khassetarash, A., Haider, I.T., Edwards, W.B. (2022). Tibial-fibular geometry and density variations associated with elevated bone strain and sex disparities in young active adults. Bone. doi: 10.1016/j.bone.2022.116443
>
> *Statement of contributions*: OB and WBE conceived of the study design. MB and AK collected the data. ITH developed the finite element model. OB performed the analysis and wrote the manuscript with input from all authors. WBE supervised the research and provided critical feedback.

Chapter 4 is based on:

> Bruce, O.L., Edwards, W.B. Sex disparities in tibia-fibula geometry and density are associated with elevated bone strain in females: A cross- validation study. *In review at Bone.*
>
> *Statement of contributions*: OB and WBE conceived of the study design. OB collected the data. OB performed the analysis and wrote the manuscript. WBE supervised the research and provided critical feedback.

Chapter 5 is based on:

> Bruce, O.L., Baggaley, M., Welte, L., Rainbow, M.J., Edwards, W.B. (2021). A statistical shape model of the tibia-fibula complex: sexual dimorphism and effects of age on

reconstruction accuracy from anatomical landmarks. Computer Methods in Biomechanics and Biomedical Engineering. doi: 10.1080/10255842.2021.1985111

*Statement of contributions*: OB and WBE conceived the study design. MB collected the data. OB performed the analysis with input from LW and MJR. OB wrote the manuscript with input from all authors. WBE supervised the research and provided critical feedback.

Chapter 6 is based on:

Bruce, O.L., Tu, J., Edwards, W.B. Predicting tibia-fibula geometry and density from anatomical landmarks: influence of errors on finite element-calculated bone strain. *In preparation for submission to the Journal of Biomechanics.*

Statement of contributions: OB conceived the study design. OB and JT collected and processed the data. OB performed the analysis and wrote the manuscript with input from all authors. WBE supervised the research and provided critical feedback.

Ethics statement: Chapter 3 was covered by ethics certificate REB16-1475. Chapter 5 was covered by ethics certificates REB16-1475 under the project title "Computational modelling of stress-fracture injuries" and REB19-1845 under the project title "Internal loads during Groucho running, grounded running, and normal running: A subject-specific musculoskeletal model approach." Chapters 4 and 6 were covered by ethics certificate REB21-1971 under the project title "Statistical generation of participant-specific finite element models from sparse imaging data." All studies were approved by the University of Calgary Conjoint Health Research Ethics Board. All participants provided written, informed consent.

# Acknowledgments

First and foremost, I would like to thank my supervisor Dr. Brent Edwards for his outstanding mentorship, guidance, and commitment to my success. I am very thankful I was able to continue on in your lab for my PhD. You have fostered a positive environment within your group and provided unwavering support even through a global pandemic. I have learned and grown so much over the last 6.5 years and will be forever grateful for the opportunities and mentorship you provided.

There are many individuals who have also contributed to my academic training and the success of projects during this degree. Thank you to my supervisory committee Dr. Steve Boyd and Dr. Art Kuo for your guidance, always constructive feedback, and thought-provoking questions. To Dr. Ifaz Haider, your expertise in all things finite element was instrumental to the successful development of the analysis workflows. Thank you for your patience, enthusiasm, and mentorship. To Dr. Mike Rainbow and Dr. Lauren Welte, thank you for sharing your shape modelling expertise and the virtual happy hours. I would also like to thank Dr. Renaud Léguillette and the Calgary Stampede for the opportunity to be involved in a very fun project for my We-TRAC practicum.

To past and present lab mates, officemates, and friends in the HPL, thank you for making the lab such a pleasant place to work. It has been inspiring to be surrounded by so many bright scientists. Thank you for your friendship and support. A special thank you to Michael Baggaley and Monica Russel for the many insightful conversations and for listening to me stress out on a semi-regular basis.

Finally, thank you to my mother, father, and sister for their unending emotional support and encouragement. It means so much that you have always supported my interest in science and my decision to pursue graduate degrees, though the many highs and lows that has entailed.

# Table of Contents

# List of Tables

# List of Figures

# List of Symbols and Nomenclature

| | |
|---|---|
| 2D | Two-dimensional |
| 3D | Three-dimensional |
| $\varepsilon$ | Strain |
| $\varepsilon_{vol}$ | Strained volume |
| $\eta^2$ | Partial eta squared |
| $\lambda$ | Eigenvalue |
| $\mu\varepsilon$ | Microstrain |
| $\nu$ | Poisson's ratio |
| $\vec{\nu}$ | Eigenvector |
| $\rho_{app}$ | Apparent density |
| $\rho_{HU}$ | CT equivalent density |
| $\sigma$ | Standard deviation |
| $\varphi$ | Matrix of principal component coefficients (eigenvectors) |
| $\chi^2$ | Chi squared test statistic |
| ANOVA | Analysis of variance |
| BFGS | Broyden–Fletcher–Goldfarb–Shanno algorithm |
| BMC | Bone mineral content |
| BMD | Bone mineral density |
| C | Covariance matrix |
| cm | Centimetre |
| CT | Computed tomography |
| Dmp1 | Dentin matrix acidic phosphoprotein 1 |
| DXA | Dual-energy X-ray absorptiometry |
| E | Modulus of elasticity |
| F | F-statistic |
| FE | Finite element |

| | |
|---|---|
| g | Grams |
| G | Shear modulus |
| GPa | Gigapascal |
| HR-pQCT tomography | High-resolution peripheral quantitative computed |
| HU | Hounsfield unit |
| Hz | Hertz |
| I | Identity matrix |
| IQR | Interquartile range |
| kg | Kilograms |
| kVp | Kilovoltage peak |
| m | Metres |
| mA | Milliamps |
| MEPE | Gene that encodes for matrix extracellular phosphoglycoprotein |
| mm | Millimetre |
| MPa | Megapascal |
| MRI | Magnetic resonance imaging |
| MSK | Musculoskeletal |
| N | Newtons |
| $N_f$ | Fatigue life |
| p | p-value |
| PCA | Principal components analysis |
| PC | Principal component |
| pQCT | Peripheral quantitative computed tomography |
| $r^2$ | Coefficient of determination |
| RED-S | Relative energy deficiency in sport |
| RMSE | Root mean square error |
| s | Seconds |

| | |
|---|---|
| SAM | Statistical appearance model |
| SD | Standard deviation |
| SSM | Statistical shape model |
| t | t-statistic |
| $W_s$ | Weighting factor to normalise node/density scores |
| $\bar{x}$ | Mean shape and/or density |

# Chapter 1

# Introduction

## 1.1 Rationale

Stress fractures are common overuse injuries experienced by runners and military personnel, with an incidence of 3-20% (Bennell et al. 1996; Hame et al. 2004; Shaffer et al. 2006). These fractures develop as a result of repetitive loading and typically occur following a sudden increase in training volume (Kardouni et al. 2021; Hoenig et al. 2022). The tibia is the most common bone affected, accounting for 20-63% of all stress fractures (Matheson et al. 1987; Brukner & Bennell 1995; Bennell et al. 1996). Notably, female runners are at two to three times greater risk and female military recruits are at up to four times greater risk of stress fracture when compared to males (Bennell et al. 1996; Changstrom et al. 2015; Kardouni et al. 2021). Stress fractures require months for recovery to return to sport and a history of stress fracture is a major risk factor for future fracture (Pegrum et al. 2012; Wood et al. 2014). Consequently, prevention is of great interest.

Stress fracture development has been associated with mechanical fatigue, a phenomenon wherein repetitive submaximal loading results in the accumulation of microdamage (Burr et al. 1990). Microdamage is associated with reduced stiffness of bone tissue, resulting in increased strain for a given stress magnitude in subsequent loading cycles, thereby accelerating the accumulation of damage (Bennell 1996; Pattin et al. 1996). Over time, when the rate of damage

accumulation is chronically greater than the rate of repair, a fracture may eventually occur. Strain is the key mechanical parameter associated with the accumulation of microdamage in bone (Pattin et al. 1996). The relationship between strain magnitude and fatigue life is well described by an inverse power law, the slope of which indicates that small changes in strain result in much larger changes in fatigue life (Carter et al. 1981a).

Bone strain is a complex function of bone geometry, density distribution, material properties, and applied loads. Bone geometry and density are hypothesized to be risk factors for stress fracture and to contribute to the disparity in risk between females and males (Hoenig et al. 2022). Differences in transverse cross-sectional geometry and density parameters have previously been observed between stress fracture cases and controls and between females and males (Beck et al. 2000; Koltun et al. 2022), but these investigations were limited to two-dimensional measures. Furthermore, evaluation of the mechanical implication of these differences has been limited to simple estimates of bone strength. Tibial-fibular geometry and density distribution variation in young active adults has not yet been characterised. Understanding how geometry and density features vary within this population and quantifying the influence of these variations on bone strain is an important step in understanding how bone geometry and density influence stress fracture risk and identifying which features are most important to guide future screening and prevention efforts.

Direct measurement of local strain is achieved through surgical implantation of strain gauges or staples onto/into the bone (Yang et al. 2011). This method is invasive and not feasible for regular use in research laboratories or clinical settings. Alternatively, bone strain may be estimated using a combination of biomechanical experimentation, advanced medical imaging data, and participant-specific finite element modeling. This approach has been used to estimate bone deformations in line with experimental measurements (Haider et al. 2020), but can be time-

consuming, costly, and requires computed tomography (CT) imaging to obtain participant-specific bone geometry and material properties (Poelert et al. 2013). Furthermore, it can be difficult to isolate or identify the specific features in bone geometry or density that are driving differences in finite element-predicted bone strain between individuals or groups.

Statistical models may provide a method to address these limitations. Statistical shape and appearance models calculate the average and principal modes of variation in bone geometry and density distribution (Cootes & Taylor 2004). The model can then be used to identify which features differ between groups (e.g., sexes) and be used in combination with the finite element method to parametrically explore the influence of geometry and density distribution variations on bone strain *in silico*. There has also been interest in using statistical shape models to predict participant-specific bone geometry in the absence of medical imaging data (Zhang et al. 2016; Suwarganda et al. 2019); however, it is currently unknown if this approach would characterise bone geometry and density distribution with sufficient accuracy to obtain bone strain estimates similar to the current state-of-the-art CT-based method.

The research presented in this thesis utilized a combination of statistical shape and appearance modeling, biomechanical data, and the finite element method to characterise tibial-fibular geometry and density variations, errors due to anthropometric data-based prediction approaches, and their mechanical implications in young active adults. The findings from these studies offer new insights into bone geometry and density distributions as risk factors for stress fracture and the methods necessary to accurately characterise these factors for use in predictive modeling approaches.

## 1.2 Objective and Specific Aims

The overarching objective of this thesis was to develop a more nuanced understanding of the mechanical implications of tibial-fibular geometry and density variations present in young active adults. More specifically, the thesis aimed to answer:

1. How do geometry and density distributions vary in young healthy adults? (Chapters 3, 4, and 5)
2. How do geometry and density distributions vary between sexes in young healthy adults? (Chapters 3, 4, and 5)
3. To what degree do geometry and density distribution variations and sexual dimorphism influence finite element-calculated bone strain? (Chapters 3 and 4)
4. Can participant-informed models be accurately generated using statistical shape and appearance models in the absence of medical imaging data and what are the errors associated with this approach? (Chapters 5 and 6)

Four studies were preformed to address these questions.

The first study aimed to characterise tibial-fibular geometry and density variations using a statistical appearance model and to quantify the influence of these variations on finite element-predicted bone strain in young, active adults. I hypothesized that transverse cross-sectional geometry would demonstrate the largest influence on bone strain and that the average female would illustrate greater bone strain when compared to the average male. I developed the statistical appearance model from a training set of twenty females and twenty-eight males. I generated finite element models representing ±1 and 2 standard deviations along each of the first five principal components and representing the average female and average male controlled for allometric

scaling. The study identified key variations that exerted a large influence on bone strain and added support to the hypothesis that sexual dimorphism influences stress fracture risk.

The second study aimed to cross-validate the first study's findings of sex-related differences in tibial-fibular bone geometry, density, and finite element-predicted bone strain. An entirely new cohort of fifteen females and fifteen males were recruited. Finite element models of the average female and average male, controlled for allometric scaling, were generated. The study confirmed that the average female illustrates greater strain due to a narrower tibia.

The third study aimed to evaluate the accuracy of tibial-fibular complex reconstructions from anatomical bony landmarks using a statistical shape model developed for a healthy, young adult population and quantify the subsequent effects on muscle moment arms. The secondary objectives of this study were (1) to quantify sex differences in bone geometry, and (2) to evaluate the generalizability of the developed young adult statistical shape model to older adults. I hypothesized that reconstruction errors would be smaller for the statistical shape model-generated geometries compared to isotropic scaling and that errors would be larger for the older adults. I developed the statistical shape model from a training set of twenty females and nineteen males. Tibia and fibula geometry were predicted from anatomical landmarks identified on the bone surface and compared to CT-quantified geometry. The results confirmed my hypotheses. However, only three muscle moment arms were affected, to a small degree, by the improved accuracy when compared to allometric scaling of the average geometry.

The fourth study aimed to (1) quantify errors associated with predicting tibial-fibular geometry and density distributions from anatomic landmarks and to (2) quantify how those errors propagate to finite element-estimated bone strain. I predicted tibial-fibular geometry and density distributions from skin-mounted landmarks using the statistical appearance model developed in

Chapter 3 and from height and sex. Errors in finite element-estimated bone strain associated with geometry and density prediction errors were quantified. Landmark-based predictions did not improve accuracy when compared to predictions from height and sex. Both prediction methods produced large errors in bone strain, indicating that medical imaging is necessary to avoid significant errors due to inter-individual bone geometry variations.

## 1.3 Presentation of the Thesis

The content of this thesis is organized as follows: Chapter Two summarizes the relevant literature and background information including stress fracture pathophysiology, *in vivo* measurement and *in silico* calculation of bone strain, and statistical shape and appearance modeling. Chapters Three through Six address the specific aims outlined in section 1.2 of this thesis. Each of these chapters are written as independent manuscripts. As such, some sections will contain redundant information. The study presented in Chapter Three characterised tibial-fibular geometry and density distribution variations and sexual dimorphism, and evaluated the influence of these variations on finite element-predicted bone strain. The study presented in Chapter Four cross-validated sex-related variations and their influence on bone strain. The studies presented in Chapters Five and Six evaluated errors associated with predicting whole bone geometry and density distribution in the absence of medical imaging and their mechanical implications. Chapter Seven synthesizes the findings of the studies and discusses implications and future directions.

# Chapter 2

# Background

## 2.1 Bone hierarchical structure, cells, and functions

Bone is organized in a hierarchical structure (Figure 2.1). At the nanoscale cross-linked Type I collagen fibrils are mineralized with carbonated apatite to form collagen fibers where the collagen serves to provide toughness, while the mineral component contributes to the stiffness of the material (Burr 2019). At the microscale these fibers are arranged in lamellar sheets with alternating orientations, laid down at the periosteal, endosteal, and trabecular surfaces to form primary lamellar bone (Reznikov et al. 2014). Lamellae are also laid down concentrically within large vascular channels to form primary osteons (Rho et al. 1998). Secondary bone results from remodeling, where existing bone is resorbed and new bone is deposited in concentric sheets to form secondary osteons (a.k.a., Haversian systems) surrounded by cement lines (Burr 2019). Osteons are approximately oriented along the long axis of the bone, contributing to the highly anisotropic properties of the material (Doblaré et al. 2004). At the macroscale, bone tissue is organized into dense cortical bone or very porous trabecular bone (also called cancellous bone) (Rho et al. 1998).

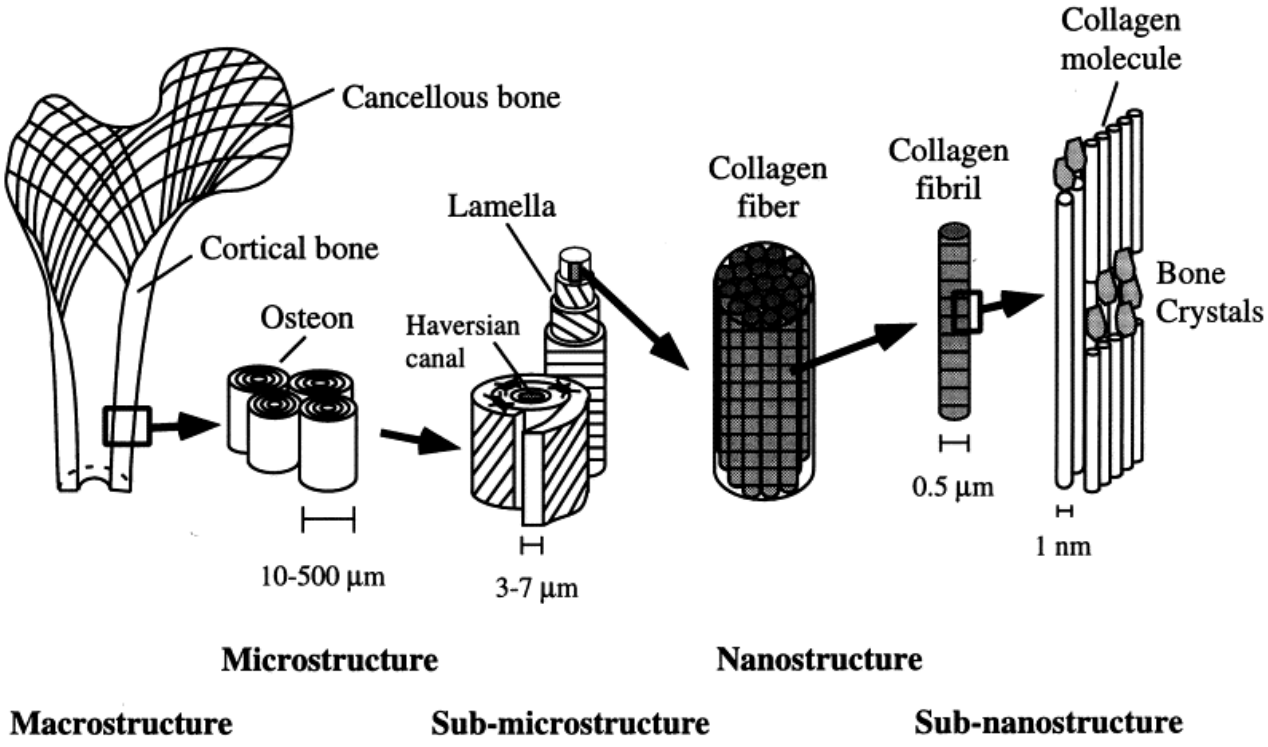


*Figure 2.1 Hierarchical structure of bone across scales. Reproduced with permission (Rho et al. 1998)*

There are four types of bone cells: osteoclasts, osteoblasts, osteocytes, and lining cells. Osteoclasts originate from hematopoietic stem cell populations and resorb bone (Bellido et al. 2019). When resorption is complete osteoclasts undergo programmed cell death (apoptosis) (Majeska 2001). Osteoblasts originate from skeletal stem cell populations in the bone marrow and periosteum and form bone. Specifically, osteoblasts produce the organic components of the bone matrix called osteoid and facilitate mineral deposition (Majeska 2001). When bone formation is complete osteoblasts either undergo apoptosis or become osteocytes or lining cells (Bellido et al. 2019). Osteoblasts that become surrounded by bone tissue during deposition differentiate into osteocytes (Bellido et al. 2019). Osteocyte lacunae are connected via tunnels called canaliculi to enable communication between cells through their dendritic processes and gap junctions

(Schneider et al. 2010). Osteocytes account for approximately 90% of the cells in bone and together coordinate osteoclast and osteoblast action in response to mechanical and hormonal cues (Bellido et al. 2019). Finally, some osteoblasts on bone surfaces flatten to become lining cells. These cells communicate with osteocytes in the bone matrix and play a role in the regulation of calcium exchange between mineralized bone and bone marrow (Bellido et al. 2019).

Bone serves a variety of functions. The first one that likely comes to mind is bone's role in the musculoskeletal system, providing structure, support, and levers on which muscles pull to produce movement. Bone also provides protection for our internal organs by absorbing and dissipating energy from impacts while minimizing damage to itself and the underlying soft tissues (Burr 2019). Other functions of bone include mineral homeostasis, hematopoiesis, and endocrine regulation.

## 2.2 Bone growth and development

Bones develop through the processes of intramembranous and endochondral ossification. Intramembranous ossification is the process by which mesenchymal stem cells differentiate directly into osteoblasts and lay down bone in sheets (Allen & Burr 2019). In endochondral ossification, which is responsible for the development and growth of long bones, mesenchymal stem cells differentiate first into chondrocytes to form a hyaline cartilage template that is gradually replaced by bone (Hall 2015). The shape of the template is genetically controlled (Chalmers & Ray 1962; Hall 2015). A membrane with a network of blood vessels surrounds the cartilage template, supplying nutrients, removing waste, and bringing osteoblasts to the edges of the template. The osteoblasts deposit bone in a ring around the edges of the cartilage template, which prevents diffusion of nutrients to the center and results in chondrocyte death. Blood vessels then invade the spaces left by the dead chondrocytes, expanding the spaces, and delivering osteoblasts

to the primary ossification center in the middle of the forming bone. Cartilage continues to grow at both ends of the template with ossification following, increasing the bone's length. After birth, secondary ossification centers are established at the epiphyses, separated from the metaphysis and diaphysis regions by the physis (i.e., the growth plate) (Hall 2015; Allen & Burr 2019). During childhood and adolescence, new cartilage forms in the growth plate, which is then mineralized on the metaphysis side and eventually replaced with bone, extending the length axially. This process continues until the growth plate closes, becoming ossified (Ballock & O'Keefe 2003). The timing of the closure depends on the location of the growth plate and follows a genetically determined order (Ballock & O'Keefe 2003; Martin et al. 2015).

During growth, bone shape is adjusted through the process of modeling, where osteoblasts and osteoclasts act independently to form bone in some areas and remove bone in others (Martin et al. 2015; Allen & Burr 2019). In bones with ends that flare outward such as the tibia, modeling occurs at the metaphysis as the bone lengthens to preserve the correct bone shape (Martin et al. 2015). Bone formation on the periosteal surface and resorption on the endosteal surface acts to expand the diameter of the bone (Allen & Burr 2019). Adaptation of bone geometry and transverse size in response to mechanical loading is also accomplished through modeling, although it is reduced after skeletal maturity is reached (Bass et al. 2002; Martin et al. 2015).

Remodeling involves the removal and re-formation of bone at a site via the coupled actions of osteoclasts and osteoblast following the sequence: activation-resorption-reversal-formation (Martin et al. 2015). In the activation phase, lasting three to five days, osteoclast precursors are recruited to the remodeling site and differentiate into mature osteoclasts (Allen & Burr 2019). The resorption phase is characterised by osteoclast resorption of bone and lasts approximately three

weeks. This is followed by a short reversal period lasting a few days followed by bone formation in concentric layers by osteoblasts over a period of three to four months (Allen & Burr 2019). Approximately ten days after new unmineralized bone matrix is deposited, mineralization of the new tissue begins. Full mineralization of the new material can take up to one year (Fuchs et al. 2008). Remodeling occurs throughout life and plays a role in microdamage repair and mineral homeostasis (Martin et al. 2015).

## 2.3 Strain and Bone Health

Bone is a dynamic tissue that adapts to its mechanical loading environment. Bone strain, or some consequence thereof (microdamage, fluid flow, strain energy density), is thought to be the key mechanical parameter influencing the adaptive process (Klein-Nulend et al. 2013; Bhatia et al. 2015). Experiments using animal models have demonstrated that short durations of high strain, dynamic loading produced large osteogenic effects (Rubin & Lanyon 1985; Turner 1998; Robling et al. 2002). This has been supported indirectly in humans. Athletes training in sports characterised by periodic, large loads (e.g., gymnastics) have greater bone mineral density (BMD) compared to sports characterised by repetitive, lower loads (e.g., cycling, running) and sedentary individuals (Fehling et al. 1995; Pettersson et al. 2000). Exercise intervention studies have also observed changes in trabecular bone quality measures and bone mineral density (BMD) in as little as eight weeks (Bhatia et al. 2015; Hughes et al. 2018).

Osteocytes are thought to be the primary mechanosensory cells associated with adaptation (Qin et al. 2020). Loading is associated with down regulation of sclerostin and upregulation of Dmp1 and MEPE, all of which are produced by osteocytes (Harris et al. 2007; Robling et al. 2008). Sclerostin is an antagonist for the pathway leading to osteoblast differentiation and dentin matrix

acidic phosphoprotein 1 (Dmp1) and matrix extracellular phosphoglycoprotein (MEPE) promote mineralization (Li et al. 2005; Harris et al. 2007). Interestingly, the mechanosensory signal for adaptation appears to saturate quickly with repeated loading cycles. For example, one study observed no difference in bone formation between limbs loaded 36 or 1800 cycles per day (Rubin & Lanyon 1984). Animal models suggest that the adaptive response saturates after 100-400 cycles depending on the strain magnitude and takes four to eight hours to fully recover sensitivity (Umemura et al. 1997; Robling et al. 2001; Robling et al. 2002). Practically, this means that just a few minutes of impulsive high magnitude loading such as jumping can lead to an adaptive response, but the response plateaus quickly during highly repetitive activities such as running (Vlachopoulos et al. 2018; Warden et al. 2021a).

At the material level, strain is also the primary factor driving mechanical fatigue. Mechanical fatigue is a phenomenon wherein repetitive submaximal loading results in the accumulation of microdamage in the form of diffuse damage and microcracks (Burr et al. 1997). Characterised by a loss of stiffness and strength due to the accumulation of damage, mechanical fatigue is influenced by strain magnitude and the number of loading cycles (Carter et al. 1981a; Pattin et al. 1996; Edwards 2018). In bone, the relationship between strain magnitude ($\varepsilon$) and the number of cycles to failure ($N_f$) is well described by an inverse power law (Figure 2.2):

$$N_f = A\varepsilon^{-b} \tag{2.1}$$

where $A$ is a constant and $b$ is the slope of the strain-life curve (Carter et al. 1981a; Edwards 2018). Thus, strain magnitude has a much greater effect on the accumulation of damage than the number of cycles.

A great degree of scatter is observed in experimental measures of fatigue life (Figure 2.2, Carter et al. 1981; Taylor 1998). A significant proportion of this scatter can be explained by stressed/strained volume (Taylor 1998; Taylor et al. 1999; Loundagin et al. 2021). Bone exhibits a statistical size effect, wherein a larger volume of bone tends to illustrate a shorter fatigue life when compared to smaller samples loaded to the same strain magnitude (Bigley et al. 2007). A larger volume is more likely to contain an area of microstructural weakness or a critical flaw, increasing the probability of failure (Taylor 1998). Strained volume is influenced by variations in intracortical microarchitecture. Vascular and resorption canals act as strain concentrators, substantially amplifying local strains far above the overall strain of the bone sample (Nicolella et al. 2005; Nicolella et al. 2006). In particular, canal diameter has a strong influence on stressed/strained volume where increased diameter results in greater stress concentrations and stressed/strained volume (Loundagin & Edwards 2020; Loundagin et al. 2021).

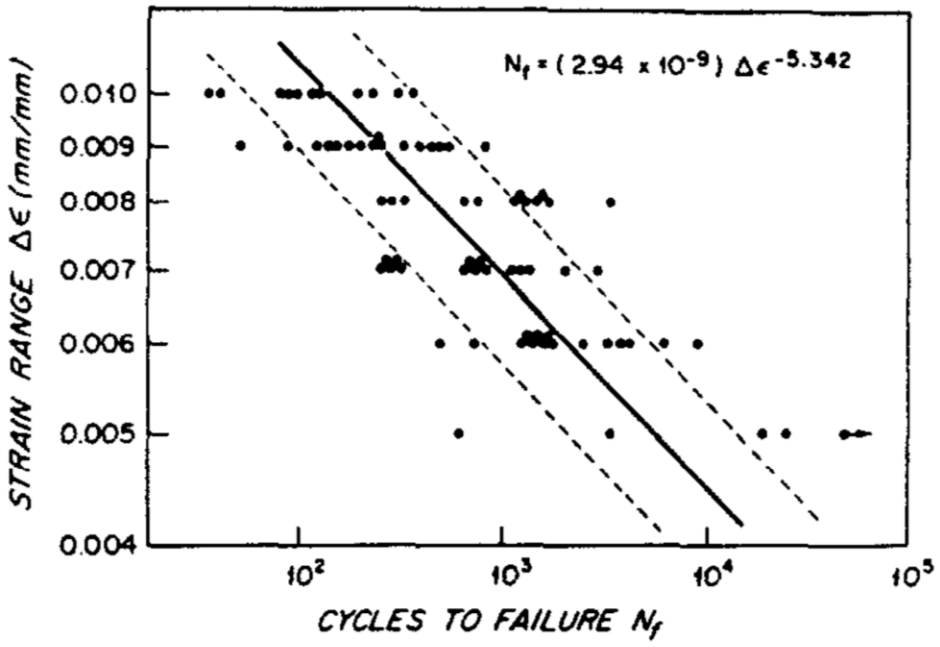


*Figure 2.2 Influence of cyclic strain range on the number of cycles to fatigue failure. Reproduced with permission* (Carter et al. 1981b)

## 2.4 Stress Fracture

Stress fracture is a common overuse injury in runners and military personnel, with incidence of 3-20% (Bennell et al. 1996; Hame et al. 2004; Shaffer et al. 2006). These fractures develop as a result of repetitive loading applied to a generally normal bone and typically occur following a sudden increase in training volume (Kardouni et al. 2021; Hoenig et al. 2022). In military recruits, incidence peaks between three and eight weeks following the beginning of basic training (Kardouni et al. 2021). Athletes tend to be at higher risk during the pre-season or transition to competition season (Rizzone et al. 2017; Khan et al. 2018). Stress fractures present clinically as pain and localized tenderness when loaded (Fredericson et al. 1995; Gmachowska et al. 2018). Magnetic resonance imaging (MRI) may be used to confirm the presence of oedema and a fracture line (Kijowski et al. 2012; Nattiv et al. 2013). When oedema is present but a fracture line is not, the injury is classified as a stress reaction, a lower grade of bone stress injury (Nattiv et al. 2013).

Common stress fracture locations vary by sport. Stress fractures occur in the ribs of rowers and kayakers, at the lumbar spine in gymnasts and football linemen, and at the upper limb in pitchers and para-athletes who use wheelchairs (Tenforde et al. 2019; Hoenig et al. 2022). In runners and military personnel the tibia is the most common bone affected , accounting for 20-63% of all fractures, followed by the metatarsals, other tarsals, pelvis, fibula, and femur (Matheson et al. 1987; Brukner & Bennell 1995; Bennell et al. 1996). Tibial stress fractures occur most frequently on the posterior aspect of the tibial diaphysis, followed by the medial aspect (Kijowski et al. 2012). Fracture locations are approximately evenly spread across the axial length of the diaphysis (Fredericson et al. 1995). Anterior tibial stress fractures can occur but are more common in athletes performing repetitive jumping than in runners (McInnis & Ramey 2016). Anterior

fractures are considered high risk as they are located at a site with high tensile stresses and are thus more prone to delayed union and complete fracture (Murray et al. 2006; McInnis & Ramey 2016).

Treatment of stress fractures depends on the location and severity, but typically requires a period of rest and some degree of physical activity restriction to allow for healing, followed by gradual return to activity (Pegrum et al. 2012; Warden et al. 2021b). The long recovery period (10-47 weeks) may result in an athlete missing a season and significant declines in fitness. The economic burden resulting from the cost of treatment and missed games or competitions is substantial (Pegrum et al. 2012). Similarly, the economic burden of stress fractures in British military recruits has been estimated at £1500 per recruit per week, or £1.2 million (2 million CAD) per year (Wood et al. 2014).

### *2.4.1 Pathophysiology*

The pathophysiology of stress fracture is not fully understood but is generally thought to result from a chronic imbalance between mechanical fatigue and bone cellular repair. As discussed in Chapter 2.3, mechanical fatigue is a phenomenon wherein submaximal repetitive loading results in the accumulation of microdamage in the form of small cracks in the bone matrix (Burr et al. 1990). Microdamage is associated with reduced stiffness of the bone tissue, resulting in increased strain for a given stress magnitude in subsequent loading cycles, thereby accelerating the accumulation of damage (Bennell 1996; Pattin et al. 1996). Microdamage is also associated with osteocyte apoptosis, which stimulates the remodeling process to repair damage, but this process takes time (Herman et al. 2010). When the rate of microdamage is chronically greater than the rate of repair, microcracks may grow to a critical length or coalesce and result in a fracture (Bennell 1996). An imbalance between microdamage accumulation and cellular repair could result from

increased damage due to greater training loads associated with increased strain, elevated resorption associated with low energy availability and hormonal disturbances, or the combination of the two (Burr et al. 1990; Papageorgiou et al. 2017).

A prevalent alternate hypothesis posits that targeted remodeling is a central factor contributing to the imbalance between mechanical fatigue and repair, and thus the development of stress fractures *in vivo*. Following the initiation of remodeling, bone is resorbed by osteoclasts over a period of approximately three weeks before bone formation begins (Allen & Burr 2019). Thus, a sudden increase in remodeling leads to a transient increase in porosity, which may weaken the bone, increase strain, and lead to a destructive feed-forward loop (Burr et al. 1997; Warden et al. 2021a; Hoenig et al. 2022). In fact, resorption canals are large (200-300 με) and would therefore have a disproportionately negative effect on fatigue life (Cooper et al. 2016; Lassen et al. 2017; Loundagin & Edwards 2020). This hypothesis may align with the time frame for the development of stress fractures observed *in vivo* (Kardouni et al. 2021; Warden et al. 2021a). However, temporarily suppressing bone remodeling using bisphosphonates at the beginning of infantry basic training did not reduce stress fracture incidence when compared to placebo (Milgrom et al. 2004). It is possible that there are multiple conditions in which an imbalance between microdamage accumulation and repair exist: elevated remodeling may accelerate the accumulation of damage, supressed remodeling may fail to repair microdamage, or microdamage formation may simply outpace normal bone repair (Milgrom et al. 2004).

### *2.4.2 Risk factors*

Prospective and retrospective cross-sectional studies have identified a myriad of risk factors associated with stress fracture. These risk factors generally share a common thread: they

ultimately affect the strain environment of bone by influencing the applied loads, bone mass and quality, and/or remodeling. Indeed, bone geometry and density themselves have been identified as risk factors for stress fracture (Beck et al. 2000; Popp et al. 2020). Type of sport, stage of training, and biomechanical variables such as cadence/step length, rearfoot eversion, and leg-length discrepancy influence the loads applied to the bone (Bennell et al. 1999; Milner et al. 2006; Rizzone et al. 2017; Kliethermes et al. 2021). Physical activity history, early sport specialization, genetic variation, and nutritional deficiencies affect bone mass and/or quality (Milgrom, Simkin, et al. 2000; Lappe et al. 2008; Nieves et al. 2010; Bulathsinhala et al. 2017; Warden et al. 2021a). Relative energy deficiency in sport (RED-S) is a major risk factor for stress fracture, influencing bone mass, microarchitecture, and remodeling (Mountjoy et al. 2014). Sex is another notable risk factor for stress fracture; female runners are two to three times more likely to sustain a stress fracture than men and female military recruits are up to four times more likely to sustain a fracture than their male colleagues (Bennell et al. 1996; Changstrom et al. 2015; Kardouni et al. 2021). Bone mass and quality may vary between sexes (discussed in the next section) (Beck et al. 2000). In addition, low energy availability and hormonal disturbances are more prevalent in females when compared to males (Mountjoy et al. 2014). Finally, history of stress fracture is a strong predictor of future fracture (Wright et al. 2015). Recurring stress fractures typically occur at new sites either within the previously fractured bone or a different bone altogether (Bennell & Brukner 1997; Hoenig et al. 2022).

### *2.4.3 Tibial-fibular sexual dimorphism*

It has been hypothesized that sex-related differences in the transverse geometry of the tibia may contribute to the disparity in stress fracture risk between sexes. Investigations of two-dimensional cross-sections obtained using peripheral quantitative computed tomography (pQCT)

or dual-energy x-ray absorptiometry (DXA) at discrete sites along the tibial diaphysis demonstrate that females illustrate smaller transverse size relative to body size when compared to males (Nieves et al. 2005; Tommasini et al. 2007). Specifically, cortical area, section modulus normalised to bone length or height, and simple estimates of bone strength were smaller in females than in males (Beck et al. 2000; Smock et al. 2009; Sherk et al. 2012; Koltun et al. 2022). In addition, cortical density may be higher in females (Beck et al. 2000; Sherk et al. 2012), but some cohorts illustrated no difference between sexes (Nieves et al. 2005). Three-dimensional analyses of tibial periosteal shape report additional geometric variations between sexes not captured by two-dimensional transverse diaphyseal cross-sections: greater protrusion of the tibial tuberosity, diaphyseal curvature, condyle size, and metaphyseal slope illustrated by females when compared to males (Mahfouz et al. 2012; Brzobohatá et al. 2015; Brzobohatá et al. 2016; Audenaert et al. 2019; Tümer et al. 2019). Neither sex differences in density distribution or the influence of geometry and density differences on the strain environment of the tibia have been investigated.

## 2.5 *In vivo* measurement of Bone Strain in Humans

In humans, direct measurement of bone strain and deformation *in vivo* requires invasive methods: strain gauges (Lanyon et al. 1975; Burr et al. 1996; Milgrom et al. 1996), instrumented staples (Rolfe et al. 1997; Fyhrie et al. 1998; Ekenman et al. 1998; Milgrom 2000; Ekenman et al. 2002; Milgrom et al. 2003), or bone screws (Yang et al. 2014) surgically inserted onto or into the bone. Early studies used strain gauges, the standard measurement tool for strain in tests of engineering materials (Lanyon et al. 1975; Burr et al. 1996; Milgrom et al. 1996). Strain gauges are glued to the surface of the bone after removing the periosteum. It is important to achieve adequate bonding of the strain gauge to the bone to avoid data loss, but this can be difficult in a biological environment (Burr et al. 1996; Yang et al. 2011). Instrumented staples, secured in pre-

drilled holes in the cortex of the bone, address this limitation and have since been used in a number of studies (Rolfe et al. 1997; Ekenman, Halvorsen, Westblad, Fellander-Tsai, et al. 1998; Fyhrie et al. 1998; Milgrom et al. 2000; Ekenman et al. 2002; Yang et al. 2011). These *in vivo* strain measurement methods provide a direct measure of local strain. However, strain varies throughout the bone and local measurements may not reflect the strain experienced by the bone (Yang et al. 2011). Furthermore, strain gauges and staples can only be attached to the bone in areas close to the skin surface (ex. the anteromedial tibia) (Yang et al. 2011). Stress fractures in the tibia often occur on the posterior aspect of the bone (Komatsu et al. 2019), but attachment of a strain gauge or staple is not possible in this location without disturbing or damaging the surrounding muscles. More recently, bone screws were used to obtain global measures of tibia deformation (Yang et al. 2014). The screws were implanted into pre-drilled holes at multiple locations in the bone and optical motion capture data were used to measure global anterior-posterior and medial-lateral bending, and torsion in the tibia during walking and running. This approach provided measures of overall deformation, but not localized measures of bone strain.

While these methods provide direct measures of bone strain or deformation, they are invasive and involve risk of infection. As a result, studies typically involve few participants and test conditions. Measurements are limited to local strain or global deformation. The distribution of strains across the tibia are likely different across individuals and activities, but cannot be measured using strain gauges, staples, or screws. Given these limitations, modeling approaches are becoming more common (Schipilow et al. 2013; Bhatia et al. 2015; Firminger et al. 2017).

## 2.6 Computational Modeling Approaches

The current state-of-the-art modeling approach for estimating bone strain *in vivo* involves generating a participant-specific finite element model from advanced medical imaging with

boundary conditions obtained from biomechanical measurements and simulations of the movement of interest. The finite element method is a useful approach for estimating stress and strain in problems with complex geometries, loads, and/or material properties (Martin et al. 2015). CT data are used to define the geometry and material properties of the object(s) of interest, in this case the tibia and fibula. Meshes of the bones made up of connected discretized elements are created from segmented CT images (Martin et al. 2015). A convergence analysis is typically performed to determine the size of the elements such that refining the mesh further, i.e., using smaller element sizes, does not significantly change (usually a threshold of < 5%) bone strain predictions. After meshing, an apparent density value is assigned to each element based on the underlying CT data using a linear relationship between Hounsfield units (i.e., image intensity) and CT equivalent density established using a phantom with known densities included in each scan. Material properties are then assigned to each element, usually based on published relationships between apparent bone density and elastic modulus. These properties inform the partial differential equations that govern the behavior of the elements (Dalstra et al. 1993; Austman et al. 2008). In the model used in this thesis, the elastic modulus in the axial direction was calculated using the apparent density of the element and the elastic constants in the medial-lateral and anterior-posterior directions were calculated assuming constant orthotropy throughout the bone (Rho 1996). This definition showed strong agreement between experimentally measured and FE-predicted strains for a cadaveric tibia when loaded in compression, bending, and torsion (Gray et al. 2008).

The analysis approximates a solution to the set of partial differential equations governing the behavior of the elements such that specified boundary conditions (e.g., applied forces and fixed points) are satisfied to estimate stress and strain distributions throughout the bone (Martin et al. 2015). A variety of constraints have been used in recent literature, from simple set-ups where the

distal portion of the tibia is fixed and an axial load is applied at the tibial plateau to very complex set-ups allowing some movement at joints and including muscle forces (Edwards et al. 2010; Xu et al. 2016; Hadid et al. 2018; Haider et al. 2020). Haider et al. (2020a) compared finite element-predicted tibial bending between models with different boundary conditions and to *in vivo* measures reported in the literature (Yang et al. 2014). They found that inclusion of the fibula was necessary to predict realistic tibial bending. Furthermore, the most complex model incorporating a pinned constraint allowing some rotation at the ankle joint, simulated ligaments allowing some movement at the proximal tibia-fibula joint, muscle forces, and a residual moment accounting for forces otherwise excluded from the model (e.g., the moment produced by the gastrocnemius muscles that do not insert into the tibia) produced realistic tibial bending predictions closest to *in vivo* measurements.

The muscle and joint contact forces applied as boundary conditions are typically calculated using a musculoskeletal (MSK) model and experimentally measured motion and ground reaction force data. The complexity and participant-specificity of the MSK model can vary from generic two-dimensional models to complex three-dimensional models incorporating participant-specific bone geometries and/or muscle properties (Scott & Winter 1990; Seth et al. 2018). Most commonly, MSK models are constructed from generic skeletal geometries and muscle parameters that are scaled using a participant's segment lengths and mass (Vaughan et al. 1999; Arnold et al. 2010; Edwards et al. 2010; Wang et al. 2016; Seth et al. 2018). Less commonly, participant-specific bone geometries quantified from CT, magnetic resonance imaging (MRI), or statistical models have been used (Martelli et al. 2015; Hughes et al. 2019). Using participant-specific geometries may reduce errors in joint center and muscle attachment locations, muscle moment arms, and joint contact forces (Scheys et al. 2008; Martelli et al. 2015; Xu et al. 2020). The

participant-specific approach is far less common because it requires advanced medical imaging and a significant amount of time and expertise to personalize bone geometries, alignments, and/or muscle properties. However, tools to automate and streamline the generation of personalized models are being developed and may improve the feasibility of personalizing bone geometries in MSK models in the future (Zhang et al. 2014; Modenese & Renault 2021).

One of the major barriers for the use of the finite element method to estimate bone strain is the necessity for advanced medical imaging to characterise participant-specific bone geometry and material properties. Many researchers do not have access to CT scanning facilities, and if they do scans add significant costs and analysis time to studies. These barriers also limit the utility of finite element analysis in clinical settings (Keyak et al. 1990). In the absence of participant-specific advanced medical imaging data, generic models of the tibia, scaled to each participant using anthropometric data, have been used (Edwards et al. 2009; Edwards et al. 2010; Chen et al. 2016). Alternatively, atlas-based approaches where a tibia model closest to some selection criteria such as bone mineral content (BMC) and/or anthropometrics is selected from a database of models (Xu et al. 2017; Khassetarash et al. 2023). These approaches may be useful for within-participant comparisons but could lead to erroneous conclusions due to the failure to characterise geometry and/or material property differences when comparing between individuals or groups (Khassetarash et al. 2023). Statistical approaches to estimate participants' bone geometry and density distributions, discussed in the next section (Chapter 2.7), may enable generation of more accurate participant-informed models from less intensive imaging modalities or from anatomical landmarks (Väänänen et al. 2015; Nolte et al. 2016). It is unknown whether this approach will produce tibial strain estimates that strongly agree with those from participant-specific models.

## 2.7 Statistical Shape and Appearance Models

Statistical shape models (SSM) describe the average geometry of a bone and the ways in which the geometry varies within a population (Sarkalkan et al. 2014). Statistical appearance models (SAM), sometimes referred to as statistical shape and intensity models, also describe the average and modes of variation of the bone density distribution (Sarkalkan et al. 2014). There are a plethora of applications for this technique including: automating the image segmentation process (Ambellan et al. 2019; Taghizadeh et al. 2019), creating simulated populations for orthopedic implant design (Galloway et al. 2013), identifying phenotypes associated with disease progression or treatment outcomes (Varzi et al. 2015; Wise et al. 2016; Grassi et al. 2021), and predicting bone shape and/or density distributions from sparse data (Zhang et al. 2016; Zhang & Besier 2017; Suwarganda et al. 2019). SSMs of or including the tibia (and fibula) have been reported (Zhang et al. 2016; Audenaert et al. 2019; Nolte et al. 2020; Keast et al. 2023). SAMs have been created for the femur and scapula (Bonaretti et al. 2014; Väänänen et al. 2015; Bah et al. 2015; Grassi et al. 2017; Burton et al. 2019). Prior to this thesis, a SAM of the tibia and fibula had yet to be developed.

As discussed previously (Chapter 2.6), using scaled generic geometries can lead to errors in parameters such as joint center locations, muscle forces, and bone strain. However, manual or semi-automated segmentation of medical imaging data can be time consuming and limit the feasibility of using participant-specific models as clinical tools (Poelert et al. 2013). The ability to reconstruct an individual's bone from partial scans, 2D imaging data (DXA, X-ray), or even motion capture data would enable opportunistic studies and may reduce the time, cost, and ionizing radiation exposure associated with using 3D imaging modalities to generate participant-specific models. SSMs and SAMs have been used in combination with MSK models and the finite element

method to reduce errors associated with scaling generic geometries (Väänänen et al. 2015; Nolte et al. 2016; Zhang et al. 2016; Grassi et al. 2017; Chandran et al. 2019; Suwarganda et al. 2019). While these approaches are not yet widespread, tools to automate and streamline the generation of participant-informed musculoskeletal and finite element models are being developed (Zhang, Sorby, et al. 2014; Modenese & Renault 2021).

### *2.7.1 Generating SSMs and SAMs*

SSMs are created using a set of imaging data that, ideally, represents the variation present in the population of interest. First, points on the surface of the bone of interest are created. This is achieved by identifying landmarks through a combination of manual identification and/or automated algorithms, such that each landmark corresponds to the same anatomical point on each bone of the training set (Sarkalkan et al. 2014). Recently, it has become more common to create surface meshes from the segmented bone(s) of interest and then establish nodal correspondence using non-rigid registration algorithms that allow for local deformations (Väänänen et al. 2015; Burton et al. 2019). In this process, a median geometry is selected from the dataset and used to register the remaining bones in the training data. Selection methods for the median geometry range from subjective to more objective approaches such as choosing the bone with median surface area or volume. Next, the individual and reference mesh are rigidly aligned using the iterative closest point algorithm (Du et al. 2010). Coherent point drift algorithm (Myronenko & Song 2010) performs rigid alignment, scaling, and local deformation to match the reference mesh to the individual's mesh and returns the node in the individual's mesh most likely to correspond to each node in the reference mesh. A generalized Procrustes analysis (Pomidor et al. 2016) may then be used to rigidly align the corresponding meshes across the training set. The data are then compiled into a matrix $x$:

$$x = \begin{bmatrix} X_{1,1} & Y_{1,1} & Z_{1,1} & \dots & X_{1,n} & Y_{1,n} & Z_{1,n} \\ \vdots & \vdots & \vdots & & \vdots & \vdots & \vdots \\ X_{N,1} & Y_{N,1} & Z_{N,1} & \dots & X_{N,n} & Y_{N,n} & Z_{N,n} \end{bmatrix} \quad (2.2)$$

where *X*, *Y* and *Z* are the x-, y- and z-coordinates of each node (*n*) across training instances (*N*) (Sintini 2017). The average shape can then be computed by taking the average of each column of the matrix (Sarkalkan et al. 2014):

$$\bar{x} = \frac{1}{N}\sum_{i=1}^{N} x_i \quad (2.3)$$

Principal components analysis (PCA, discussed below) is then used to calculate the modes of variation of bone shape.

There are two approaches to generate a SAM: image-based and mesh-based. In the image-based approach, anatomical correspondences are established using image registration algorithms and images are warped to match a reference bone to obtain correspondence for image intensity (Schuler et al. 2010; Nicolella & Bredbenner 2012; Bonaretti et al. 2014). This results in a set of volumetric images of the bone(s) of interest where the voxels contain geometry and image intensity information. The image-based approach produces more accurate volume correspondence and better mesh quality, but the perturbed images must be segmented and meshed each time the model is perturbed to use this type of SAM with the finite element method (Bonaretti et al. 2014). An overview of the process used in this thesis to generate a mesh-based SAM is illustrated in Figure 2.3. The bones are first segmented from the image data used to generate and triangular surface meshes. A tetrahedral mesh is generated for the reference bone. Correspondence between surface nodes is established using point cloud registration methods such as the Coherent Point Drift algorithm (Cootes & Taylor 2004; Myronenko & Song 2010). Element correspondence is then

established by elastically morphing the reference mesh to match the individuals' corresponding surface point clouds (Sintini et al. 2018; Burton et al. 2019).

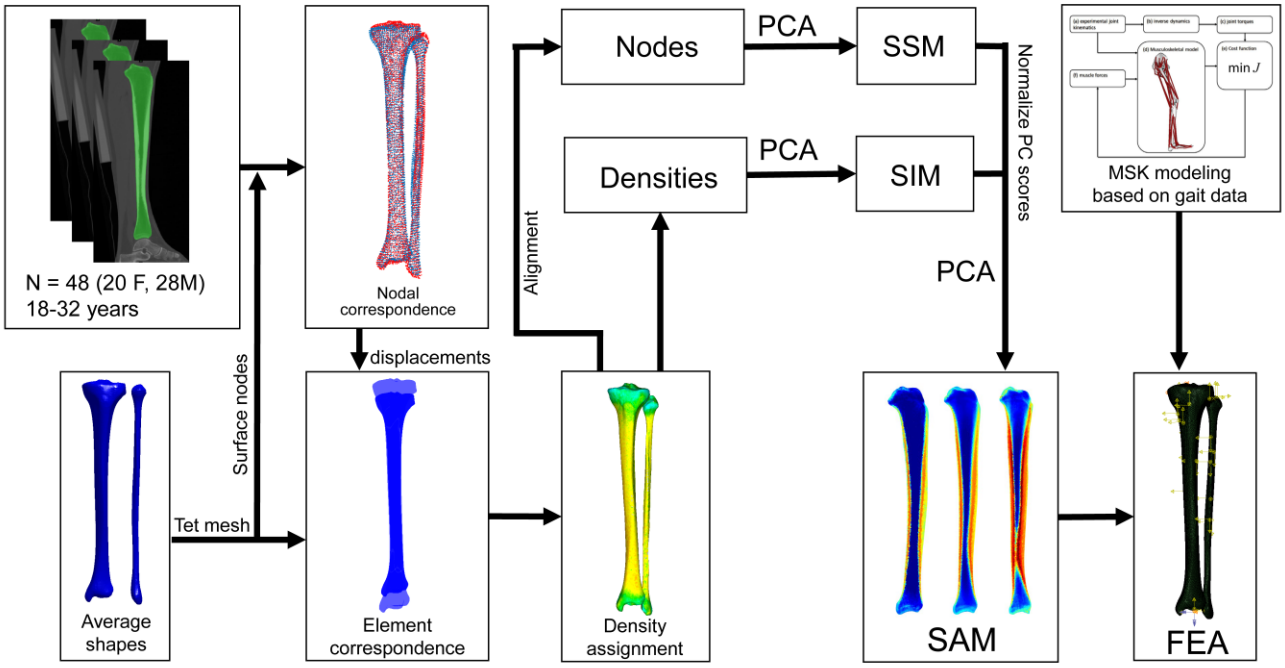


*Figure 2.3 Overview of the mesh-based approach used in this thesis to generate a statistical appearance model (SAM) and the integration of the model with finite element analysis (FEA) to evaluate the influence of geometry and density variations on finite element-predicted bone strain.*

Density values may be assigned to either nodes or elements based on each individual's underlying CT data. Following rigid alignment of the meshes using the Procrustes algorithm, PCA is applied to the data to obtain the SAM. There are two approaches to applying the PCA. In a tiered approach (Figure 2.3, outlined by Cootes & Taylor (2004)), PCA is applied to the node and density data separately to obtain a statistical shape model (SSM) and a statistical intensity model (SIM). The principal component (PC) scores (i.e., variance from the mean along each mode of variation for each individual) calculated from these models are then concatenated into a matrix, normalizing by the total variance in the shape and intensity models. Another PCA is then applied to the normalised

matrix to obtain the combined model. The second approach reported in the literature (Väänänen et al. 2015) combines the node and density information into one matrix, normalizing to account for the difference in scale between node and density variance, and applies a single PCA to the combined data. If the data are normalised in the same way (i.e., by total variance in the shape and density data), these two approaches yield the same results. The mesh-based approach results in more accurate surface correspondences and a more compact SAM (Bonaretti et al. 2014). Perturbing a mesh-based SAM results in meshes that can directly be used as finite element models, but tend to display worse mesh quality when compared to image-based models (Bonaretti et al. 2014).

### *2.7.2 Principal components analysis (PCA)*

PCA is a statistical technique used to reduce the dimensionality of a dataset through feature extraction (Bro & Smilde 2014). The input variables are transformed to create new variables that are linear combinations of the input variables. These new variables, called principal components (PCs), are independent of each other and ordered by the amount of variation they explain in the data. PCs with the lowest amount of variation are removed, reducing the dimensionality of the dataset while retaining the original input variables. A given instance in the dataset can then be predicted using a weighted linear combination of the PCs.

The x-, y-, and z-coordinates and/or density value for each node are the input variables. A covariance matrix is calculated for this data, describing how each variable relates to each of the other variables. The eigenvalues and eigenvectors are then calculated using the equations:

$$det(\lambda I - C) = 0 \tag{2.4}$$

$$C\vec{v} = \lambda\vec{v} \tag{2.5}$$

where $C$ is the covariance matrix, $I$ is the identity matrix, $v$ is the eigenvector, and $\lambda$ is the eigenvalue (Bro & Smilde 2014; Sintini 2017). The eigenvectors are the new variables, or PCs, and the eigenvalues are the variance of each PC. The proportion of variance explained by each PC is calculated by dividing the eigenvalue of a given PC by the sum of the eigenvalues for all PCs (Bro & Smilde 2014). The PCs explaining the most variation are retained. The method used to decide the number of PCs to retain varies in the literature from arbitrary (Bah et al. 2015; Varzi et al. 2015; Wise et al. 2016; Nolte et al. 2016; Zhang et al. 2016; Zhang & Besier 2017) to more analytical (Mei et al. 2008; Suwarganda et al. 2019; Burton et al. 2019) approaches.

### *2.7.3 Interpreting principal components*

Once the average shape and density distribution and the modes of variation have been calculated new instances ($x$) can be created using the equation:

$$x = \bar{x} + \sum_{i=1}^{p} \phi_i b_i \tag{2.6}$$

where $\bar{x}$ is the mean geometry, $p$ is the number of retained PCs, $\phi_i$ is the $i^{\text{th}}$ PC, and $b_i$ is the weighting factor of the $i^{\text{th}}$ PC (Sarkalkan et al. 2014). For a combined geometry ($x$) and density ($d$) model, similar equations are used. The following equations are used for the tiered approach:

$$x = \bar{x} + \sum_{i=1}^{p} (\phi_s W_s^{-1} \phi_{csi}) c_i \tag{2.7}$$

$$d = \bar{d} + \sum_{i=1}^{p} (\phi_d \phi_{cdi})\, c_i \tag{2.8}$$

where $c_i$ is the weighting factor of the $i^{th}$ PC of the combined model, $\phi_s$ is the PCs in the shape model, $\phi_{csi}$ is the shape portion of the $i^{th}$ PC in the combined model, $\phi_d$ is the PCs in the density model, $\phi_{cdi}$ is the density portion of the $i^{th}$ PC in the combined model, and $W_s^{-1}$ is the inverse of

the weighting factor used to normalise the shape data to match the total variance in the density data (Cootes & Taylor 2004).

To obtain an understanding of how each PC influences the model, each weighting factor can be systematically perturbed and added to the average shape and/or density. For example:

$$x = \bar{x} + \sum_{i=1}^{p} 3\sqrt{\lambda_1}\phi_1 \tag{2.9}$$

alters the model by only the first PC, increasing the weight by three standard deviations. Perturbed and average meshes are visualized and compared to interpret the geometry and density variations the PC describes. Heatmaps depicting differences in node position or density value are useful to further aid interpretation.

### *2.7.4 Predicting unseen geometry and density distribution*

Methods to determine the values of the weighting factors ($b_i$ or $c_i$) for an unseen individual vary depending on the data available. Fitting methods for 3D and 2D medical imaging are described elsewhere (Sarkalkan et al. 2014; Grassi et al. 2017). Anatomical landmark data has previously been used to predict pelvis, femur, tibia, and lower limb surface geometry (Zhang et al. 2016; Zhang & Besier 2017; Suwarganda et al. 2019; Nolte et al. 2020; Keast et al. 2023). Landmarks are identified either on the bone surface or using skin-mounted markers for the unseen individual and on the surface of the average mesh. Geometry is then predicted by morphing the SSM along the retained PCs and performing rigid-body transformations to match the morphed model's predicted landmarks to the target landmarks. Pelvis and lower limb bone geometries predicted from anatomical landmarks using this approach have demonstrated reduced distance and volume errors when compared to linearly scaled generic musculoskeletal models (Zhang et al. 2016; Suwarganda et al. 2019). Tibial geometry estimations from bone surface landmarks have

resulted in mean surface geometry errors of approximately 2.6-6.6 mm (Nolte et al. 2020; Keast et al. 2023). It is unclear whether errors of this magnitude have a meaningful influence on parameters such as muscle moment arm and estimates of bone strain.

### *2.7.5 SSM vs SAM*

*Table 2.1 Time per individual to complete pre-processing steps toward generating a SSM and SAM for the tibia and fibula with the methods used in this thesis. Active steps required the investigator to interact with the program to complete the step, while passive steps could be run in the background or overnight.*

| *Processing step* | *Time SAM* | *Time SSM* | *Active/passive* |
|---|---|---|---|
| *Segmenting* | 30 minutes | 30 minutes | Active |
| *Surface node correspondence (CPD)* | 3 hours | 3 hours (or less if using fewer nodes) | Passive |
| *Morphing reference to individual surface* | 5 minutes | | Active |
| *Density assignment* | 10 minutes | | Active |
| *Reading mesh into MATLAB and fixing element assignment* | 3 hours 5 minutes | | Passive |
| *Checking data throughout process* | 10 minutes | 5 minutes | Active |
| *Active time (per individual)* | 55 minutes | 35 minutes | |
| *Passive time (per individual)* | 6 hours 5 minutes | 3 hours | |
| *Total time (per individual)* | 7 hours | 3 hours 35 minutes | |

SSMs are much more common in the medical and bioanthropology literature than SAMs. While SAMs provide more information, they require imaging modalities that enable quantification of both geometry and density (e.g., CT) and involve a more complex and time-consuming processing workflow (Table 2.1). Additionally, open source software is available for the generation of SSMs (Zhang et al. 2014; Cates et al. 2017; Keast et al. 2023), but extensions to SAMs are not yet publicly available. In general, the decision to use a SSM over a SAM depends on the available data and the intended use. If, for example, only MRI is available the analysis will

be limited to a SSM of periosteal (and endosteal) surface geometry. Some SSMs have been developed specifically for applications in MSK modeling (Zhang et al. 2016); in this application only periosteal surface geometry information is necessary. On the other hand, if the intended application included FE analysis as well as MSK modeling a SAM would be needed to provide both bone geometry and density information.

## 2.8 Summary

Stress fractures result from a chronic imbalance between microdamage due to repetitive loading and bone cellular repair processes. Bone strain, specifically strain magnitude and strained volume, is strongly related to the rate of microdamage accumulation and is thought to be the key factor driving the imbalance. To understand how risk factors for stress fracture contribute to injury risk, it is important to characterise their influence on the strain environment of the bone. Epidemiologic evidence indicates that bone geometry and density are risk factors for stress fracture and may contribute to the disparity in risk between sexes. However, the complex three-dimensional variation in geometry and density distribution among young active adults and their influence on the strain environment of the tibia are not well characterised. Additionally, obtaining accurate representations of an individual's bone geometry and density are important for personalized modeling approaches used to estimate bone strain and the probability of fracture but currently requires CT data. Access to CT scanners, financial cost, and the time required to characterise bone geometry and density from the images limit the use of these approaches. Emerging statistical approaches may address some of these barriers.

The research presented in this thesis utilizes a combination of statistical shape and appearance modeling, biomechanical data, and the finite element method to characterise tibial-fibular geometry and density variations, errors due to anthropometric data-based prediction

approaches, and their mechanical implications in young active adults. The findings from these studies offer insights into bone geometry and density distributions as risk factors for stress fracture. In addition to identifying key features influencing bone strain, potential methods to characterise bone geometry and density distributions in the absence of medical imaging are evaluated.

# Chapter 3

# Tibial-fibular geometry and density variations associated with elevated bone strain and sex disparities in young active adults

## 3.1 Introduction

Stress fracture is a common injury in runners and military recruits (Cosman et al. 2013; Rizzone et al. 2017; Kardouni et al. 2021). Stress fractures frequently occur at the tibia and females are at greater risk of fracture than males (Cosman et al. 2013; Rizzone et al. 2017; Kardouni et al. 2021). Mechanical fatigue, a phenomenon whereby submaximal repetitive loading leads to the accumulation of microdamage, has been associated with the development of stress fractures (Burr et al. 1990). It is important to note that the rate of damage accumulation is strongly related to bone strain magnitude (Carter et al. 1981a; Pattin et al. 1996).

Bone geometry and density are two factors that influence bone strain magnitude. It has been hypothesized that differences in transverse cross-sectional size, cortical thickness, and condyle size between males and females contribute to the greater risk of stress fracture in females when compared to males (Nieves et al. 2005; Brzobohatá et al. 2016; Audenaert et al. 2019). In current literature, characterization of geometry, density, and estimates of bone strength within and between sex and injury status groups has largely relied on simple measures such as cortical area,

cortical thickness, section modulus, polar strength-strain index, and bone mineral content measured at transverse cross-sections (Nieves et al. 2005; Cosman et al. 2013; Popp et al. 2020). Bone strain is a complex function of bone geometry and density distribution, and can be directly estimated using subject-specific finite element models (Xu et al. 2020). However, as a numerical technique, it can be difficult to isolate the contributions of different model parameters and understand their relative impact on bone strain using finite element models alone.

This limitation could be overcome using statistical shape models (SSMs), which characterise geometry variation, and statistical appearance models (SAMs), which characterise bone geometry and density variations within a population. SSMs have been used to describe geometry variations in a variety of bones (Zhang, Malcolm, et al. 2014; Sintini et al. 2018; Burton et al. 2019; Grant et al. 2020; Bruce, Baggaley, Welte, et al. 2022), characterise sexual dimorphism (Brzobohatá et al. 2016; Audenaert et al. 2019; Bruce, Baggaley, Welte, et al. 2022), and to explore the influence of geometry variations on spine and knee kinematics and joint contact mechanics (Campbell & Petrella 2016; Clouthier et al. 2019; Clouthier et al. 2022). SAMs have been developed for bones including the scapula, lumbar vertebrae, femur, and tibia (Bryan et al. 2012; Nicolella & Bredbenner 2012; Galloway et al. 2013; Bah et al. 2015; Day et al. 2022). Importantly, SAMs in combination with finite element analysis have enabled population-level investigations of knee and hip implant performance (Bryan et al. 2012; Galloway et al. 2013), proximal femur strength in a sideways fall (Nicolella & Bredbenner 2012), and vertebral stiffness (Day et al. 2022). The influence of tibia and fibula geometry and density variations on bone strain has yet to be investigated.

The purpose of this study was to characterise tibial-fibular geometry and density variations using a SAM and to quantify the influence of these variations on finite element-predicted bone

strain in young active adults. We expected that transverse cross-sectional dimensions and cortical thickness would demonstrate the largest influence on bone strain after controlling for scale and that sex-related geometry and density variations would result in higher bone strain in the average female when compared to the average male.

## 3.2 Material and Methods

### *3.2.1 Statistical Appearance Model*

A SAM was constructed using computed tomography (CT) scans of the left tibia and fibula (GE Revolution GSI, General Electric Medical System, Milwaukee, WI; acquisition settings: 120 kVp, 200 mA, in-plane resolution of 0.48 x 0.48 mm, slice thickness of 0.625 mm) obtained from forty-eight healthy adults (20 females and 28 males, age = 18-32 years, height = 1.49-1.87 m, mass = 48.3-86.0 kg). Age, height, and mass for males and females are presented in Table 3.1. Participants were recreationally active at least three times per week and had no musculoskeletal injuries that limited physical activity within the three months prior to scanning. All participants provided written, informed consent. Study protocol was approved by the university's Conjoint Health Research Ethics Board.

*Table 3.1 Mean (standard deviation) participant age, height, and body mass of females and males included in the SAM.*

| Sex | n | Age (years) | Height (m) | Mass (kg) |
|---|---|---|---|---|
| **F** | 20 | 19.9 (1.3) | 1.65 (0.08) | 60.1 (5.8) |
| **M** | 28 | 22.4 (4.4) | 1.76 (0.07) | 71.5 (7.2) |
| **p-value** | | 0.006 | <0.001 | <0.001 |

The tibia and fibula were semi-automatically segmented in the Mimics Innovation Suite (v21, Materialise, Leuven, Belgium) and triangular periosteal surface meshes were generated. Reference four-node tetrahedral volume meshes were created from average tibia and fibula

geometries, obtained from a previously described SSM based on a subset of the data used in the present study (Bruce, Baggaley, Welte, et al. 2022). The reference tibia and fibula meshes contained 270 002 and 41 077 elements, respectively. Surface node correspondence between the reference meshes and participant geometries were established using the Coherent Point Drift algorithm (Myronenko & Song 2010). Displacements between corresponding surface nodes were calculated and used as boundary conditions to morph the reference mesh to match each participant's surface geometry in Abaqus (v.2019, Dassault Systèmes Simulia Corp.; Providence, USA). The resulting meshes were then overlaid onto the participant's CT data. A hydroxyapatite calibration phantom (QRM GmbH; Moehrendorf, Germany) was used to identify a linear relationship between Hounsfield units in the CT image and equivalent bone mineral density ($\rho_{HU}$) for each participant. Each element was assigned a density value based on a volume-weighted average of the underlying voxels.

The resulting meshes were aligned to the reference mesh using the Procrustes algorithm, preserving scale. Principal components analysis (PCA) was applied to construct the SAM as outlined by Cootes and Taylor (Cootes & Taylor 2004): PCA was applied to the nodes to obtain a SSM and to the density values to obtain a SIM. To account for correlations between shape and density, a further PCA was applied to a combined matrix containing shape and intensity parameters, weighted to normalise the total variance in each set, to obtain a SAM.

### *3.2.2 SAM Perturbations*

The first five principal components (PCs), cumulatively accounting for 70.5% of the total variance in the model, were evaluated. The SAM was perturbed along each PC by ± 1 and 2 standard deviations from the mean. Average PC scores for males and females were calculated. The first PC described isotropic scaling and related geometry and density variations and was strongly

correlated with height ($r^2$=0.83). Meshes representing the average male and average female geometry and density distribution, controlled for scaling and related variations, were created by perturbing all PCs except the first by their respective average scores. Meshes isolating geometry and density variation for the average male and female were generated for a secondary analysis.

### *3.2.3 Finite Element Models*

Following perturbations, mesh elements were converted to ten-node tetrahedral elements. Element densities were discretized into bins, where the width of each bin was 0.01 g/cm$^3$ $\rho_{HU}$. Bin centers were used as the density value for each element. Orthotropic linear-elastic material properties were assigned to each element. The elastic modulus of bone in the axial direction was calculated as a function of element apparent bone mineral density ($\rho_{app} = \rho_{HU}/0.626$) (Dalstra et al. 1993):

$$E_3 = 6570 \cdot {\rho_{app}}^{1.37} \tag{3.1}$$

The other constants were obtained assuming constant anisotropy: $E_1 = 0.574 \cdot E_3$, $E_2 = 0.577 \cdot E_3$, $G_{12} = 0.195 \cdot E_3$, $G_{23} = 0.265 \cdot E_3$, $G_{31} = 0.216 \cdot E_3$, $\nu_{12} = 0.427$, $\nu_{23} = 0.234$, $\nu_{31} = 0.405$, where subscripts 1-3 denote the medial-lateral, anterior-posterior, and axial directions, respectively (Rho 1996). This definition of material properties has demonstrated excellent agreement between cadaveric experimental measurements and finite element predictions of bone strain and fracture strength at the tibia (Gray et al. 2008; Edwards et al. 2013).

A preliminary mesh convergence analysis (Appendix A, Figure A.6) was performed using the participant model with the largest volume. Increasing the number of elements by ~100% (tibia and fibula combined) from 132 740 and 20 241 elements to 270 002 and 41 077 elements changed 95$^{th}$ percentile pressure-modified von Mises strain by less than 4% and strained volume by less

than 2%, suggesting the mesh was adequately converged. We conservatively selected the finer mesh, as the added computational time was negligible.

### *3.2.4 Finite Element Boundary Constraints*

Boundary constraints were similar to previous work from our group, with pinned constraints at the knee and ankle and complex proximal tibia-fibula joint constraints (Haider et al. 2020). One point at the middle of the tibial plateau was fully constrained. Surface nodes on the tibial plateau within one centimeter of the fixed point in the axial direction were kinematically coupled to rotate about the fixed point. One point on the medial condyle was fixed in the anterior-posterior direction. The ankle center of rotation was estimated as the midpoint between the malleoli and used for the application of the joint contact force. This point was constrained in the anterior-posterior and medial-lateral directions. The ankle center of rotation was coupled to surface nodes near the tibia-talus and fibula-talus interfaces, such that the coupled nodes remained free to rotate about the ankle center of rotation. The distal tibia-fibula joint was modeled with surface-based tied constraints. At the proximal tibia-fibula joint, spring elements with stiffness of 133 N/mm and 109 N/mm were used to model the anterior and posterior ligaments, respectively (Marchetti et al. 2017). Nodes at the articulating surface of the proximal tibia-fibula joint were tied to prevent motion in the direction normal to the joint surface.

### *3.2.5 Finite Element Loads*

Lower limb joint contact force and muscle forces were calculated based on motion capture and force data from one female participant (age = 24 years, mass = 59 kg, height = 170 cm). The participant ran at 3.3 m/s on an instrumented treadmill (Bertec, Columbus, OH) while motion and force data were collected at 200 Hz and 1000 Hz, respectively, using an eight-camera Vicon Nexus system (v. 1.8.4, Vicon Motion Systems Ltd, Oxford, UK). An inverse dynamics-based static

optimization routine, detailed in our previous work, was used to calculate lower extremity muscle and joint contact forces (Haider et al. 2020). Briefly, a musculoskeletal model of the pelvis and lower limb containing forty-five muscles (Arnold et al. 2010) was scaled to the participant's segment lengths and body mass. Muscle forces were computed such that the sum of muscle moments at each joint was equal to the net joint moment computed from inverse dynamics. The following moments were used as constraints in the optimization: flexion-extension and abduction-adduction moments at the hip, flexion-extension moment at the knee, flexion-extension moment at the ankle, and the pronation-supination sub-talar moment. The optimization minimized the sum of muscle stresses squared. Ankle joint contact force and muscle forces at the time of peak resultant ankle joint contact force were scaled to the SAM average finite element model by mass (i.e., $F_{FE} = F_{participant}*(m_{average}/m_{participant})$). The same joint contact and muscle forces were applied to all models. Ankle joint contact force was applied at the ankle center of rotation. Insertion points of seventeen muscles attaching to the tibia or fibula (Appendix A, Table A.1) and the patellar ligament were identified by aligning the MSK model geometry and the SAM average finite element mesh using an iterative closest points algorithm and mapping each muscle point to the nearest surface node. A concentrated force was applied at each attachment point (Appendix A, Table A.1). A residual moment term about the sagittal and axial axes that accounts for other sources of torque (e.g., bi-articulating muscles such as the medial and lateral gastrocnemius) about the ankle was calculated for each perturbed geometry and applied at the ankle center of rotation (Haider et al. 2020).

### *3.2.6 Outcome Measures and Comparisons*

Finite element models were solved in Abaqus (v.2019, Dassault Systèmes Simulia Corp.; Providence, USA). Custom Matlab (r2019a, Mathworks, Natick, MA) scripts were used to

calculate pressure-modified von Mises equivalent strain, which is a modification of the von Mises strain criterion that has previously been shown to predict failure in quasi-brittle materials that demonstrate compression-tension strength asymmetry (de Vree et al. 1995; Haider et al. 2021). Analysis was limited to elements containing bone (element density values $\geq 0.5$ g/cm$^3$) in the tibial diaphysis, defined as 20-80% of the length of the tibia (Edwards et al. 2015). The bone density threshold sensitivity was tested in the average model, and the average male and female models. Peak strain changed by less than 2.4% when thresholds of 0.5 and 1.0 g/cm$^3$ were used. Strained volume changed by less than 0.7% and did not affect male vs. female comparisons. We conservatively selected the lower threshold. Elements within a 1.0 cm radius of the soleus force application and a 0.5 cm radius of other muscle force application points, including transcortical elements, were removed from the analysis due to artefactually high strains (over 10 000 με). The large force applied at the attachment point for the soleus necessitated a larger radius to remove all elements with artefactually high strains. Over 98% of the elements containing bone in the tibial diaphysis remained for analysis after artefacts were removed. The 95$^{th}$ percentile (peak) strain and strained volume, defined as the sum of the volume of elements experiencing strain greater than or equal to 4000 με, were quantified for each model. We previously demonstrated that strained volume, with a threshold of 4000 με, was a strong predictor of fatigue life for whole rabbit tibiae in uniaxial and biaxial (compression and torsion) modes of loading (Haider et al. 2021). At the material level, O'Brien et al. (O'Brien et al. 2005) observed rapid microdamage accumulation and subsequent fracture in cyclically-loaded cortical bone at a stress range of 80 MPa, which would correspond to 4000 με for an assumed elastic modulus of 20 GPa; samples loaded at lower stress ranges accumulated damage but did not fracture (O'Brien et al. 2005). Absolute and percentage

differences in peak strain and strained volume between perturbed models and the average model were calculated. These measures were also compared between average male and female models.

### *3.2.7 Statistical Analysis*

In addition to qualitative assessments of differences between average male and female geometry and density generated from the SAM, t-tests were performed to compare PC scores between females and males. According to Shapiro-Wilk and Levene's tests, PC scores for male and female groups were normally distributed and had equal variances. A Sidak correction for multiple comparisons was applied such that the family-wise error rate was 0.05. Pearson product-moment correlations between scores of the first five PCs and age were also evaluated. Statistical tests were performed in SPSS (v27.0, IBM Corp., Armonk, NY).

## 3.3 Results

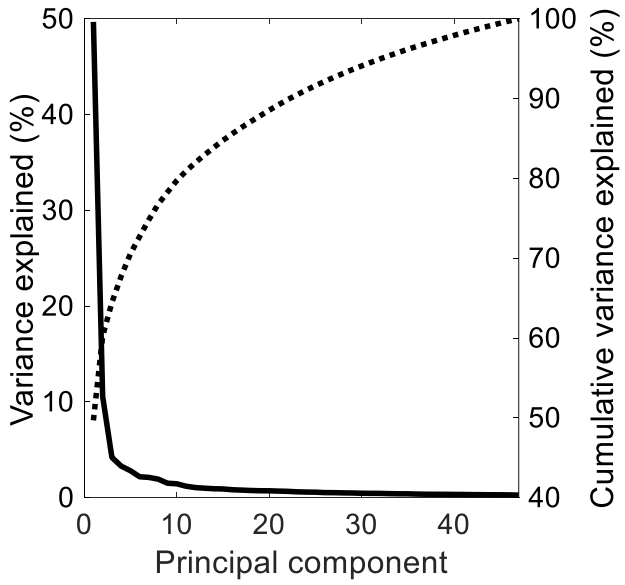


*Figure 3.1 Percent variation captured by principal components of the SAM*

The first PC, dominated by isotropic scaling, explained half (49.7%) of the total variance in the SAM. The first five PCs accounted for 70.5% of the total cumulative variance. The variance

explained by the PCs are displayed in Figure 3.1. Geometry and density variations described by the first five PCs were independent of age ($p \geq 0.310$).

### *3.3.1 PC Perturbations*

The first five PCs described tibial geometry and density variations including: isotropic scaling, axial length, cross-sectional size and geometry, curvature, and regional variations in cortical thickness and density (Table 3.2). The fibula varied to a lesser degree, typically displaying corresponding variations in dimensions and cortical density. Visualizations of geometry and density variations for each PC are provided in supplementary Figures A.1-A.5 (Appendix A). Perturbations of ± 1 standard deviation along these PCs resulted in 2.0-5.7% differences in peak strain and 11.5-44.6% differences in strained volume when compared to the average model (Table 3.2). Perturbations of ± 2 standard deviations along these PCs resulted in 3.9-12.0% differences in peak strain and 20.8-95.4% differences in strained volume when compared to the average model (Table 3.2).

Perturbing PC 1, 2, and 5 resulted in the largest changes in peak strain and strained volume. The first PC was dominated by isotropic scaling. Lower density at the endocortical surface corresponded with increased size. Increasing size by one standard deviation reduced peak strain and strained volume by 5.3% and 38.7%, respectively. The second PC explained 10.6% of the total variance and described variations in tibia and fibula length, tibial curvature, and cortical thickness (Figure 3.2). A longer, straighter tibia with increased cortical thickness reduced peak strain and strained volume (perturbing by plus one standard deviation = 5.3% and 36.5% reduction in peak strain and strained volume, respectively) when compared to the average model (Figure 3.3). The fifth PC explained 2.8% of total variance, describing changes in diaphysis cross-sectional size and geometry, and variation in density distribution. Increased cross-sectional size, corresponding with

decreased cortical density in the anterior diaphysis and regional variations in cortical thickness, resulted in 4.0% lower peak strain and 29.1% smaller strained volume when compared to the average model.

*Table 3.2 Geometry and density variations described by the first five principal components and their influence on 95$^{th}$ percentile pressure modified von Mises strain (peak ε) and strained volume ($\varepsilon_{vol}$) compared to the average model. Data are presented as absolute difference (percent difference).*

| PC | | Perturbation (σ) | | | | Geometry and density variation in positive direction |
|---|---|---|---|---|---|---|
| | | -2 | -1 | 1 | 2 | |
| **1** | Peak ε (με) | 446 (12.0) | 205 (5.5) | -197 (-5.3) | -380 (-10.2) | Increased size<br>Decreased density at the endocortical surface |
| | $\varepsilon_{vol}$ ($mm^3$) | 1395 (59.1) | 793 (33.6) | -914 (-38.7) | -1726 (-73.2) | |
| **2** | Peak ε (με) | 428 (11.5) | 212 (5.7) | -195 (-5.3) | -375 (-10.1) | Longer tibia and fibula<br>Less curvature in sagittal plane<br>Increased density at the endocortical surface |
| | $\varepsilon_{vol}$ ($mm^3$) | 2250 (95.4) | 1052 (44.6) | -861 (-36.5) | -1491 (-63.2) | |
| **3** | Peak ε (με) | -160 (-4.3) | -81 (-2.2) | 75 (2.0) | 146 (3.9) | Decreased cross-sectional size in proximal 2/3 of tibia<br>Smaller proximal tibial condyles<br>More triangular cross-section at mid-diaphysis<br>Increased density in middle 1/3 and decreased density in proximal and distal 1/3 near the endocortical surface |
| | $\varepsilon_{vol}$ ($mm^3$) | -616 (-26.1) | -294 (-12.5) | 272 (11.5) | 491 (20.8) | |
| **4** | Peak ε (με) | 207 (5.6) | 103 (2.8) | -100 (-2.7) | -198 (-5.3) | Larger tibia and fibula cross-sectional size<br>Increased density in distal half, decreased density in proximal half at the endocortical surface |
| | $\varepsilon_{vol}$ ($mm^3$) | 916 (38.9) | 456 (19.3) | -471 (-20.0) | -928 (-39.3) | |
| **5** | Peak ε (με) | 330 (8.9) | 159 (4.3) | -150 (-4.0) | -291 (-7.8) | Larger tibia and fibula cross-sectional size, especially along the A/P axis<br>Regional variations in cortical thickness<br>Decreased cortical density in anterior diaphysis |
| | $\varepsilon_{vol}$ ($mm^3$) | 1568 (66.5) | 751 (31.9) | -686 (-29.1) | -1308 (-55.5) | |

### *3.3.2 Sexual Dimorphism*

The female tibia was narrower along both anterior-posterior and medial-lateral axes and had smaller condyles. Cortical density was greater and cortical thickness in the distal ¼ of the diaphysis was smaller in the average female when compared to the average male (Figure 3.4). Scores for the third PC were different between males and females ($p < 0.001$), where females had more positive scores. PC three illustrated similar geometry and density variations (Table 3.2, Supplemental Figure A.3) to the observed variations between sexes. These differences resulted in 5.5% (198 με) higher peak strain and 41.3% (830 $mm^3$) higher strained volume in the average female when compared to the average male. When isolated, geometry differences resulted in 9.7% (345 με) higher peak strain and 99.5% (1678 $mm^3$) larger strained volume in the average female. In contrast, density differences alone resulted in 3.9% (146 με) lower peak strain and 30.6% (832 $mm^3$) smaller strained volume in the average female when compared to the average male.

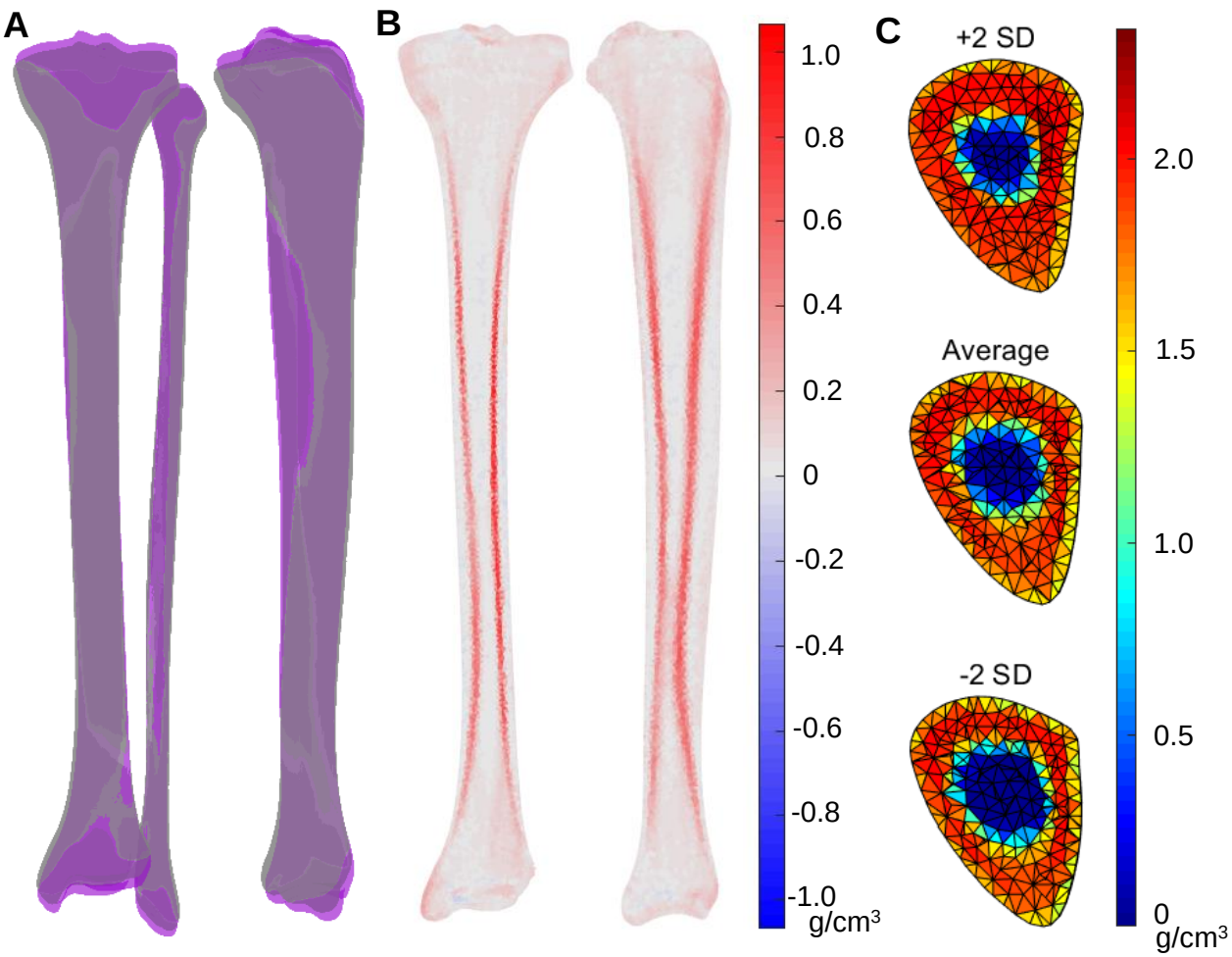


*Figure 3.2 Geometry and density variations characterised by the second principal component. (A) Surface geometry of the tibia and fibula perturbed by +2 standard deviations (SD) (purple) and the average geometries (grey). (B) Frontal (left) and sagittal (right) cross-sections of the tibia illustrating differences in internal density distribution between +2 SD and average, where red indicates greater density in the model perturbed by +2 SD. (C) Axial cross-sections of the tibial diaphysis at 50% of total axial length.*

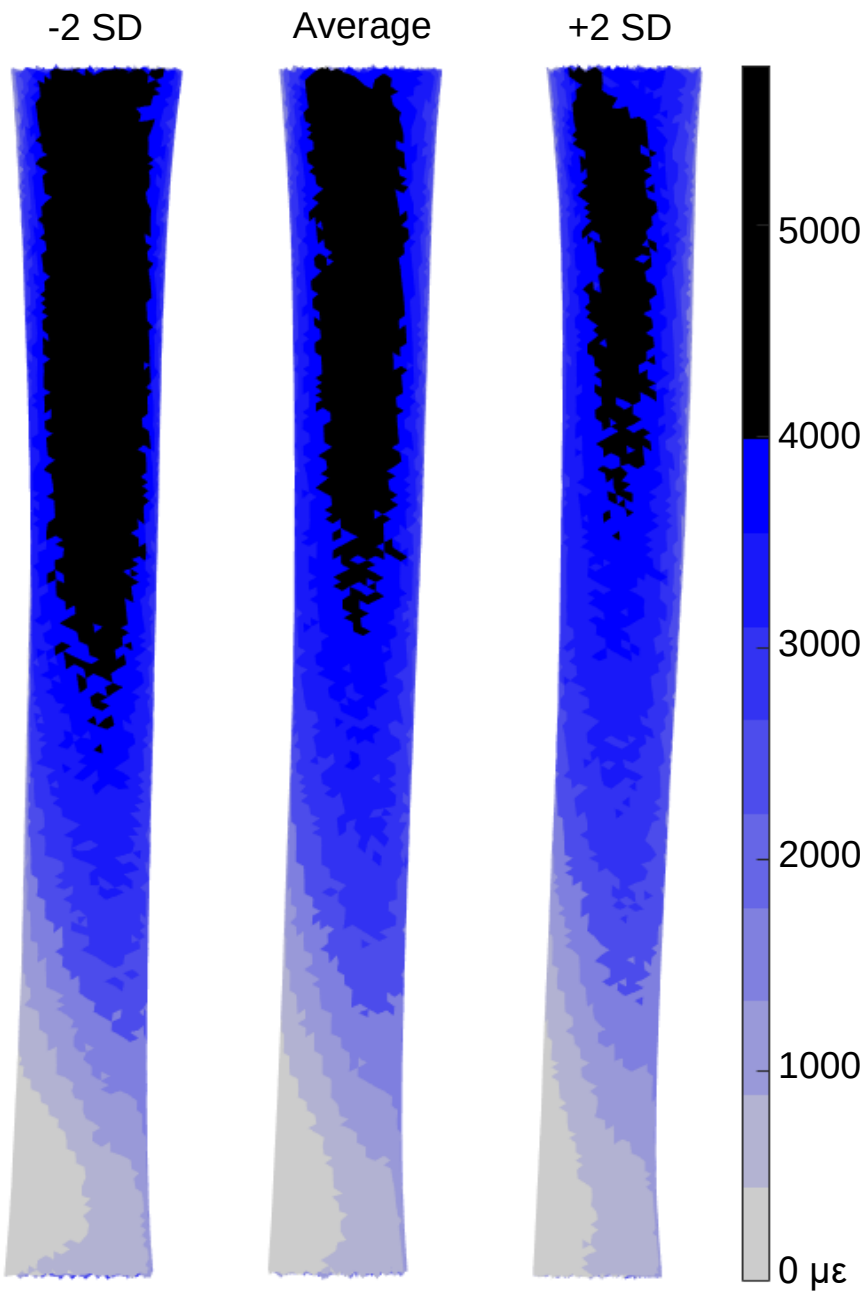


*Figure 3.3 Pressure-modified von Mises strain distribution across the posterior surface of the tibial diaphysis for perturbations of ± 2 standard deviations (SD) along the second principal component compared to the average. Elements coloured black (≥ 4000 με) contributed to the strained volume measure.*

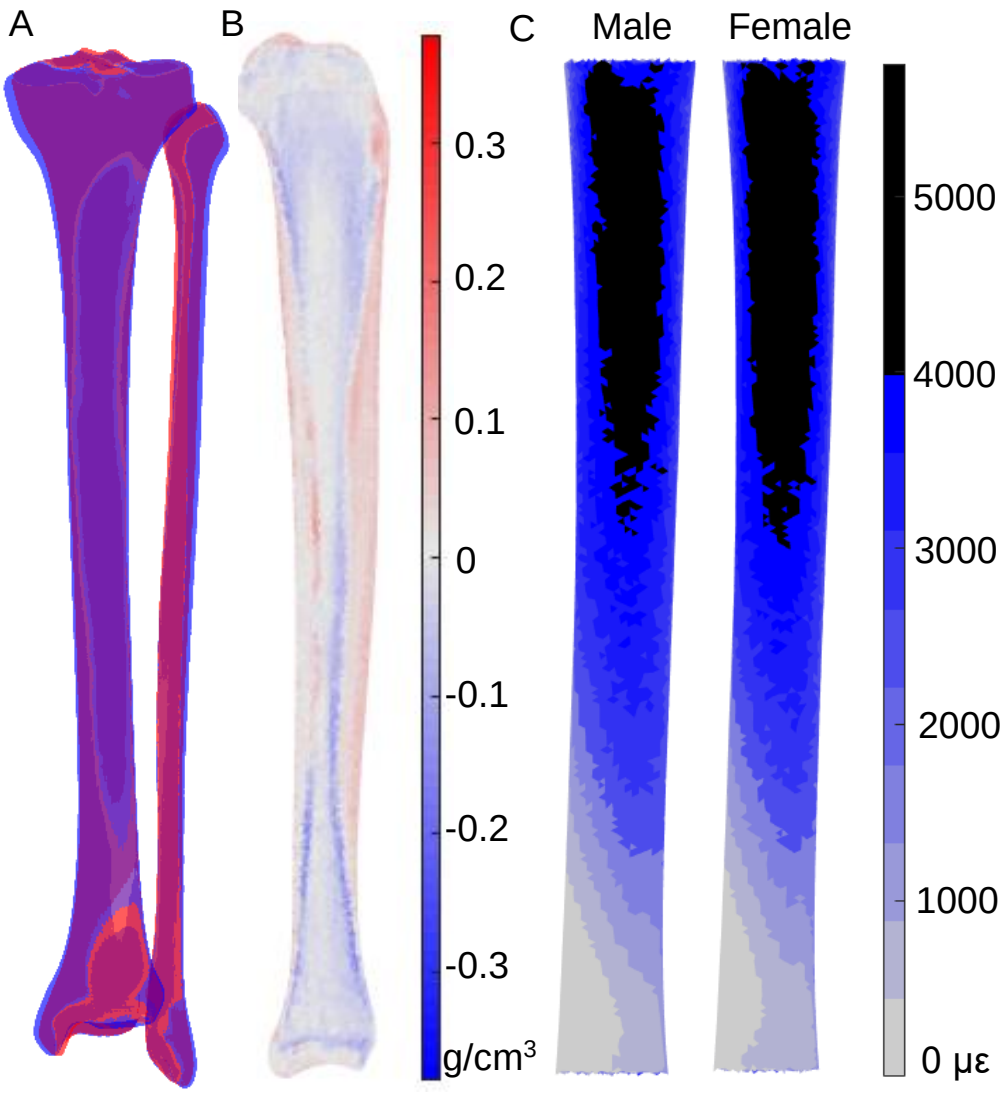


*Figure 3.4 Comparisons between the average female and male tibia and fibula, controlled for scaling. (A) Average female (red) and male (blue) periosteal geometry. (B) Sagittal cross-section of the tibia displaying differences in density between the average female and average male, controlled for bone size. Red indicates higher density in the female model. (C) pressure-modified von Mises strain distribution across the posterior surface of the tibial diaphysis. Elements coloured black (≥ 4000 με) contributed to the strained volume measure.*

## 3.4 Discussion

The aims of this study were to characterise tibial-fibular geometry and density variations and to quantify the influence of these variations on finite element-predicted bone strain in young

active adults. Finite element-predicted bone strain was sensitive to geometry and density variations present in a young active adult population. Isotropic scaling, tibial curvature, cortical thickness, and diaphyseal dimensions in the transverse plane had the largest effects on bone strain. Sex differences in geometry were subtle yet resulted in greater bone strain in the average female than the average male when controlled for scale.

The average female model illustrated 5.5% greater $95^{th}$ percentile pressure-modified von Mises strain and 41.3% greater strained volume than the average male model when controlled for scaling and related variations. At the material level, strain magnitude is associated with fatigue life and the accumulation of microdamage, where higher strain results in greater damage accumulation and a shorter fatigue life (Carter et al. 1981a; Pattin et al. 1996). Strained volume examines the entire strain distribution and captures the amount of bone experiencing strain above a specific threshold; in theory, a larger volume experiencing high strain has a greater probability of loading a site of localized microstructural weakness, which accelerates fatigue failure (Taylor 1998). Indeed, uniaxial and biaxial mechanical tests of whole rabbit tibiae revealed strong relationships ($r^2$ = 0.73 and 0.59, respectively) between pressure-modified von Mises-based strained volume and fatigue life, where greater strained volume was associated with fewer loading cycles to fracture (Haider et al. 2021). Furthermore, our finite element results are in line with clinical data. The largest area of strained volume and the highest strains, in all models, occurred on the posterior surface of the tibial diaphysis, consistent with Kijowski et al.'s (Kijowski et al. 2012) observations of the most frequent tibial stress fracture location. Thus, the fact that the average female illustrated greater peak strain and strained volume suggests that sexual dimorphism in the tibia and fibula, independent of applied load and scale, may indeed contribute to the greater risk of stress fracture

observed in females when compared to males in a young physically active population (Cosman et al. 2013; Rizzone et al. 2017; Kardouni et al. 2021).

The larger strains and strained volume observed in the average female when compared to the average male were explained by geometric rather than density variations. The average female tibia was smaller in the transverse plane when compared to the average male tibia; cortical area and second moment of area (i.e., resistance to bending) were also smaller through the diaphysis, leading to higher strain. In contrast, cortical density in the diaphysis was slightly greater (up to approximately 0.05 $g/cm^3$ greater) in the average female when compared to the average male, leading to lower strain. Specifically, when isolated, density variations resulted in 3.9% smaller peak strain and 30.6% smaller strained volume. However, the small increase in cortical density was not sufficient to offset the effects of reduced transverse cross-sectional size.

As expected, finite element-predicted strain was sensitive to scaling, geometry, and density variations among young active adults. Isotropic scaling, tibia and fibula axial length, tibial curvature, cortical thickness, and transverse cross-sectional size were the most prominent variations characterised by the SAM and resulted in substantial differences in bone strain when perturbed by ± 2 standard deviations. Increases in isotropic scaling, cortical thickness, and transverse cross-sectional dimensions are associated with increased cortical area, second moment of area, and polar moment of area, which result in reduced stresses and strains in response to axial, bending, and torsional loads. An increase in axial length would increase the moment arm of forces applied at the joints relative to the middle of the diaphysis and would result in a greater bending moment and higher strain. However, the expected effect of length on strain was not observed when evaluating the influence of the second PC due to the greater and opposing influence of concomitant

increases in cortical thickness and reduced sagittal plane curvature. In long bones, less curvature decreases bending resulting from axial loads, leading to smaller peak stresses and strains (Bertram & Biewener 1988).

Our findings highlight the importance of obtaining subject-specific geometry and density for finite element simulations when comparing bone strain between individuals or groups, supporting previous work comparing generic and subject-specific modelling approaches (Xu et al. 2020). When clinical computed tomography scans of the tibia and fibula are not available, SAMs may serve as a tool to estimate subject-specific geometry and density from more accessible imaging methods and/or anatomical measures. For example, Väänänen et al. (Väänänen et al. 2015) reconstructed 3-dimensional proximal femur geometry and density from 2-dimensional clinical dual-energy x-ray absorptiometry (DXA) images using a SAM. The mean point to surface and volumetric bone mineral density errors were 1.41 mm and 0.19 g/cm$^3$, respectively, and this resulted in a strong correlation ($r^2$ = 0.85) between finite element predictions from DXA- and computed tomography-based models. Perhaps a similar approach could be developed to generate subject-specific finite element models of the tibia and fibula based on DXA, peripheral computed tomography, and/or skin-based markers. We found that tibia sagittal-plane curvature, diaphysis cortical thickness, and diaphysis transverse cross-sectional dimensions had the greatest influence on tibial bone strain. As such, obtaining measures of these factors from less intensive imaging methods may be most important for SAM-based reconstruction to minimize bone strain inaccuracies due to geometry or density prediction errors.

A limitation of our analysis was that we only modeled a single loading configuration. We chose to apply the same joint contact and muscle forces to all models to isolate the effects of

geometry and density perturbations. However, contact force magnitude and direction, and the distribution of muscle forces may vary between individuals, sexes, running conditions, and other movements. For example, Meardon et al. (2021) observed smaller axial force, larger medial-lateral force, and smaller anterior-posterior bending moment at the tibia in females when compared to males during running. These factors would interact with bone geometry to determine the strain environment of the tibia and fibula. To examine the sensitivity of our results for sexual dimorphism to the applied loads, we performed a post-hoc sensitivity analysis where loads calculated based on data from a male (age = 36, height = 1.73 m, mass = 76.8 kg, running speed = 3.3 m/s; see Appendix A, Table A.2 for muscle and ankle contact forces) were applied to the average male and female models. Our interpretations did not change; peak strain and strained volume were greater (by 161 με and 419 $mm^3$) in the average female when compared to the average male, controlled for scale and applied load. Still, future work evaluating the interaction between sex differences in loads and bone morphology is warranted. A second limitation of our analysis was that the training set used to build the SAM in our study was composed of only young physically active adults. The inclusion criteria for our training set limits the applicability of our SAM to other populations (e.g., clinical, pediatric, or geriatric); however, young active adults are perhaps the most studied population in biomechanics and running research.

## 3.5 Conclusions

PCs characterising tibial curvature, cortical thickness, and cross-sectional dimensions had the greatest influence on bone strain. On average, females illustrated narrower tibiae when controlled for scale, resulting in larger strains when compared to the average male. Our findings identify key morphological parameters associated with elevated bone strain that may have implications for stress fracture risk.

# Chapter 4

# Sex disparities in tibia-fibula geometry and density are associated with elevated bone strain in females: A cross-validation study

## 4.1 Introduction

Tibial stress fracture is a common overuse injury among runners and military personnel (Cosman et al. 2013; Rizzone et al. 2017; Kardouni et al. 2021). Stress fractures have been associated with a mechanical fatigue phenomenon, in which submaximal repetitive loading leads to the accumulation of microdamage (Burr et al. 1990). Over time, with insufficient repair, this accumulation of microdamage may lead to a stress fracture (Burr et al. 1990). The rate of microdamage accumulation is strongly related to bone strain magnitude (Carter et al. 1981a; Pattin et al. 1996). Bone also exhibits a statistical size effect, wherein a larger volume of bone experiencing high strain tends to illustrate a shorter fatigue life because of the increased probability of loading weak regions or microstructural flaws (Taylor 1998; Bigley et al. 2007). Indeed, the volume of bone experiencing high strain, or strained volume, was more strongly related to the fatigue life of whole bone than peak strain magnitude (Haider et al. 2021).

Females are up to four times more likely to sustain a stress fracture than males (Kardouni et al. 2021). It has been hypothesized that sex-related differences in tibial diaphysis cross-sectional geometry (e.g., periosteal circumference and cortical thickness) may contribute to the elevated risk

of stress fractures observed in females (Nieves et al. 2005; Tommasini et al. 2007). We recently used a statistical appearance model (SAM), describing variations in tibia-fibula geometry and density in a young physically active population, in combination with the finite element method to evaluate sexual dimorphism and its influence on bone strain (Bruce, Baggaley, Khassetarash, et al. 2022). When controlled for isotropic scaling, the average female illustrated a narrower tibial diaphysis, resulting in 6% greater peak strain and 41% greater strained volume when compared to the average male. While these results were encouraging, the analysis was performed using a moderate sample size of twenty females and twenty-eight males, and the geometric differences between the average female and male were subtle.

The purpose of this study was to cross-validate our previous findings of sex-related differences in tibia-fibula bone geometry, density, and finite element-predicted bone strain in an entirely new cohort of young physically active adults. Previous studies examining tibial sexual dimorphism using transverse cross-sections observed smaller bone size relative to body size in females when compared to males (Nieves et al. 2005; Tommasini et al. 2007; Evans et al. 2008). Based on these observations and our previous results for the whole tibia-fibula complex, we hypothesized that the average female would illustrate a narrower tibial diaphysis and elevated strained volume when compared to the average male.

## 4.2 Materials and Methods

Fifteen females (22.9 ± 3.0 years, 1.67 ± 0.07 m, 60.9 ± 6.7 kg) and fifteen males (23.3 ± 4.3 years, 1.77 ± 0.09 m, 75.6 ± 10.0 kg) were recruited from the student population at the University of Calgary. Participants were active at least three times per week, had sustained no injuries in the 3 months prior to scanning, had no contraindications for CT, and had no metal hardware in their legs. The study was approved by the University's Conjoint Health Research

Ethics board (REB21-1971). Participants provided written, informed consent prior to participating in the study.

### *4.2.1 Sex-related differences in bone shape and density*

A CT scan of each participant's left lower leg and foot were obtained using a Revolution GSI scanner (General Electric Medical System, Milwaukee, WI; acquisition settings: 120 kVp, 200 mA, in-plane resolution of 0.48 x 0.48 mm, slice thickness of 0.625 mm). One participant had previous surgery on their left knee; in this case a scan of the right leg was obtained and the data were mirrored.

A SAM of the left tibia and fibula, described in a previous publication (Bruce, Baggaley, Khassetarash, et al. 2022), was generated from CT scans of twenty female and twenty-eight physically active adults (18-32 years, 1.49–1.87 m, 48.3–86.0 kg). Briefly, the tibia and fibula were semi-automatically segmented in Mimics (v25, Materialise, Leuven, Belgium) and triangular surface meshes were exported. Surface node correspondence between individuals and a reference mesh were established using the Coherent Point Drift algorithm (Myronenko & Song 2010) in MATLAB (v2022a, Mathworks, MA, USA). The reference tetrahedral mesh was then elastically morphed to match each individual's bone surface geometry in Abaqus (v.2019, Dassault Systèmes Simulia Corp.; Providence, USA), establishing element correspondence. A linear relationship between Hounsfield units in the CT image and equivalent bone mineral density ($\rho_{HU}$) was calculated using a hydroxyapatite phantom (QRM GmbH; Moehrendorf, Germany) included in each scan. Density values were assigned to elements of the morphed mesh based on an average of the underlying voxels. The meshes were rigidly aligned to the reference mesh using the Procrustes algorithm. PCA was applied to the nodes to obtain a SSM and to the density values to obtain a SIM. To account for correlations between shape and density, a further PCA was applied to a

combined matrix containing shape and intensity parameters, weighted to normalise the total variance in each set, to obtain a SAM. Plots illustrating model accuracy, compactness, and generalization are shown in Appendix B (Figures B2-B4).

The new cohort's data were processed using the same methods described above from CT segmentation up to and including assigning density values to each element. The SAM was fit to the new meshes using all principal components (PCs) with a two-stage approach. An iterative approach minimizing the sum of squared distances between model and target nodes was used to obtain an initial estimate of PC weightings (Cootes & Taylor 2004). These weightings were then used as the initial guess for an optimization performed using the BFGS algorithm (Dong C. Liu & Jorge Nocedal 1989). The SAM was morphed along the PCs and rigidly aligned to the new meshes. The optimization minimized a weighted sum of squared node coordinate and density errors:

$$D = \sum 4.93 \left(\frac{n_i}{10}\right)^2 + d_i^2 \tag{4.1}$$

where $n_i$ is the distance between the $i^{th}$ model and target node, and $d_i$ is the difference between the $i^{th}$ model and target density values. Distances between nodes were divided by ten to account for magnitude differences between node and density information. The node data were multiplied by a weighting factor (4.93, the ratio of the number of elements to the number of nodes) to account for the difference in the number of data points between node and density information. Geometry and density fitting errors were calculated as the RMSE between the CT-based mesh and fitted approximation.

Fitted PC scores were compared between females and males using t-tests. The average female and male geometries and density distributions were calculated, normalizing for isotropic scaling and associated geometry and density distribution variations (Figure S1 in supplemental material of (Bruce, Baggaley, Khassetarash, et al. 2022)) by removing the first PC from each

individual's fitted data. The first PC was strongly related to height ($r^2 = 0.82$) and body mass ($r^2 = 0.48$). Sex-related variations in geometry and density distribution were visually compared to the variations observed in the previous study's cohort (the "model cohort").

### *4.2.2 Finite element modeling*

Finite element models of the average female and male were generated as previously described for the model cohort (Bruce, Baggaley, Khassetarash, et al. 2022). Briefly, mesh elements were converted to second-order tetrahedral elements. Orthotropic linear-elastic material properties were assigned to each element based on binned element density. The elastic modulus of bone in the axial direction was calculated as a function of element apparent bone mineral density ($\rho_{app} = \rho_{HU}/0.626$) (Dalstra et al. 1993):

$$E_3 = 6570 \cdot \rho_{app}^{1.37} \tag{4.2}$$

The other constants were obtained assuming constant anisotropy: $E_1 = 0.574 \cdot E_3$, $E_2 = 0.577 \cdot E_3$, $G_{12} = 0.195 \cdot E_3$, $G_{23} = 0.265 \cdot E_3$, $G_{31} = 0.216 \cdot E_3$, $\nu_{12} = 0.427$, $\nu_{23} = 0.234$, $\nu_{31} = 0.405$, where subscripts 1-3 denote the medial-lateral, anterior-posterior, and axial directions, respectively (Rho 1996). Pinned boundary constraints were applied at the knee and ankle. The distal tibia-fibula joint was modeled as rigid with surface-based tie constraints (Haider et al. 2020). The proximal fibula was connected to the tibia using two spring elements representing the anterior and posterior ligaments (stiffness of 133 N/mm and 109 N/mm, respectively) (Marchetti et al. 2017).

Ankle joint contact force and muscle forces representing loads during running at 3.3 m/s at the time of peak resultant ankle joint contact force were calculated from motion capture and force platform data from one female participant (age = 24 years, mass = 59 kg, height = 170 cm) using an inverse dynamics-based static optimisation approach. A musculoskeletal model of the pelvis and lower limb containing forty-five muscles (Arnold et al. 2010) was scaled to the

participant's segment lengths and body mass. Muscle forces were computed such that the sum of muscle moments at each joint was equal to the net joint moment computed from inverse dynamics. The following moments were used as constraints in the optimization: flexion-extension and abduction-adduction moments at the hip, flexion-extension moment at the knee, flexion-extension moment at the ankle, and the pronation-supination sub-talar moment. The optimization minimized the sum of muscle stresses squared. Muscle and joint contact forces were then scaled by body mass to the mean of the SAM training set (65 kg). Ankle joint contact force and a residual moment term about the sagittal and axial axes accounting for moments generated by muscles not attached to the tibia or fibula (e.g., the gastrocnemius muscles) as well as contact from neighboring segments were applied to the FE models at the ankle center of rotation (Haider et al. 2020). Muscle forces were applied to the FE models as concentrated forces. Muscle attachment points were determined by aligning the SAM mean mesh with the musculoskeletal model geometry and mapping each muscle insertion to the nearest surface point. The same joint contact and muscle forces were applied to the average female and male models.

Finite element models were solved in Abaqus. As previously described (Bruce, Baggaley, Khassetarash, et al. 2022), pressure-modified von Mises strain was calculated for elements containing bone (element density values ≥ 0.5 g/cm3) in the tibial diaphysis, defined as 20-80% of the length of the tibia (Edwards et al. 2015), using custom MATLAB scripts. Elements within a 1.0 cm radius of the soleus force application and a 0.5 cm radius of other muscle force application points, including transcortical elements, were removed from the analysis due to artefactually high strains (over 10 000 με). The removed elements represented less than 2% of the tibial diaphysis volume. The 95$^{th}$ percentile (peak) strain and strained volume, defined as the volume of elements experiencing strain greater than or equal to 4000 με, were quantified for each model. Absolute

differences were calculated by subtracting the peak strain and strained volume values of the average male model from the average female model. Percentage differences in peak strain and strained volume between the average female and male were also quantified. These differences observed in the new cohort ('validation cohort') were qualitatively compared to the results observed in the model cohort.

## 4.3 Results

### *4.3.1 Fitting accuracy*

Mean geometry and density fitting errors of the SAM were 1.60 ± 0.31 mm and 0.114 ± 0.018 g/cm$^3$, respectively. The largest errors in shape tended to occur at the proximal and distal epiphyses and the largest density errors tended to occur at the endocortical surface (Appendix B, Figure B.1).

### *4.3.2 Sex-related differences in bone geometry and density*

PC 3, illustrating variation in transverse cross-sectional size, differentiated between males and females ($p<0.001$), where females tended to have more positive scores (0.85 vs -0.16 SD) corresponding with narrower tibiae. Visually, the differences between the average female and male tibia and fibula are similar between the model (original study's) cohort and the validation cohort. The average female illustrated a narrower tibia and slightly greater cortical density in the diaphysis when compared to the average male (Figure 4.1). In the validation cohort, there was a greater reduction of density near the endocortical surface of the diaphysis in the average female.

### 3.3 Sex-related differences in bone strain

Differences in peak strain and strained volume between the average female and average male in the validation cohort illustrated similar trends to the model cohort (Table 4.1, Figure 4.2). The narrower tibia observed in the average female when compared with the average male was

associated with 10% greater peak strain and 80% greater strained volume. Geometry variations, rather than density variations, were responsible for the observed differences in peak strain and strained volume, (Table 4.1).

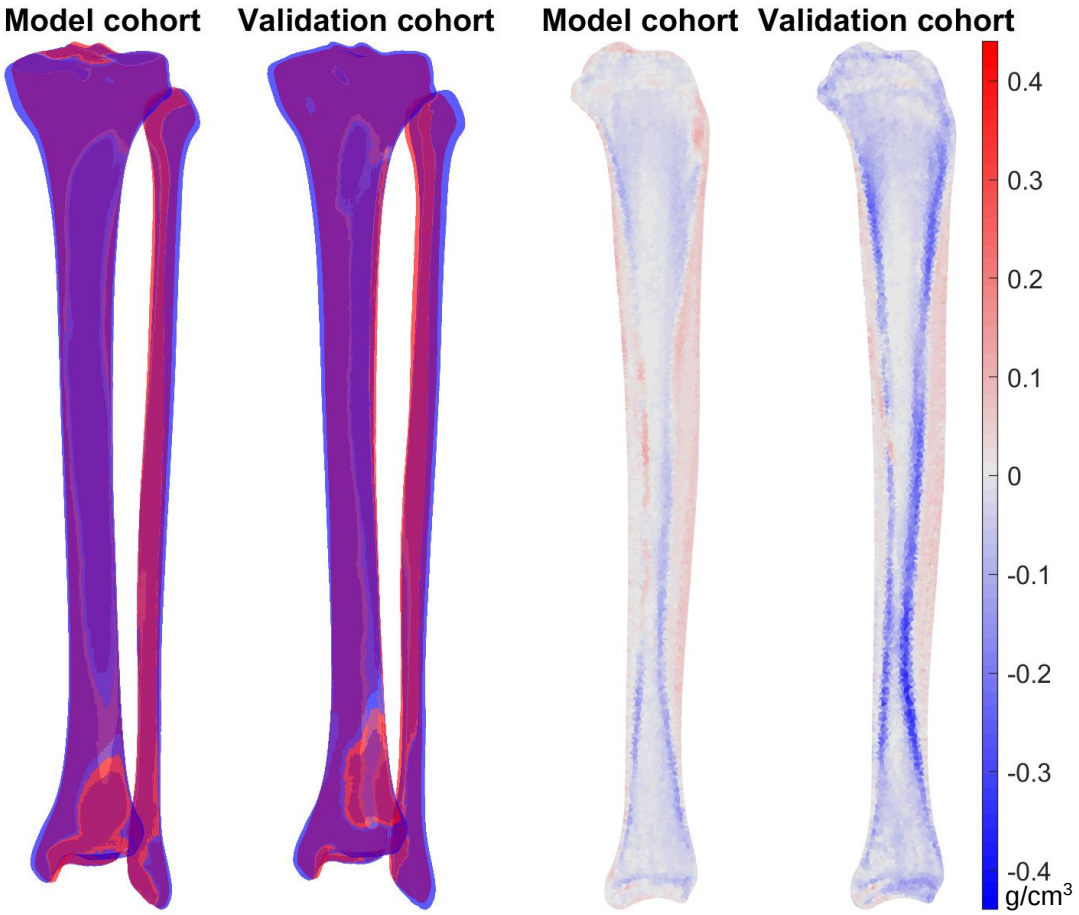


*Figure 4.1 Sex-related geometry and density differences. (Left) Periosteal geometry differences between the average female (red) and average male (blue) for the model and validation cohorts. (Right) Density differences between the average female and male for the model and validation cohorts, where positive (red) values indicate greater density in the average female when compared to the average male. The differences in geometry and density observed between the average male and average female illustrate the same patterns between the two cohorts. Density differences at the endocortical surface, influencing cortical thickness, are greater in the validation cohort when compared to the model cohort.*

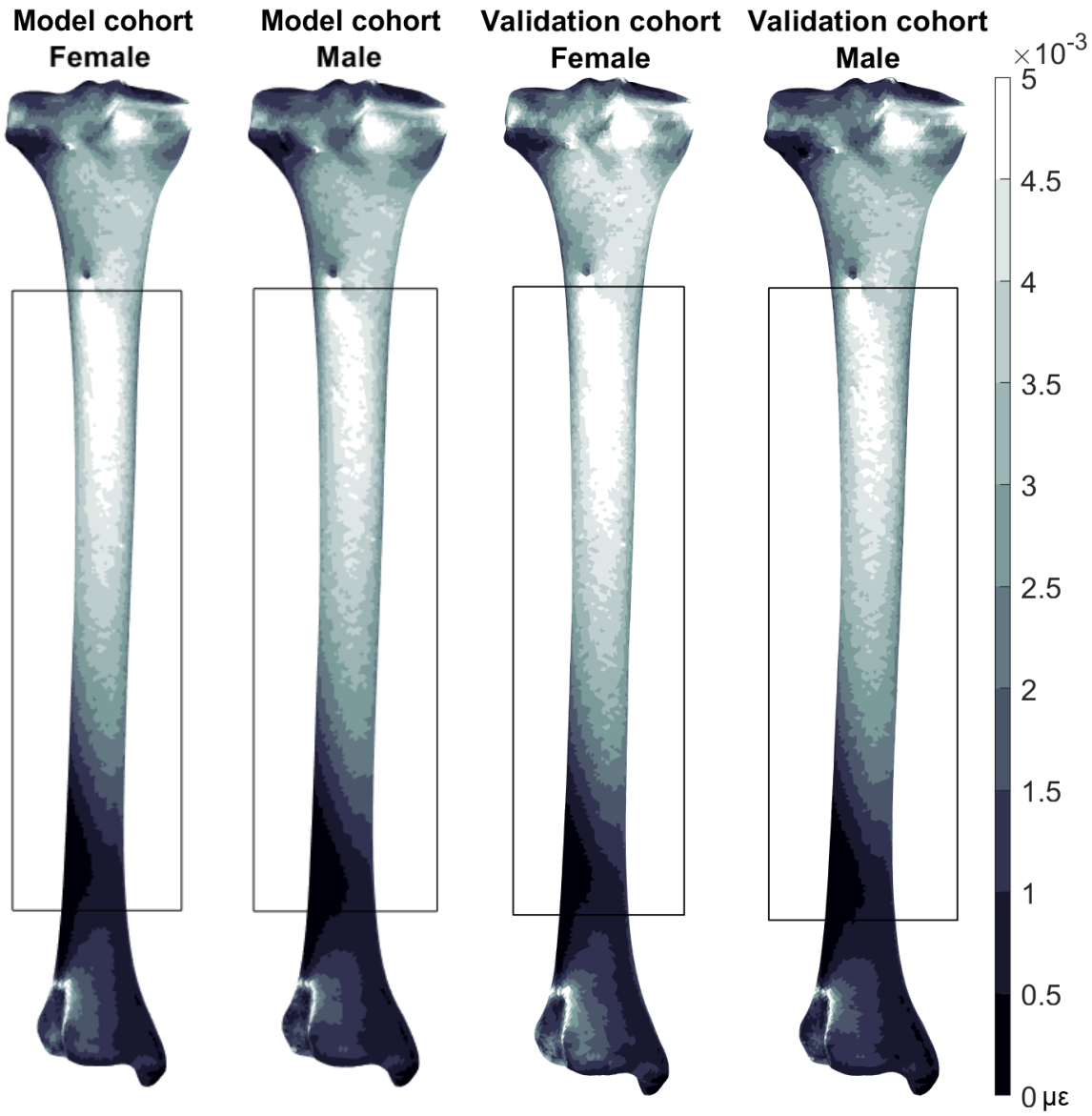


*Figure 4.2 Pressure-modified von Mises strain across the posterior surface of the tibia for the average female and male models generated from the model and validation cohorts. Bounding boxes indicate the portion of the bones included for the calculation of peak strain and strained volume. In both cohorts, strained volume (the volume of elements experiencing greater than 4000 με) was greater in the average female when compared to the average male.*

*Table 4.1 Absolute (percent) difference in peak strain (με) and strained volume ($mm^3$) in the average female when compared to the average male for the model and validation cohorts.*

| | Model cohort | Validation cohort |
|---|---|---|
| Peak strain (με) | | |
| Geometry | 645 (10) | 394 (11) |
| Density | -146 (-4) | -52 (-1) |
| Geometry + density | 198 (6) | 359 (10) |
| Strained volume ($mm^3$) | | |
| Geometry | 1678 (99) | 1973(154) |
| Density | -832 (-31) | -471 (-14) |
| Geometry + density | 831 (41) | 1675 (80) |

## 4.4 Discussion

The purpose of this study was to evaluate sex-related differences in tibia-fibula bone geometry, density, and finite element-predicted strain in young physically active adults to cross-validate a SAM of young physically active adults. Like our previously reported observations in the model cohort (Bruce, Baggaley, Khassetarash, et al. 2022), when controlled for isotropic scaling and associated geometry and density variations, the average female illustrated a narrower tibial diaphysis, reduced cortical thickness, and greater cortical density when compared to the average male. These differences resulted in 10% greater peak strain and 80% greater strained volume in the average female model. Importantly, the observed differences between the average female and male for the third PC score, geometry and density, and bone strain illustrated the same patterns as previously reported in the model cohort.

Sex-related differences in tibial geometry and density leading to elevated bone strain in the average female when compared to the average male were closely replicated by the new cohort analysed in this study, providing confidence in our previously reported results. The narrower diaphysis and thinner cortex observed in the average female resulted in higher peak strain and

strained volume when compared to the average male. Both strain magnitude and strained volume have been associated with the fatigue life of bone (Carter et al. 1981a; Pattin et al. 1996; Taylor 1998). The relationships between strain magnitude/strained volume and fatigue life are well described by an inverse power law or logarithmic function, wherein a small increase in strain magnitude or strained volume is associated with a much greater reduction in the number of cycles to failure (Edwards 2018; Haider et al. 2021). Furthermore, the largest area exhibiting high strains occurred on the posterior surface of the tibial diaphysis in both female and male models, in line with clinical data (Kijowski et al. 2012). Imaging studies suggest that tibial stress fractures most commonly occur on the posterior surface and can occur throughout the axial length of the diaphysis (Kijowski et al. 2012; Gmachowska et al. 2018). The greater strained volume observed in the average female when compared to the average male (i.e., 80% and 40% greater in the validation and model cohorts, respectively) adds strong support to the hypothesis that sexual dimorphism in tibial geometry may contribute to the elevated risk of stress fracture in females when compared to males (Nieves et al. 2005; Tommasini et al. 2007)

Differences in sex-related density distributions near the endocortical surface were more exaggerated in the validation cohort analyzed in this study when compared to the model cohort. The reduced density at the endocortical surface corresponds with a small reduction in cortical thickness relative to diaphysis diameter in the average female when compared the average male. The greater difference in cortical thickness explains, in part, the greater differences in peak strain (10% vs. 6%) and strained volume (80% vs 40%) between sexes in the validation cohort when compared to the model cohort. In addition to a narrower diaphysis, smaller cortical thickness further reduces cortical area, and second moment of area leading to increased strain.

There are several limitations of this study that should be highlighted. To isolate the influence of bone geometry and density on bone strain, we applied the same loads to all models. However, loads during running may differ between sexes and conditions. For example, Meardon et al. (2021) observed smaller axial force, larger medial-lateral force, and smaller anterior-posterior bending moment at the tibia in females when compared to males. In addition, we modeled muscle forces as concentrated forces applied to a single node in the finite element models. *In vivo,* muscles attach to bone via tendon across an area, sometimes to multiple structures. For example, the tibialis posterior originates on the fibula, tibia, and interosseus membrane (Marieb & Hoehn 2013), but was modeled at a single point on the tibia only. Muscle attachment areas may also vary between individuals and sexes (Edama et al. 2017; Kimata et al. 2022). The simplified attachment points and variations in attachment area would be expected to influence the internal moments generated by muscles. That being said, it remains unknown whether these details would be sufficient to produce changes in our peak strain and strained volume observations. Our future work will further characterise sex-related differences in running loads and muscle attachment locations, and explore the interaction between applied loads, bone morphology, and bone strain.

## 4.5 Conclusions

When controlled for isotropic scaling and associated geometry and density variations, the average female illustrated a narrower tibia, thinner diaphyseal cortex, and greater bone mineral density in the diaphysis resulting in elevated peak strain and strained volume when compared to the average male. Apart from more exaggerated differences in cortical thickness, these findings verify our previously reported observations in a completely different cohort of young physically active adults. Our findings suggest that sexual dimorphism in tibial diaphysis geometry may indeed contribute to the elevated risk of stress fracture in females when compared to males.

# Chapter 5

# A statistical shape model of the tibia-fibula complex: sexual dimorphism and effects of age on reconstruction accuracy from anatomical landmarks

## 5.1 Introduction

Musculoskeletal models are commonly used to estimate muscle forces and joint kinematic and kinetic parameters associated with human movement. Outputs from musculoskeletal models (e.g., muscle moment arms and joint contact forces) are highly sensitive to bone geometry (Scheys et al. 2008; Gerus et al. 2013; Clouthier et al. 2019; Ding et al. 2019; Xu et al. 2020), which is frequently defined using either participant-specific imaging or model scaling approaches. Advanced imaging, including computed tomography (CT) and magnetic resonance imaging, is the gold standard for quantifying participant-specific bone geometry. Of course, CT imaging requires ionizing radiation and both imaging modalities are costly and can be challenging to acquire. Consequently, it is more common to scale a 'generic' musculoskeletal model according to gross anthropometric measurements (Delp et al. 1990; Arnold et al. 2010), which does not necessarily capture potentially important differences in bone geometry among individuals.

Statistical shape models (SSM) provide an alternative method to incorporate participant-specific bone geometry into musculoskeletal models. A SSM numerically calculates the average

and principal modes of variation of a shape (e.g., bone geometry) from a training set of models (Audenaert et al. 2019). These models can be used to reconstruct participant-specific geometry from incomplete information by morphing the average shape along the modes of variation to best fit the target data. In this way, the pelvis, femur, tibia-fibula complex, and multiple bones of the foot have been reconstructed from select anatomical landmarks identified either on the bone surface or using skin-mounted motion capture markers (Zhang et al. 2016; Grant et al. 2020; Nolte et al. 2020).

Bone geometry is known to vary as a function of age and sex, among other factors (Ruff & Hayes 1988; Stevens & Vidarsdóttir 2008; Mahfouz et al. 2012; Li et al. 2014; Brzobohatá et al. 2015; Brzobohatá et al. 2016; Audenaert et al. 2019). Indeed, periosteal expansion increases with age, although to a lesser degree in females than males (Ruff & Hayes 1988; Jee 2001). At the tibia, observed geometric differences between males and females include: greater protrusion of the tibial tuberosity, diaphyseal curvature, diaphyseal cross-sectional properties (Smock et al. 2009; Feldman et al. 2012; Sherk et al. 2012), condyle size (Mahfouz et al. 2012; Audenaert et al. 2019; Tümer et al. 2019), and metaphyseal slope (Brzobohatá et al. 2015; Brzobohatá et al. 2016). These differences have been used to classify bones into age and sex- specific groups with 61-98% accuracy, depending on the study (Stevens & Vidarsdóttir 2008; Brzobohatá et al. 2015; Brzobohatá et al. 2016; Audenaert et al. 2019).

Previous studies reconstructing the tibia-fibula complex from anatomical markers used participant groups with wide age ranges (20-70 years in Nolte et al. (2020) and 15-92 years in Zhang et al. (2016)) to train and test the SSMs. While these SSMs may be more widely generalizable, a model more specific to a population of interest such as young healthy adults - a

commonly used group in biomechanics modelling studies - may provide more accurate results. Furthermore, these studies have not investigated how errors in shape influence musculoskeletal modelling parameters. Thus, the primary purpose of this study was to evaluate the accuracy of tibia-fibula complex reconstructions from anatomical bony landmarks using a SSM developed for a healthy, young adult population and quantify the subsequent effects on muscle moment arms. Errors associated with isotropically scaling the average model were also quantified for comparison. In line with previous literature (Zhang et al. 2016; Nolte et al. 2020), we hypothesized that reconstruction errors would be smaller for the SSM-generated geometries compared to isotropic scaling. The secondary objectives of this study were (1) to quantify sex differences in bone geometry, and (2) to evaluate the generalizability of the developed young adult SSM to older adults. We expected to observe differences in size and shape between young adult males and females. Due to age-related differences in bone geometry, we hypothesized that reconstruction errors and changes in muscle moment arms would be larger for the older adults.

## 5.2 Materials and methods

### *5.2.1 Model development*

Forty-one physically active participants (22 F and 19 M, 18-23 years, physically active at least three times per week) were recruited to obtain a range of statures (mean (range), female: 1.66 m (1.49 – 1.80 m), 59.7 kg (47.7-71.8 kg), male: 1.77 m (1.62 – 1.87 m), 71.8 kg (60.0 – 83.7 kg)). CT scans of the left lower leg were obtained using a GE Revolution GSI (GE Healthcare, Waukesha, WI) with image acquisition settings of 120 kVp and 180 mA. Images were reconstructed with an in-plane resolution of 0.488 mm x 0.488 mm and a slice thickness of 0.625 mm. Ethics approval was obtained from the university's Conjoint Health Research Ethics Board and written, informed consent was obtained from each participant prior to scanning.

The tibia and fibula geometries were segmented using a semi-automatic procedure and surface meshes were created in the Mimics Innovation Suite (v21, Materialise, Leuven, Belgium). Nodal correspondence and registration were performed in MATLAB (R2020a, Mathworks, MA, USA). A template mesh was selected, corresponding to an individual with tibia/fibula surface area close to the sample mean, and contained 3874 and 2111 nodes for the tibia and fibula, respectively. A sensitivity analysis, evaluating shape errors resulting from the template deformation step, was used to determine the number of nodes for the tibia and fibula. Nodal correspondence between meshes was established using the Coherent Point Drift algorithm (Myronenko & Song 2010). This algorithm performs translation, rotation, scaling, and local deformation to match a moving point-set (template) to a fixed point-set (participant surface). A nearest neighbours algorithm was used to identify corresponding points. A preliminary analysis of nodal correspondence registration errors and the number of principal components (PCs) needed to explain 95% of the variance demonstrated these measures were insensitive to the choice of template. Tibia and fibula point clouds were then combined and rigidly aligned using a generalized Procrustes analysis that retained bone size. The tibia and fibula were modelled together to include relative positioning between the two bones within the model.

A principal component analysis (PCA) was applied to the registered data to obtain the average shape and modes of variation (i.e., PCs) for the sample. An analysis described by Mei *et al*. (2008) evaluating bootstrap stability on mode direction and comparison with noise was used to determine the number of PCs to retain. Eight PCs accounting for 96.2% of the total variance in the model were ultimately retained. Scores for each retained PC were compared using unpaired t-tests to determine if and how size and shape differed between sexes (SPSS v.26, IBM, NY, USA, $\alpha = 0.05$). Centroid size, the square root of the sum of squared Euclidean distances of all points in

a shape from the centroid of the shape, was calculated. Pearson correlations were used to evaluate whether PC scores were correlated with size.

### *5.2.2 Landmark-based reconstruction*

The tibia-fibula SSM meshes were reconstructed based on two sets of anatomical landmarks (Figure 5.1). The first set contained nine landmarks that could be identified through palpation, and thus used to estimate tibia and fibula geometries from skin-mounted motion capture markers: tibial tuberosity, medial condyle, lateral and medial malleoli, lateral aspect of the head of the fibula, anterior border of the tibia at 25%, 50% and 75% of the distance between the medial condyle and malleolus markers, lateral fibula diaphysis at 25% of the distance from the lateral malleolus to the lateral point on the head of the fibula. The second set contained the nine "palpable" landmarks described above as well as another five landmarks that could not be palpated, but could be captured through imaging, to determine if additional information regarding dimension and curvature improved reconstruction accuracy: posterior aspect of the medial condyle, posterior aspect of the mid-diaphysis (50%) of the tibia, apex of the fibular head, fibular diaphysis at 50% (posterior) and 85% (anterior) of the distance between the lateral malleolus and the lateral point on the fibular head. Both sets of landmarks (Figure 5.1) were manually digitised on the average shape as well as each participants' CT-based bone surface meshes in MATLAB (R2020a, Mathworks, MA, USA).

A leave-one-out analysis was performed, where each participant was removed from the SSM and reconstructed from the digitised landmarks. The average point cloud was fit to the participant's landmarks using rigid-body rotation, translation, and deformation along the PCs using a Limited-memory Broyden-Fletcher-Goldfarb-Shanno (L-BFGS) algorithm (Liu & Nocedal

1989). The objective of the optimization was to minimize the squared Euclidean distance between reconstructed and target landmarks, which was performed using each set of landmarks (Figure 5.1). Tibia/fibula geometries were also generated by isotropically scaling the average point cloud. The scaling factor was the ratio of the distance between the lateral malleolus and lateral fibular head markers for the average shape and target data.

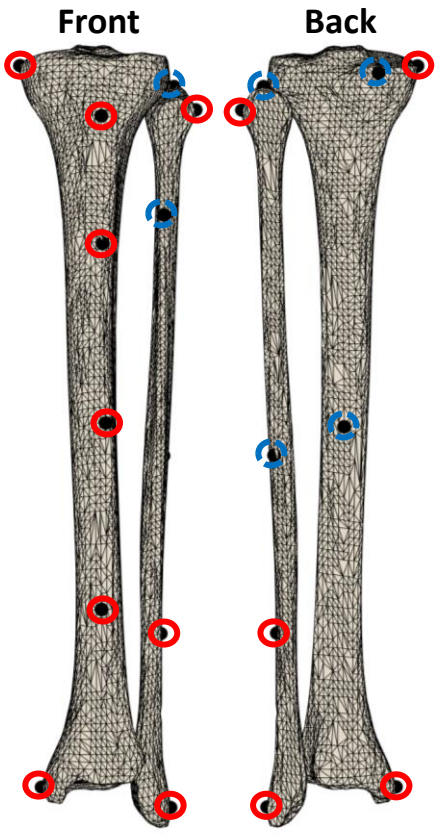


*Figure 5.1 Landmarks used for reconstructions. The subset of nine palpable landmarks are circled in red. The five non-palpable landmarks are circled in blue (dashed line).*

### *5.2.3 Generalizability to older individuals*

A dataset of bilateral lower-limb CT scans from 10 human cadavers (81.8 ± 10.7 years, 6 male, 4 female) was used to examine the robustness of the SSM when applied to an entirely new

sample. Scans were performed using a GE Revolution GSI (GE Healthcare), with image acquisition settings of 120 kVp, 103 mA, in-plane resolution of 0.67 mm x 0.67 mm, and slice thickness of 0.625 mm. The same procedures described above were used to segment and generate surface meshes of the left tibia and fibula. In one of the scans, part of the left tibia/fibula was outside of the field-of-view. In this case, the right tibia/fibula geometries were segmented and mirrored. Landmarks, previously defined (Figure 5.1), were digitised on the bone surfaces. Tibia and fibula geometries were reconstructed using nine and fourteen landmarks with the optimization procedure described above. The average shape from the shape model was also isotropically scaled.

### *5.2.4 Musculoskeletal modelling*

A musculoskeletal model was implemented in MATLAB (Mathworks, Natick, MA) and used to obtain moment arms of eighteen muscles attaching to the tibia and fibula (Appendix C, Table C.3). Initial geometry and muscle parameters were obtained from Arnold et al. (2010). The average shape from the SSM was rigidly aligned and scaled to the generic tibia and fibula of the musculoskeletal model. The surface nodes corresponding to muscle origin or insertion points were determined using a nearest neighbours algorithm.

The musculoskeletal model was scaled using markers that were digitized on the model at the lateral malleolus and head of the fibula. Reconstructed and CT-based surfaces were rigidly aligned to the scaled musculoskeletal model. The musculoskeletal model was then moved through a physiologic range of motion about the flexion-extension axis at the knee (0° to 142° flexion) and the ankle (15° dorsiflexion to -62° plantarflexion) (Soucie et al. 2011). Translations at the knee along the anterior-posterior and longitudinal axes changed as a function of knee flexion; no translations were allowed at the ankle. Muscle moment arms were computed using the tendon

excursion method. The model was positioned at each joint angle, and then perturbed by ± 10°. The moment arm of each muscle was calculated from the change in muscle length divided by the change in joint angle. Patellar ligament moment arm was calculated as the perpendicular distance from the knee joint centre to the line of action of the ligament. Maximum difference in moment arm compared to the model using the CT-based geometry was calculated.

### *5.2.5 Statistics*

Reconstructed geometries were aligned with the participants' CT-based surface meshes using a rigid iterative closest points algorithm. A nearest-neighbour algorithm was used for each node to calculate root mean square error (RMSE) and maximum distance error. Jaccard index, a measure of volumetric similarity - where values range from 0 (no similarity) to 1 (identical) - was also computed (Real & Vargas 1996). RMSE and maximum error were also calculated for the tibia and fibula separately, and for proximal, diaphysis, and distal regions (0-20%, 20-80%, and 80-100% of the axial length, respectively (Edwards et al. 2013)). Statistical tests were performed using SPSS (v26, IBM, NY, USA). In the leave-one-out analysis, error measures for at least one of the reconstruction methods did not meet the assumption of normality as defined by the Shapiro-Wilk test. Therefore, related-samples Friedman's analysis of variance tests (ANOVA) were used to evaluate differences in error measurements between reconstruction methods (9 landmarks, 14 landmarks, isotropic scaling); pairwise comparisons were used when appropriate. For the older adult dataset, all error measures met the assumption of normality. In this case, repeated measures ANOVAs were used to evaluate differences in error measurements between reconstruction methods; again, pairwise comparisons were used when appropriate. Critical values for statistical tests were adjusted for multiple comparisons using Bonferroni corrections to maintain a familywise error rate of $\alpha = 0.05$.

## 5.3 Results

The first PC in the SSM primarily captured differences in overall size and explained 79.8% of the total variance in the model (Table 5.1). The first eight components explained 96.2% of the variance (Table 5.1).

*Table 5.1 Percent of total variance explained by principal components 1-8.*

| *Principal component* | *1* | *2* | *3* | *4* | *5* | *6* | *7* | *8* |
|---|---|---|---|---|---|---|---|---|
| *Variance explained (% of total)* | 79.8 | 4.7 | 3.6 | 3.1 | 1.7 | 1.4 | 1.2 | 0.7 |
| *Cumulative variance explained (% of total)* | 79.8 | 84.5 | 88.1 | 91.2 | 92.9 | 94.3 | 95.5 | 96.2 |

### *5.3.1 Sexual dimorphism*

PC 1 discriminated between males and females ($t = 4.727$, $p < 0.001$, whereby the tibia and fibula were larger in males. PC 1 was the only mode correlated with centroid size, with $r^2 = 0.99$. Sex differences in PCs 4 and 7 trended toward significance ($t = -2.231$, and $-2.279$, $p = 0.031$, and 0.029, respectively; Bonferroni-adjusted critical p-value = 0.05/8 comparisons = 0.006; Figure 5.2). These PCs described shape differences including larger proximal epiphyseal regions, a more prominent tibial tuberosity, and more acute anterior-posterior curvature in the tibia in males compared to females (Figure 5.2).

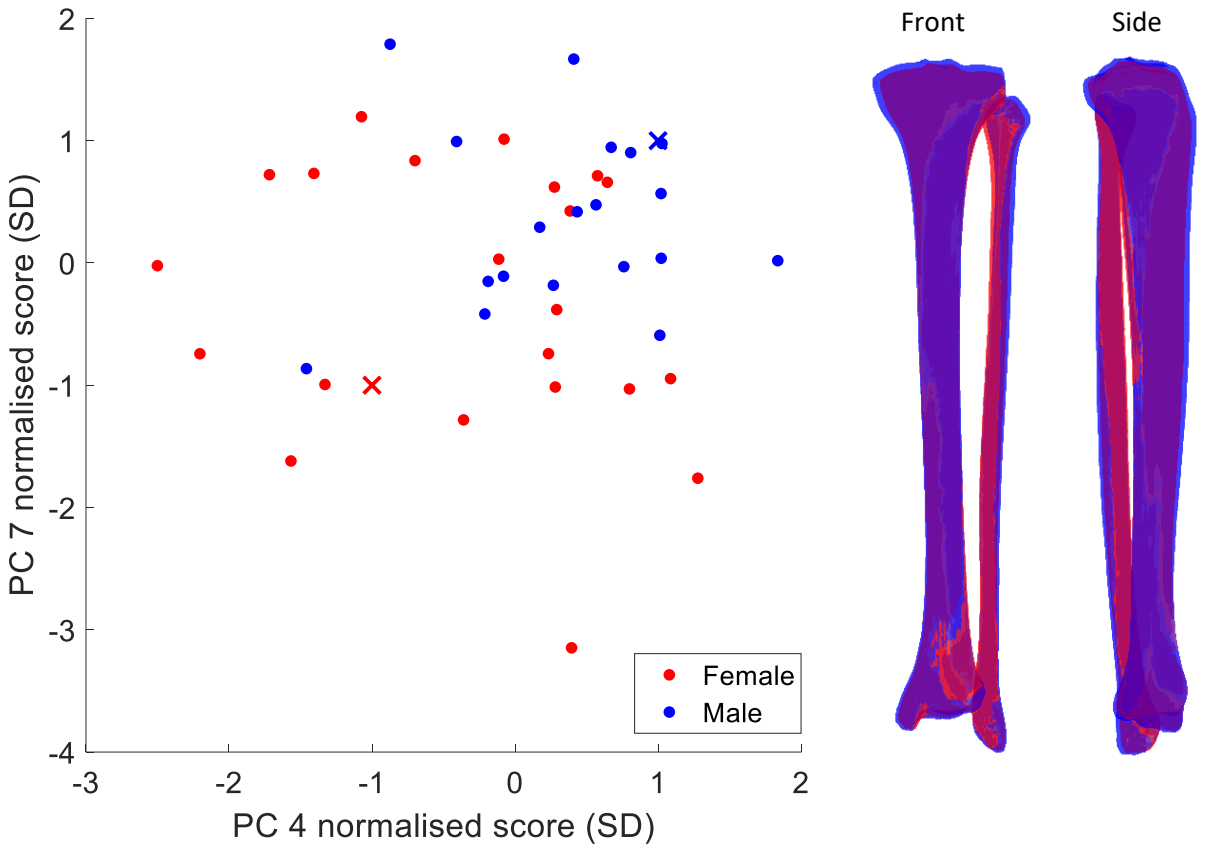


*Figure 5.2 Sex-related geometry differences detected by the SSM. (Left) Scatterplot of principal components 4 and 7 normalised scores. Red circles (female) and blue circles (male) represent individual participants. The x's represent the average shape + (blue) or – (red) 1 standard deviation (SD) for both principal components (PC) 4 and 7. (Left) Representations of the tibia-fibula complex geometry of the blue and red x's. Sex differences in shape were very subtle. ± 1 SD was larger than mean normalised scores for females (PC4 = -0.31, PC7 = -0.31) and males (PC4 = 0.36, PC7 = 0.35) and was used to more easily visualise differences.*

### *5.3.2 Reconstruction accuracy*

Differences in error between reconstruction methods were observed for RMSE ($\chi^2$ = 55.073, $p < 0.001$), Jaccard index ($\chi^2$ = 58.098, $p < 0.001$), and maximum error ($\chi^2$ = 24.927, $p < 0.001$) (Figure 5.3 and 5.4). Median (IQR) errors were smaller in SSM reconstructions using nine landmarks (RMSE = 1.62 (0.35) mm, maximum error = 5.12 (1.63) mm) compared to isotropic scaling (RMSE = 1.78 (0.62) mm, maximum error = 5.84 (2.62) mm, $p < 0.001$). Jaccard index

was greater in SSM reconstructions from nine landmarks (0.824 (0.038)) compared to isotropic scaling (0.792 (0.077), $p < 0.001$). The same pattern was observed between SSM reconstructions from fourteen landmarks (RMSE = 1.15 (0.29) mm, maximum error = (4.82 (1.26) mm, Jaccard index = 0.833 (0.034)) compared to isotropic scaling ($p < 0.001$). Differences between SSM reconstructions using nine and fourteen landmarks were also significant, where RMSE was 6.8% smaller and Jaccard index was 1.1% larger in reconstructions using fourteen landmarks ($p < 0.001$). A similar pattern of results was observed when comparing errors between reconstruction methods for specific regions of the tibia and fibula (see Appendix C, Table C.1). Shape errors tended to be larger in the fibula than the tibia, and in the proximal region.

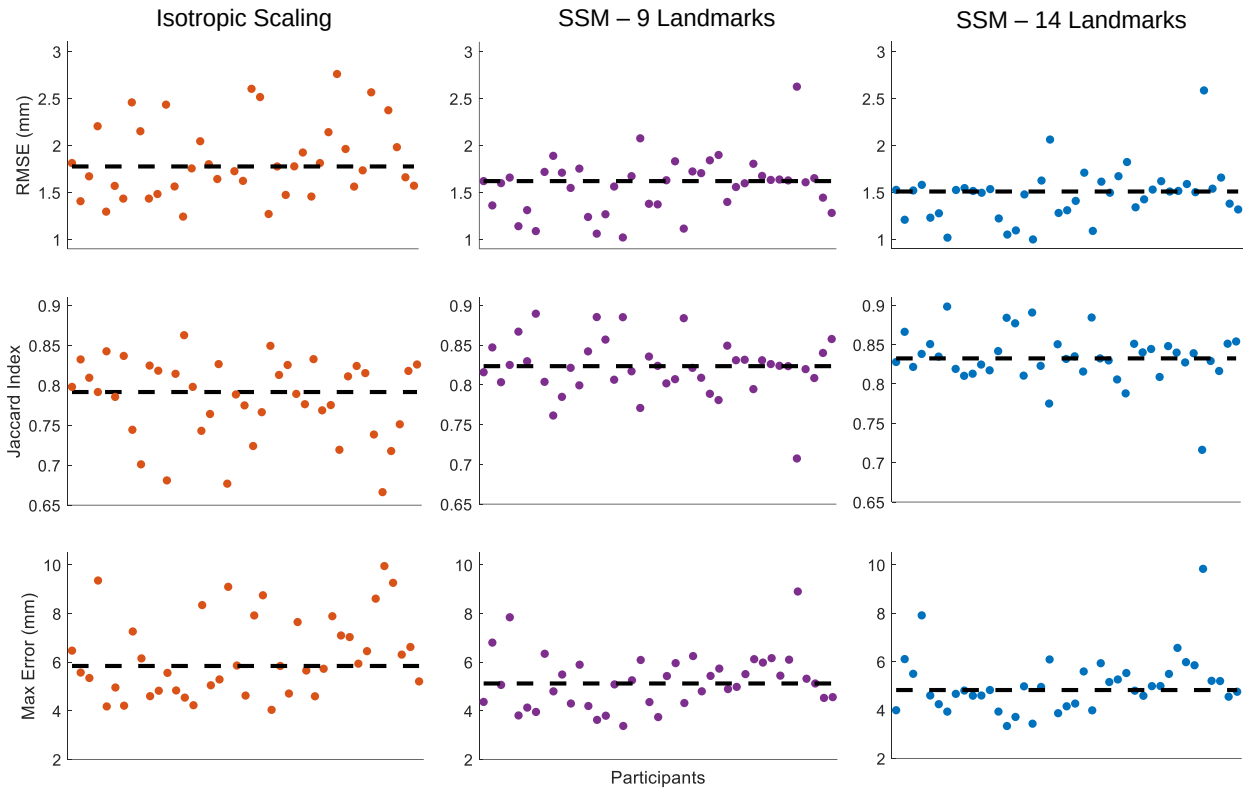


*Figure 5.3 Errors and volume similarity of tibia and fibula geometries predicted using isotropic scaling or SSM-landmark reconstruction methods compared to CT data. Dots represent individual participants. The highlighted dots are an outlier. The dashed line represents the median. Differences between SSM-landmark methods and isotropic scaling were significant for all three measures. Differences between 9 and 14 landmark reconstructions were significant for RMSE and Jaccard index.*

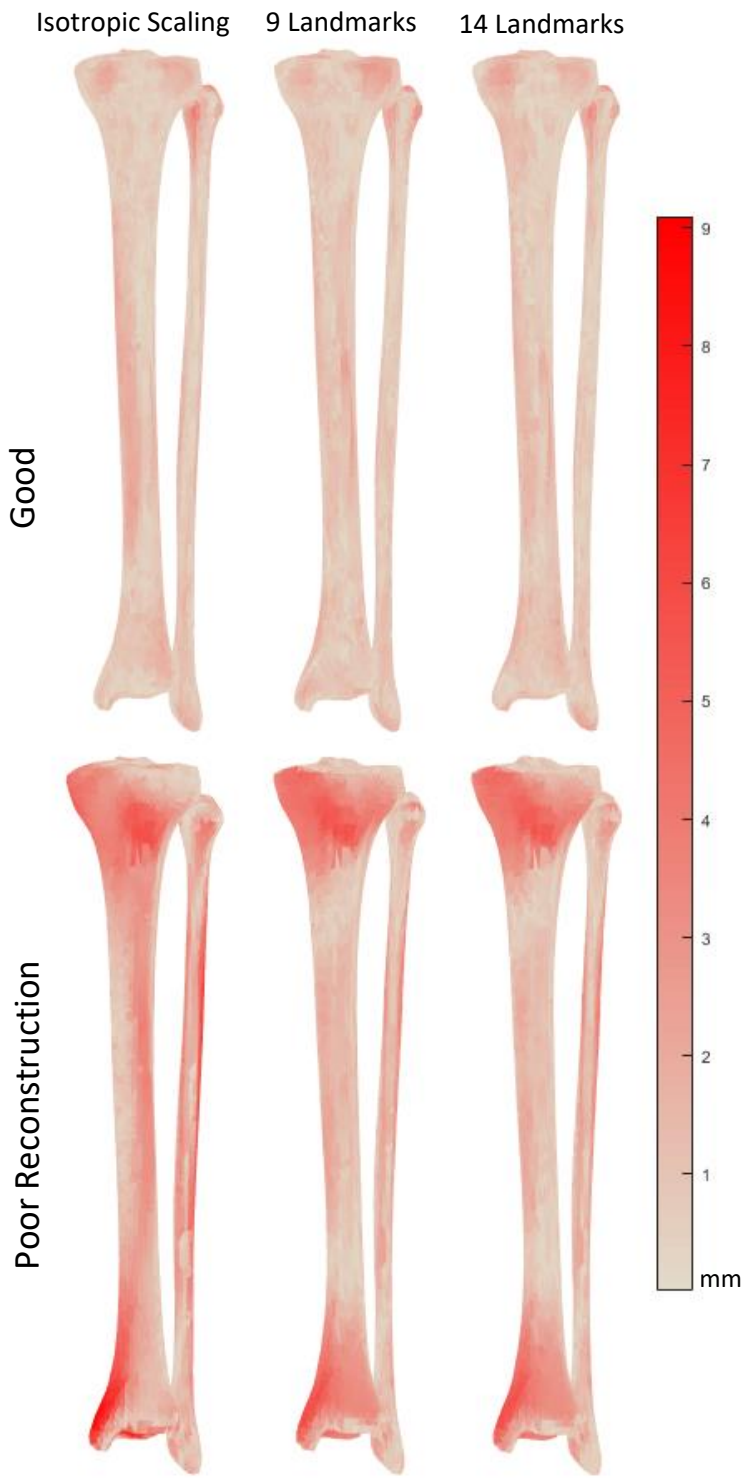


*Figure 5.4 Good (top, participant 14) and poor (bottom, participant 19) reconstructions for isotropic scaling and SSM-landmark methods.*

### *5.3.3 Generalizability to older adults*

Differences between reconstruction methods for older adults were also observed for maximum error ($F = 14.047$, $p = 0.004$, $\eta^2 = 0.609$, Figure 5.5 and 5.6), and Jaccard index ($F = 14.379$, $p = 0.004$, $\eta^2 = 0.615$). Mean (SD) maximum errors were smaller in SSM reconstructions using nine landmarks (6.90 (1.00) mm) compared to isotropic scaling (9.21 (2.36) mm, $p = 0.005$). Jaccard index was greater in SSM reconstructions from nine landmarks (0.769 (0.032)) compared to isotropic scaling (0.672 (0.077), $p = 0.004$). The same pattern was observed between SSM reconstructions from fourteen landmarks (maximum error = 7.04 (1.03) mm, Jaccard index = 0.763 (0.037)) compared to isotropic scaling ($p \leq 0.005$). Regional analysis indicated that differences in maximum error were driven by improvements in the proximal region of the tibia (Appendix C, Table C.1). No differences in error measures were observed in the fibula. Pairwise comparisons between SSM reconstructions and isotropic scaling for RMSE for the tibia and fibula combined were not significant. RMSE at the proximal and distal regions of the tibia were smaller in SSM reconstructions when compared to isotropic scaling ($p \leq 0.001$, Appendix C, Table C.1). None of the error measures were different between reconstructions from nine and fourteen landmarks.

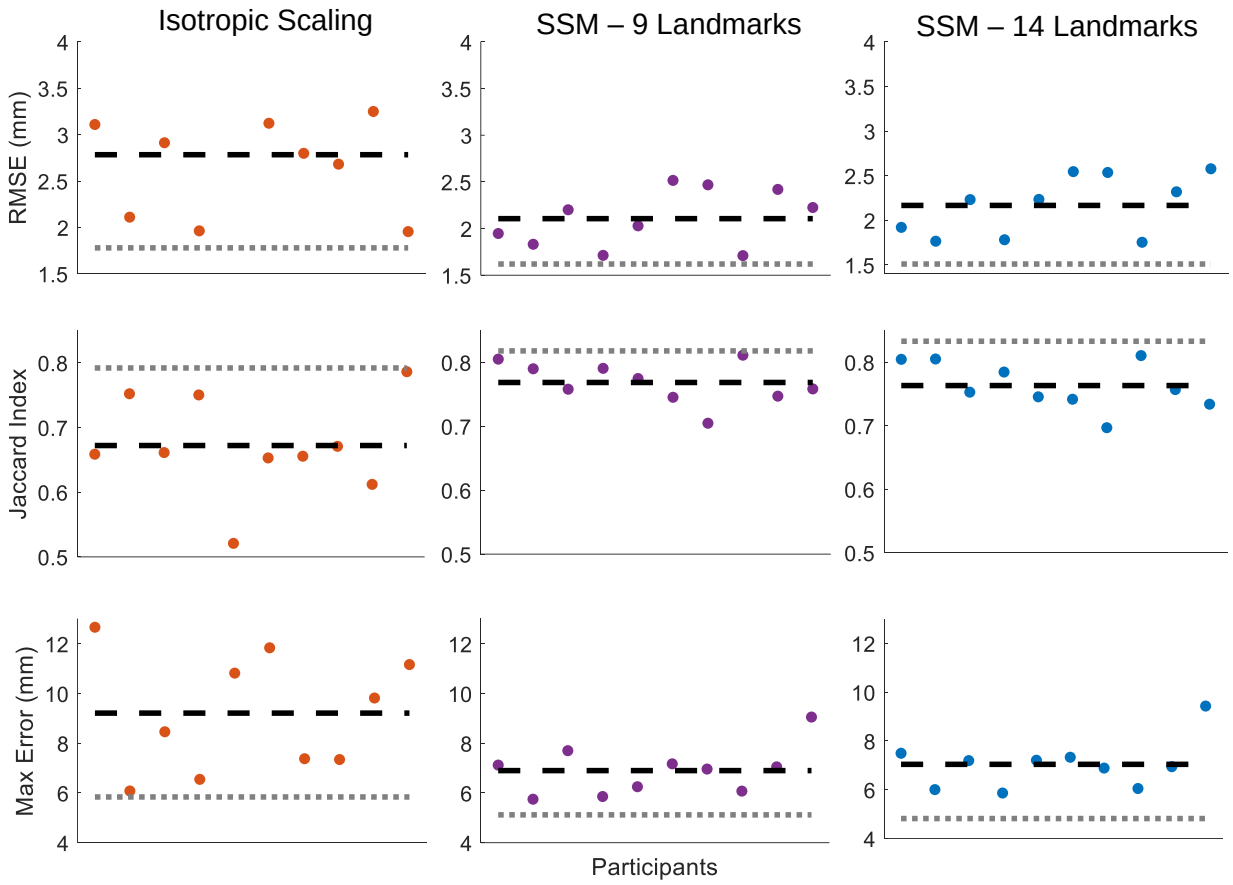


*Figure 5.5 Errors and volume similarity of tibia and fibula geometries for older individuals predicted using isotropic scaling or SSM-landmark reconstruction methods compared to CT data. Dots represent individual participants. The black dashed line represents the mean. Differences between SSM-landmark methods and isotropic scaling were significant for Jaccard index and maximum error. Errors were not different between 9 and 14 landmark reconstructions. The dotted grey line represents the median of the young adult group.*

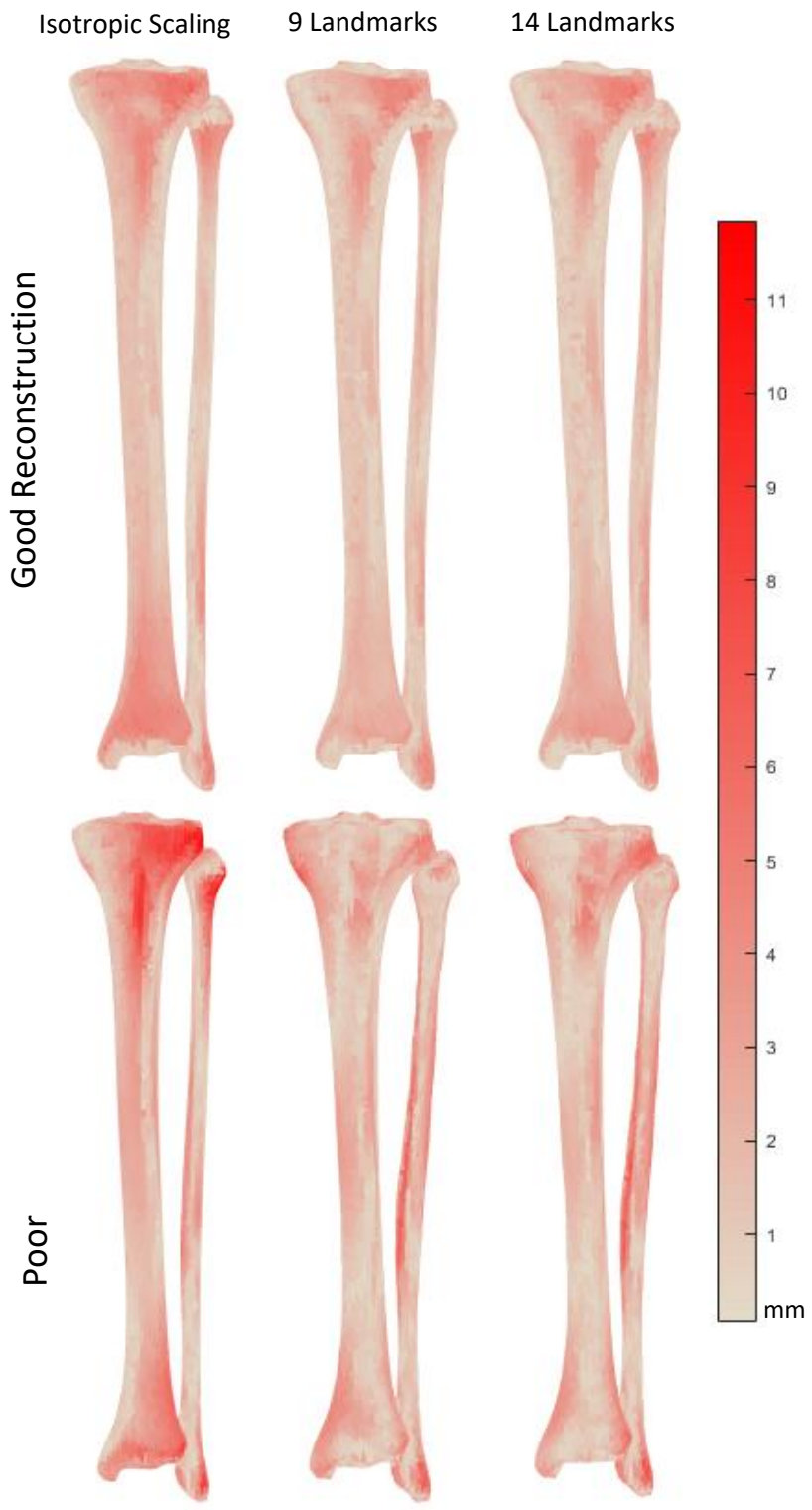


*Figure 5.6 Good (top, participant 4) and poor (bottom, participant 6) reconstructions of older participants for isotropic scaling and SSM-landmark methods.*

### *5.3.4 Muscle moment arms*

In the young adult group, the reconstruction method changed the maximum difference in moment arms, relative to the CT-based bones, of the semimembranosus, and the long and short head of biceps femoris ($\chi^2 \geq 14.244$, $p \leq 0.001$, Appendix C, Figure C.1); no differences in moment arms for other muscles originating from or inserting on the tibia-fibular complex were observed. SSM reconstructions had smaller differences in moment arms than isotropic scaling for the biceps femoris long head (median (IQR): nine landmarks = 2.36 (1.90) mm, fourteen landmarks = 2.45 (2.08) mm, isotropic scaling = 3.65 (2.90) mm, $p < 0.001$) and short head (median (IQR): nine landmarks = 3.01 (2.06) mm, fourteen landmarks = 2.74 (2.34) mm, isotropic scaling = 3.99 (3.14) mm, $p \leq 0.001$). Differences for semimembranosus were smaller in reconstructions from fourteen landmarks (2.61 (1.46) mm) when compared to nine landmarks (3.09 (2.24) mm) and isotropic scaling (3.47 (2.65) mm, $p < 0.001$). Moment arm differences in the older adults were larger than for the younger adults (4.76 – 8.33 mm vs 2.36 – 3.99 mm, respectively). No differences in muscle moment arms between reconstruction methods were observed for the older adults.

## 5.4 Discussion

The purpose of this study was to evaluate the accuracy of tibia-fibula reconstructions from anatomical bony landmarks using a SSM developed for a healthy young adult population, and quantify the subsequent effects on muscle moment arms. The secondary objectives were (1) to quantify sex differences in bone geometry within the young adult sample, and (2) to evaluate the generalizability of the developed SSM to older adults. SSM reconstructions reduced geometry errors and changed hamstring moment arms, when compared to isotropic scaling. On average, females had slightly narrower proximal epiphyseal regions and less diaphyseal curvature. SSM reconstructions, isotropic scaling, and muscle moment arms in older adults were less accurate

compared to the young adults.

Reconstruction accuracy was better in the SSM-generated models compared to isotropic scaling. The magnitude of the differences between SSM-generated reconstructions from nine and fourteen landmarks and isotropically scaled geometries in this study were somewhat small; RMSE was reduced by 0.16-0.27 mm (9-15%) and maximum error was reduced by 0.72-1.02 mm (12-17%) in SSM reconstructions compared to isotropic scaling, depending on the number of anatomical landmarks. Nolte et al. (2020) observed a larger reduction in RMSE (0.99 mm, 26%) using SSM-based reconstruction with only one PC compared to isotropic scaling, and even greater reductions in error were observed when more PCs were used. Zhang et al (2016) observed a reduction in RMSE of 0.41 mm (11%) using SSM-based reconstruction from only three bony landmarks compared to linear scaling. The low reconstruction errors observed for isotropic scaling in this study likely explains the smaller reductions in RMSE compared to previous work. Isotropic scaling was more accurate in this study (RMSE = 1.78 mm) compared to Nolte et al. (2020) (RMSE = 3.87 mm) and Zhang et al. (2016) (RMSE = 3.63 mm). In fact, the RMSE for isotropic scaling in this study was also lower than SSM-based tibia-fibula reconstruction errors observed by Nolte et al (2020) (2.88 mm) and Zhang et al. (2016) (3.22 mm). This could be explained, in part, by the small range of young participants used to create the SSM and evaluate reconstruction accuracy in this study, i.e., 18-24 years, compared to 15-92 years in Zhang et al. (2016) and 23-70 years in Nolte et al. (2020) - which likely included less geometric variability. The use of landmarks identified directly on the bone surface, as compared to skin markers may have also contributed to more accurate results when compared to isotropic scaling in previous studies.

When the SSM based on the younger group was used to reconstruct tibia-fibula geometries for the older adult group (71-98 years), errors for both isotropic scaling and SSM-based reconstructions were larger than errors for the young group. Isotropic scaling of the average young adult tibia and fibula geometries consistently underestimated cross-sectional size throughout the length of the bones in older adults, which could be explained by periosteal expansion (Ruff & Hayes 1988; Jee 2001). SSM reconstructions were able to account for some of the variation, reducing the overestimation of cross-sectional size. Although SSM-based reconstruction errors were larger in the older group than the younger group, the SSM still provided 14% and 25% reductions in Jaccard index and maximum error, respectively, within the older group, indicating greater robustness for application to new populations when compared to isotropic scaling of a generic geometry.

Geometry errors, particularly at locations affecting joint alignment and muscle attachment points, can substantially influence musculoskeletal model outcomes (Scheys et al. 2008; Gerus et al. 2013; Xu et al. 2020). RMSE and maximum errors were larger in the proximal epiphysis and metaphysis regions, where many muscles crossing the knee insert, than in the diaphysis of the tibia and fibula (Appendix C, Tables C.1 and C.2). Moment arms of some muscles attaching in the proximal regions were different when using the isotropically scaled average geometry compared to the CT-based geometry, adding support to previous findings at the knee and hip (Scheys et al. 2008; Bahl et al. 2019). In young adults, the 9-17% reductions in geometric errors from SSM-based reconstruction resulted in 25-35% reductions in maximum moment arm differences for semimembranosus and biceps femoris long and short heads. Previous work has demonstrated substantial sensitivity of muscle forces and joint contact forces to geometry (image-based vs. generic models) and perturbations of muscle insertion points and moment arms on the order of ±1

cm (Carbone et al. 2012; Gerus et al. 2013; Xu et al. 2020). The absolute changes in muscle point and maximum moment arm differences between SSM and isotropic scaling methods in this study were an order of magnitude smaller (≤1.3 mm). These differences may not translate to significant changes in muscle forces or joint contact forces, but this must be confirmed in future work. In the older adults, moment arm and muscle origin/insertion point differences relative to the CT-based model were larger: up to 8 mm and 22 mm, respectively (Appendix C, Tables C.3 and C.4). However, moment arm differences were not changed between reconstruction methods. Although SSM-reconstruction improved geometric accuracy, it was not better than isotropic scaling of a generic model for musculoskeletal modelling application in an outside population. A SSM including older adults in the training set would provide better results.

In addition to age, sex is a factor known to influence bone geometry. In this study, the scores for three PCs differentiated between sexes. While not statistically significant, likely due to the extremely conservative Bonferroni adjustment for eight comparisons, trends were observed in PCs 4 and 7. Shape differences were subtle, as these PCs accounted for very small percentages (3.15% and 1.19%) of variance in the SSM and there was overlap in the PC scores (Figure 5.2). These results are consistent with the observations of Brzobohatá et al. (2016).

A limitation of this study is that landmarks were identified directly on the bone surface. In the young adult group, using only the ‘palpable’ landmarks slightly reduced accuracy when compared to reconstructions from all 14 landmarks, but this was still 4-12% better than isotropic scaling. This illustrates the potential for a subset of landmarks that might be used to predict tibia-fibula geometry without the use medical imaging, perhaps using skin-mounted markers collected during a static motion capture trial. Of course, estimating the soft tissue offset between skin

mounted markers and bony landmarks and landmark placement errors may introduce additional uncertainty. Mean soft tissue offsets of 4.8-7.7 mm and skin marker placement inter-examiner precision of 11-20 mm have been reported for anatomical landmarks on the shank (Della Croce et al. 1999; Nolte et al. 2020). Methods have been proposed to reduce errors and improve reliability for skin marker placement (Osis et al. 2016; Hutchinson et al. 2018). Larger errors may be observed for markers on the tibia shaft, which would be placed using a measuring tape to identify 25, 50, and 75% positions along the tibial crest between the lateral malleolus and fibular head markers. An approach allowing axial movement of the tibial crest markers (Nolte et al. 2020) may reduce the effects of this source of error. Encouragingly, Nolte et al. (2020) observed small standard deviations (0.90-2.99 mm) in soft-tissue offsets for seven markers on the shank, six of which were the same or similar to landmarks used in this study. The authors reported that no differences in RMSE were observed between reconstructions from bone landmarks and skin markers digitised using an optical motion capture system, with or without soft tissue offset corrections, when one or two PCs were used. This provides some confidence that the SSM developed in this study could be used to reconstruct tibia-fibula geometries using skin-mounted markers, although additional work is needed to determine the number of PCs that could be used and to quantify the model-specific reconstruction accuracy.

The training set used in this study to create the SSM, which was composed of young active adults with no musculoskeletal abnormalities, may limit the applicability of the model to clinical or paediatric populations. Ethnicity is also a factor influencing bone geometry (Mahfouz et al. 2012). Unfortunately, ethnicity information was not collected, although most participants appeared to be of western European descent.

## 5.5 Conclusions

In conclusion, within a young physically active population, and using an average model specific to that population, isotropic scaling provided predictions of tibia and fibula bone geometry with low error. The developed SSM produced estimated tibia and fibula geometries from bony landmarks with even greater accuracy. However, this only affected the moment arms of three muscles. Geometry errors were larger in the older adult group. Although SSM-based reconstruction using a model trained on young adults was able to account for some geometric variation in an outside population, it was not sufficiently robust to alter musculoskeletal model parameters compared to a scaled generic model.

# Chapter 6

# Predicting tibia-fibula geometry and density from anatomical landmarks: influence of errors on finite element-calculated bone strain

## 6.1 Introduction

Bone strain plays an important role in the pathophysiology of stress fracture (Burr et al. 1990), a common overuse injury associated with the mechanical fatigue of load-bearing bone (Edwards 2018). Mechanical fatigue is a phenomenon wherein repetitive submaximal loading results in microdamage accumulation in the form of small cracks in the bone matrix (Burr et al. 1990). *Ex vivo* cadaveric research has illustrated that the evolution of microdamage and eventual failure of bone is a strong function of the resulting strain magnitude from the applied load (Carter et al. 1981a; Pattin et al. 1996). It is believed that stress fractures *in vivo* occur when the rate of microdamage is chronically greater than the rate of bone cellular repair (Edwards 2018; Hoenig et al. 2022).

Direct measurements of bone strain require invasive surgical procedures (Ekenman et al. 1998; Milgrom et al. 2002), therefore, bone strain is often estimated using the finite element method. The current state-of-the-art involves generating a participant-specific model from advanced medical imaging, with boundary conditions obtained from biomechanical measurements

or simulations of human movement (Haider et al. 2020). While participant-specific finite element models have illustrated bone deformations and strains consistent with direct measurements (Haider et al. 2020), the generation of these models from advanced medical imaging, typically computed tomography (CT), is often time consuming and requires technical expertise. CT imaging is required to characterise participant-specific bone geometry and material properties, and finite element-predictions of bone strain are highly sensitive to variations in these parameters (Xu et al. 2020; Bruce, Baggaley, Khassetarash, et al. 2022). Access to and cost of CT imaging are major barriers for the use of participant-specific finite element models.

Statistical appearance models (SAMs) may provide a method to generate participant-informed models in the absence of medical imaging data. SAMs of bones describe the average and principal modes of variation of geometry and density within a population represented by the model's training set (Cootes & Taylor 2004). Statistical shape models (SSMs), which characterise geometry variations only, have been used to predict tibial-fibular surface geometries from landmarks identified on the bone surface (Zhang et al. 2016; Nolte et al. 2020; Bruce, Baggaley, Welte, et al. 2022; Keast et al. 2023). These predictions were more accurate than linearly scaled generic models (Nolte et al. 2020; Bruce, Baggaley, Welte, et al. 2022). Using skin-mounted landmarks is likely to introduce additional error into model predictions. Although, Nolte et al. (2020) observed no difference in geometry accuracy between predictions from bone and skin markers when only one or two principal components (PCs) were used to non-linearly scale the tibia, greater errors were observed in skin marker-based predictions using higher-level PCs.

Studies evaluating whole-bone prediction accuracy from anatomical landmarks have been limited to SSMs that describe surface geometry only. SAMs characterise how density distribution covaries with surface geometry and density distribution errors resulting from predictions using

only anatomical landmarks remain unknown. Furthermore, the mechanical implications (i.e., bone strain) of geometry and density distribution errors resulting from landmark-based prediction methods have not yet been evaluated. Thus, the purpose of this study was to: (1) quantify errors associated with predicting tibia-fibula geometry and density distribution from skin-mounted anatomical landmarks and (2) quantify how those errors propagate to finite element-calculated bone strain. In this study we investigated modeling errors at the tibia, because it is the most common location for stress fracture (Hoenig et al. 2022).

## 6.2 Methods

Thirty young active adults (15 F and 15 M, 23.3 ± 4.3 years, 1.77 ± 0.09 m, 75.6 ± 10.0 kg) were recruited from the student population at the University of Calgary. Participants were physically active at least three times per week, had no injuries three months prior to testing, and had no contraindications for CT scanning. Participants were recruited to obtain a large range of heights to examine the model. The study was approved by the University of Calgary Conjoint Health Research Ethics board (REB21-1971). All participants provided written informed consent prior to participation.

Thirty-four retro-reflective markers were placed on landmarks of each participant's pelvis, left lower limb, and shoes by one investigator (OLB). The marker set included twelve markers on the shank: lateral and medial tibial plateau, tibial tuberosity, Gerdy's tubercle, fibula head, lateral and medial malleoli, tibial notch, three markers along the anterior tibial crest, and the lateral side of the fibula diaphysis approximately 20% along the length from the lateral malleolus (Figure 6.1). Following a static motion-capture trial, each participant performed ten trials running overground at their preferred speed (± 5%) while motion and force data were collected at 200 Hz and 1600 Hz, respectively, using an eight-camera Vicon system (Nexus v2.13, Vicon Motion Systems Ltd,

Oxford, UK) and a Kistler force platform (Kistler Instruments, Hampshire, UK). Preferred speed was calculated as the average of five runs “at a comfortable pace” along a 20 m lane passing through the capture volume, measured using timing lights. The timing lights were used tom monitor speed during each subsequent trial.

### *6.2.1 CT acquisition and processing*

On a separate day, the twelve shank markers were again placed on the participant’s left lower leg using double-sided tape by the same investigator (OLB). A CT scan of the knee, lower leg, and foot was then obtained (GE Revolution GSI, General Electric Medical System, Milwaukee, WI; acquisition settings: 120 kVp, 200 mA, in-plane resolution of 0.48 x 0.48 mm, slice thickness of 0.625 mm). The tibia and fibula were semi-automatically segmented in Mimics software (v25, Materialise, Leuven, Belgium). Skin-mounted markers were manually segmented.

Anatomic correspondence for surface nodes between participant surfaces and the reference meshes used in the generation of the SAM was established using the Coherent Point Drift algorithm (Myronenko & Song 2010). The reference meshes were then elastically morphed to match each participant’s tibia and fibula surfaces in Abaqus (v2019, Dassault Systèmes Simulia Corp.; Providence, USA). A hydroxyapatite phantom (QRM GmbH; Moehrendorf, Germany) included in all scans was used to calculate a linear relationship between Hounsfield units and CT equivalent density ($\rho_{HU}$). Each element was assigned a density value based on the underlying voxels in Mimics.

The twelve anatomic landmarks were identified on the average tibia and fibula surfaces from the SAM (Figure 6.1). For each participant, the vector between the bone-surface landmark and the centroid of the corresponding skin-mounted marker was calculated using a custom

MATLAB script (v2022a, Mathworks, MA, USA). Offsets for diaphysis markers (tibial crest, tibial notch, fibula diaphysis) were calculated as the vector between the centroid of the marker and the nearest node on the tibia or fibula surface to account for imprecise placement in the axial direction. The mean unit vector, mean, and standard deviation of the distance between bone landmarks and skin markers, removing marker radius, were calculated.

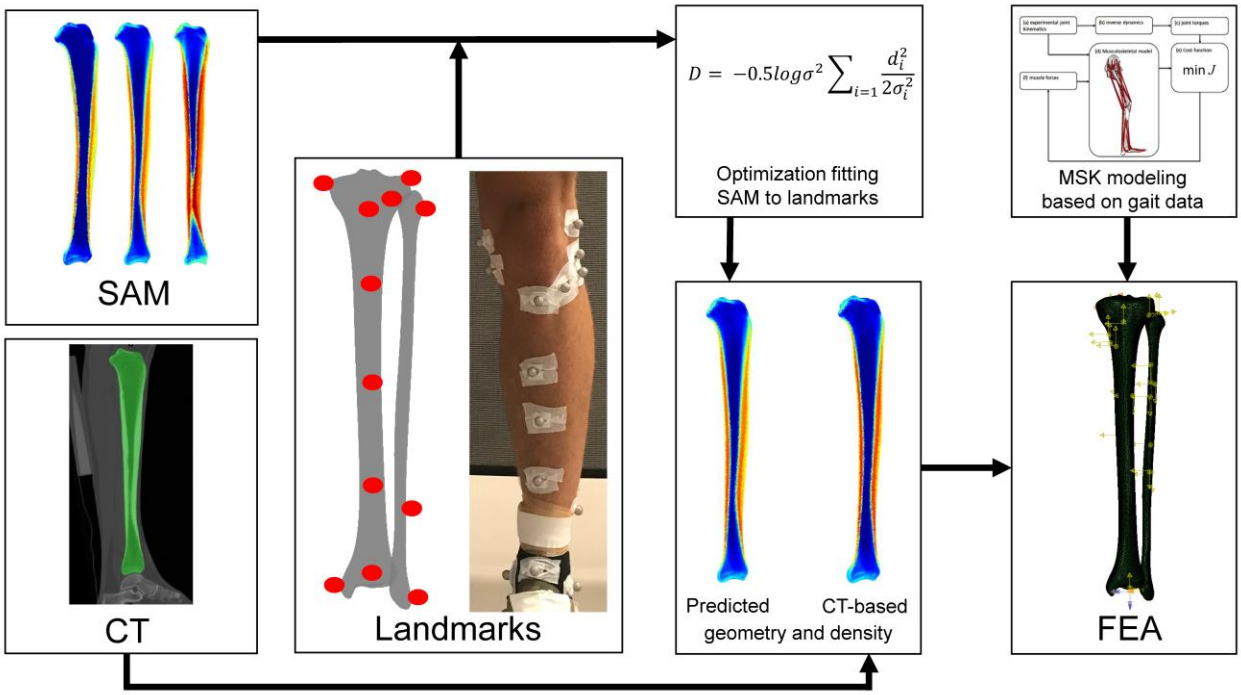


*Figure 6.1 Overview of workflow to generate participant-informed finite element models from anatomical landmarks.*

### *6.2.2 Prediction of tibia and fibula geometry and density*

First, tibia-fibula geometry and density predictions were generated from only height and sex. The first PC score was estimated from height using a linear relationship calculated from the training set of the SAM ($r^2$ = 0.82, Appendix D, Figure D.1). The mean scores for females and males were used for the rest of the PCs. Second, predictions were generated from height and anatomical landmarks (Figure 6.1). The static motion capture trial was used to obtain the target

landmark coordinates. Tibia-fibula geometry and density were predicted by morphing the SAM along the first one through five PCs and performing rigid-body transformations to match the morphed model's predicted landmarks to the target landmarks. An initial guess for the first PC was calculated from height. All other PC scores were initialised as zeroes. The optimization was performed using the BFGS algorithm in MATLAB, minimizing a negative log likelihood function of a Gaussian distribution (Nolte et al. 2020):

$$D = -0.5log\sigma^2 \sum_{i=1} \frac{d_i^2}{2\sigma_i^2} \quad (6.1)$$

where σ is the standard deviation of skin-mounted marker offsets, and $d_i$ is the distance between the target landmark and the model landmark. The position of the model landmark was calculated as the position of the bone surface landmark on the model, projected along the mean offset vector by the mean offset magnitude and marker radius. For landmarks not associated with a distinct bony feature (i.e., tibial crest, tibial notch, and fibula diaphysis markers), the nearest point on the model's surface to the target marker was used. That point was then projected to obtain the predicted model landmark.

The predicted meshes were aligned to the CT-based participant-specific mesh using the Procrustes algorithm. Prediction errors were calculated as the root mean square error (RMSE) for the Euclidean distance between corresponding surface nodes and for the difference in element density values in the predicted tibia and fibula compared to the participant-specific mesh. Based on the prediction error results, a post-hoc analysis was performed to determine if a reduced set of six landmarks (lateral and medial plateau, fibula head, tibial tuberosity, lateral and medial malleoli) to estimate the first PC would be sufficient to predict tibia and fibula geometry and density with similar accuracy.

### *6.2.3 Finite element models*

No differences in geometry or density distribution error were observed between landmark-based predictions from one through five PC. Therefore, meshes predicted from twelve landmarks and one PC, which illustrated the lowest RMSE, and from height and sex were used to evaluate the mechanical implications of geometry and density distribution prediction errors. Mesh elements were converted from first to second order tetrahedral elements. Element densities were binned (bin width = 0.010 g/cm$^3$) and used to calculate orthotropic linear-elastic material properties for each element. The elastic modulus of bone in the axial direction was calculated as a function of element apparent bone mineral density ($\rho_{app} = \rho_{HU}/0.626$) (Dalstra et al. 1993):

$$E_3 = 6570 \cdot \rho_{app}^{1.37} \tag{6.2}$$

The other constants were obtained assuming constant anisotropy: $E_1 = 0.574 \cdot E_3$, $E_2 = 0.577 \cdot E_3$, $G_{12} = 0.195 \cdot E_3$, $G_{23} = 0.265 \cdot E_3$, $G_{31} = 0.216 \cdot E_3$, $\nu_{12} = 0.427$, $\nu_{23} = 0.234$, $\nu_{31} = 0.405$, where subscripts 1-3 denote the medial-lateral, anterior-posterior, and axial directions, respectively (Rho 1996).

Boundary constraints were the same as our previous work (Bruce, Baggaley, Khassetarash, et al. 2022; Khassetarash et al. 2023). Surface nodes on the tibial plateau were kinematically coupled to rotate about a fully constrained point in the centre of the tibial plateau. A point on the medial condyle was constrained in the anterior-posterior direction. The ankle center, estimated as the mid-point between the lateral and medial malleoli, was constrained in the anterior-posterior and medial-lateral directions. Surface nodes on the tibia and fibula near the interface with the talus were coupled to the ankle center and allowed to rotate about the point. The distal tibia-fibula joint was modeled with surface-based tie constraints (Haider et al. 2020). Two spring elements were

used to model the anterior (133N/mm) and posterior (109 N/mm) ligaments at the proximal tibia-fibula joint (Marchetti et al. 2017). Nodes at the articulating surface were also tied preventing motion normal to the joint surface.

An inverse dynamics-based static optimization routine was used to calculate lower extremity muscle and joint contact forces during running based on motion and force data. Markers were used to calculate local segment coordinate systems. Cardan segment and joint angles were calculated using a flexion-extension, abduction-adduction, internal-external rotation sequence. Segment parameters were calculated using anthropometric measures and equations (Vaughan et al. 1999). Net joint moments were calculated using an inverse dynamics approach. A musculoskeletal model of the pelvis and lower limb with forty-five muscles (Arnold et al. 2010) was then scaled to match the participant's segment lengths and body mass. A constrained optimization was performed to compute muscle forces such that the sum of muscle moments was equal to the net inverse dynamics-calculated moment at each joint, minimizing the sum of muscle stresses squared. The following moments were used as constraints in the optimization: flexion-extension and abduction-adduction moments at the hip, flexion-extension moment at the knee, flexion-extension moment at the ankle, and the pronation-supination sub-talar moment. Muscle and ankle joint contact forces were calculated for each of the ten trials. The trial with the peak resultant ankle joint contact force closest to the mean of the participant's ten steps was selected. Joint contact and muscle forces at the time of peak resultant ankle contact force were applied to the finite element models. Muscle forces were applied as concentrated forces at the attachment point for each muscle originating or inserting onto the tibia or fibula. Attachment points were determined by finding the nearest surface node on the SAM average mesh aligned with the MSK model geometry. The ankle joint contact force was applied at the ankle center of rotation. Finally,

a residual moment about the sagittal and axial axes of the ankle was calculated and applied at the ankle center of rotation to account for other sources of torque such as the gastrocnemius muscles.

Finite element models were solved in Abaqus (v2019, Dassault Systèmes Simulia Corp.; Providence, USA). Pressure-modified von Mises strain, a modified formulation of the von Mises criterion shown to predict failure in quasi-brittle materials that demonstrate compression-tension strength asymmetry, was calculated for each element. The analysis was then limited to elements containing bone (element density values $\geq 0.5$ g/cm$^3$) in the tibial diaphysis, defined as 20% to 80% of the length of the tibia. Elements within a 1.0 cm radius of the soleus force application and a 0.5 cm radius of other muscle force application points, including transcortical elements, were removed from the analysis due to artefactually high strains (over 10 000 με). 95$^{th}$ percentile strain (peak strain) and strained volume, defined as the volume of elements experiencing ≥4000 με, were compared between predicted and participant-specific models.

### *6.2.4 Statistics*

Geometry and density RMSEs were not normally distributed. Friedman tests were used to evaluate differences in RMSE between reconstruction methods. When differences were found Wilcoxon signed-rank tests with Bonferroni corrections were used to test differences between pairs of reconstructions. The RMSE for strain measurements was compared between prediction methods using a Wilcoxon signed-rank test. Bland-Altman plots were constructed to evaluate agreement between predicted and participant-specific meshes, where the participant-specific mesh was the 'ground truth.' The acceptable limits of agreement were set at ± 5%.

## 6.3 Results

### *6.3.1 Skin-mounted marker offsets*

Mean distances between bone surface and skin-mounted landmarks were 5.5 - 22.9 mm. Landmarks along the tibial crest and at the lateral and medial malleoli illustrated the smallest offsets, whereas the lateral and medial tibial plateau landmarks illustrated the largest offsets (Table 6.1).

### *6.3.2 Prediction errors*

Median surface prediction RMSEs were 4.39 - 5.17 mm (Figure 6.2A). No differences were observed between prediction methods ($p = 0.933$). Median CT equivalent density prediction RMSEs were 0.116-0.142 g/cm$^3$ (Figure 6.2B). Density RMSEs were different between prediction methods ($p < 0.001$); predictions from two, four, and five cumulative PCs illustrated greater error than predictions from height and sex ($p \leq 0.003$). Surface and density RMSEs were not different between reconstructions from one PC using twelve landmarks (Median (IQR) = 4.39 (1.68) mm and 0.118 (0.046) g/cm$^3$) or six landmarks (4.59 (1.49) mm and 0.118 (0.047) g/cm$^3$, $p \geq 0.428$).

*Table 6.1 Mean and standard deviation offsets between skin-mounted markers and corresponding anatomical landmarks on the bone surface.*

| *Marker* | *Mean (mm)* | *SD (mm)* |
|---|---|---|
| Lateral plateau | 22.9 | 3.9 |
| Medial plateau | 21.6 | 4.9 |
| Tibial tuberosity | 9.0 | 2.7 |
| Gerdy's tubercle | 12.8 | 2.5 |
| Medial malleolus | 6.9 | 2.5 |
| Tibial Notch | 15.1 | 2.6 |
| Tibial crest 1 | 5.9 | 1.3 |
| Tibial crest 2 | 5.5 | 1.2 |
| Tibial crest 3 | 6.5 | 1.6 |
| Fibula head | 12.2 | 4.8 |
| Fibula diaphysis | 14.5 | 2.7 |
| Lateral malleolus | 6.5 | 1.9 |

### *6.3.3 Finite element-calculated strain errors*

Median (IQR) tibial diaphysis strain RMSEs were 492 (286) με and 476 (155) με for meshes predicted from landmarks and height and sex, respectively, when compared to results from participant-specific meshes. Strain RMSE was greater in meshes predicted from landmarks than from height and sex ($p = 0.012$). Participant-informed models illustrated poor agreement with participant-specific models for both peak strain and strained volume (Figure 6.3). The limits of agreement for peak strain were -34% to 32% and -31% to 27% for models predicted from landmarks and height and sex, respectively. The limits of agreement for strained volume were -202% to 143% and -159% to 104% for models predicted from landmarks and height and sex, respectively. No significant biases were observed ($p \geq 0.20$).

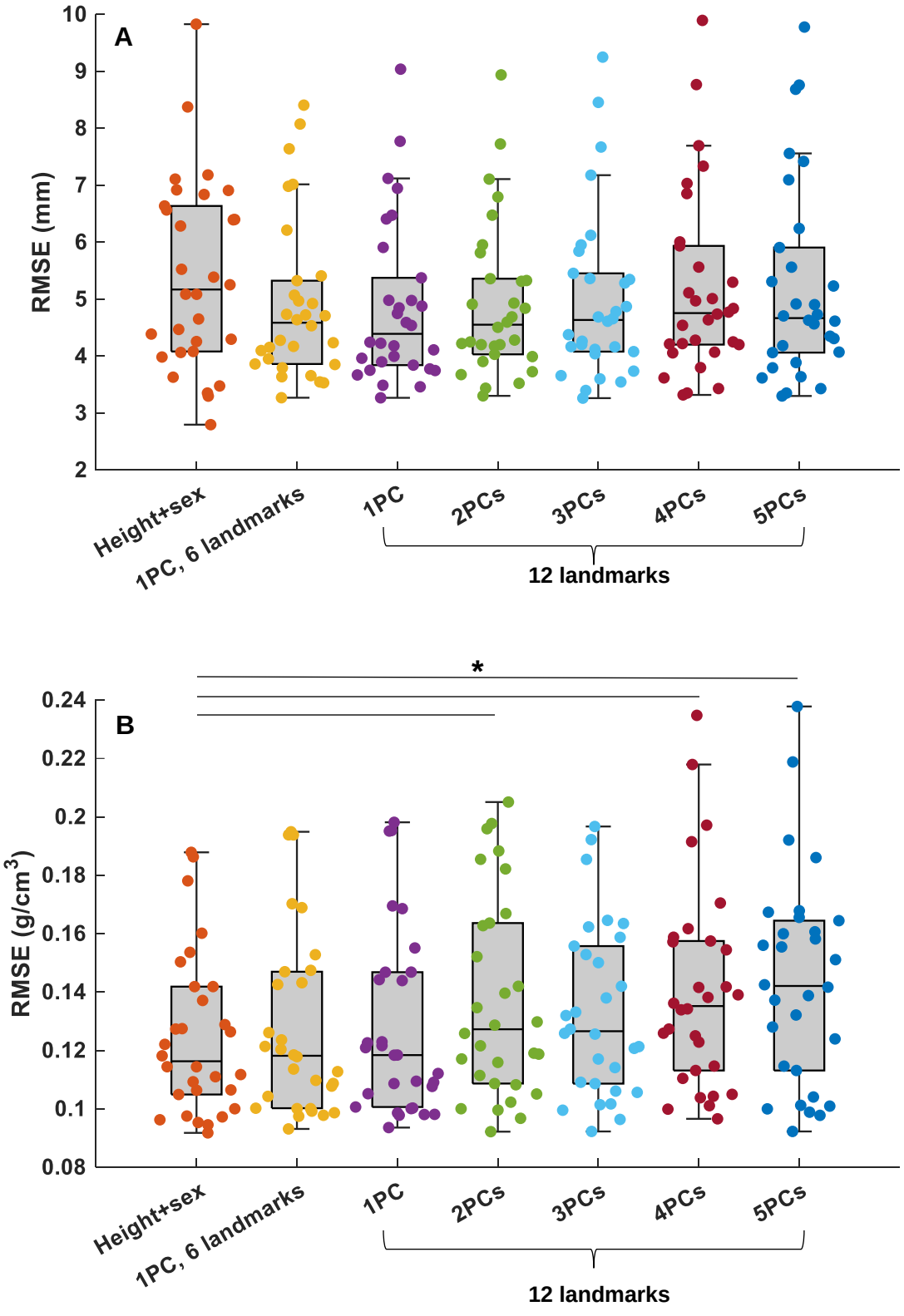


*Figure 6.2 Surface (A) and density (B) prediction errors resulting from different prediction methods. * indicates significant differences ($p < 0.003$).*

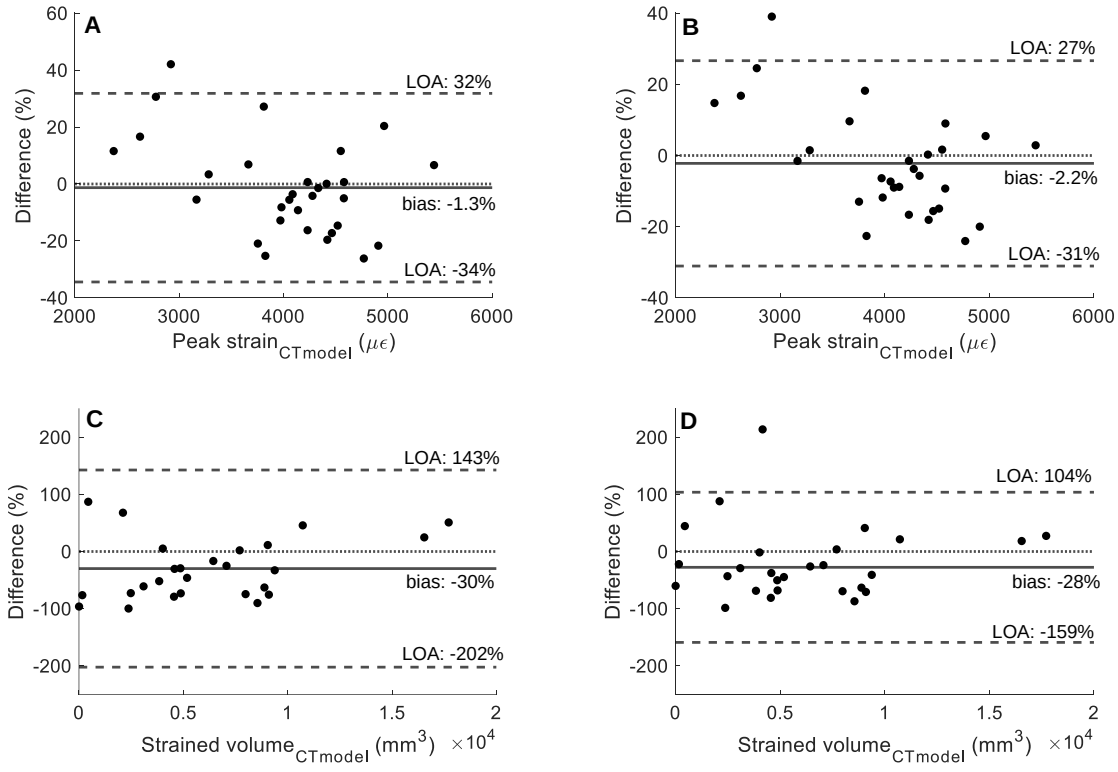


*Figure 6.3 Bland-Altman plots illustrating percent differences in peak strain between (A) landmark-based or (B) height and sex-based and participant-specific models. Percent differences in strained volume between (C) landmark-based or (D) height and sex-based and participant-specific models. Three statistical outliers are not shown in plots C (3946%, 4102%, and 23159%) and D (2376%, 3340%, and 23272%). The outliers were due to very small strained volume observed in the reference CT-based models.*

## 6.4 Discussion

The purpose of this study was to: (1) quantify errors associated with predicting tibia-fibula geometry and density distribution from anatomic landmarks and (2) quantify how those errors propagate to finite element-calculated bone strain. Participant-informed meshes generated from landmarks illustrated median geometry and density distribution errors of 4.39-4.75 mm and 0.118-0.142 g/cm$^3$, respectively. These meshes did not improve upon those generated from height and sex only. The observed geometry and density distribution errors resulted in large errors in strain

distribution, peak strain, and strained volume, indicating that neither method could adequately approximate CT-derived participant-specific data.

Geometry error did not improve when the number of cumulative PCs used to generate the participant-informed models from landmarks was increased. Landmark error was smaller in predictions using four and five cumulative PCs (medians = 5.68 mm and 5.64 mm, respectively) when compared to predictions using one and two cumulative PCs (medians = 6.18 mm and 6.19 mm, respectively, $p < 0.001$). These findings suggest the SAM was overfit to the landmarks due to uncertainties in soft-tissue offsets and marker placement. Nolte et al. (2020) observed similar results, where tibial geometry prediction errors from skin-mounted landmarks were not different or greater when the number of PCs used increased while improvements in prediction errors were observed when bone surface landmarks were used.

We performed post-hoc analyses to investigate the influence of sources of uncertainty on our results. The first analysis reconstructed tibia-fibula geometry and density distribution from the CT marker data with participant-specific offset vectors and magnitudes (Appendix D, section D2). A negligible reduction in geometry error was observed in predictions using five cumulative PCs (median RMSE = 3.71 mm) when compared to predictions from one and two PCs (median RMSEs = 3.75 and 3.73, respectively, $p \leq 0.005$). Reducing marker offset and placement uncertainty improved scaling accuracy (PC 1) but did not result in meaningful improvements in geometry characterization. The second post-hoc analysis compared predictions based on marker sets from motion capture and CT sessions to further investigate errors due to marker placement intra-rater variability (Appendix D, section D3). Median (IQR) marker placement error between days was 9.5 (4.4) mm. Median surface geometry RMSEs between days were 3.9-4.1 mm. Surface geometry RMSE relative to participant-specific meshes illustrated only moderate reliability between days

(Intra-class correlation coefficients = 0.45-0.64). Geometry errors associated with landmark-based prediction appear to be due to a combination of limited information provided by palpable landmarks, marker placement uncertainties, and soft tissue offset uncertainties.

Geometry and density distribution errors resulted in large finite element-calculated strain errors in the participant-informed models when compared to the participant-specific models. Median RMSEs were nearly 500 με for reconstructions from landmarks and from height and sex. Furthermore, the agreement range for strained volume far exceeded the acceptable limits, with differences up to ± 100-200% when compared to participant-specific models. Based on these results, participant-specific models generated from 3D medical imaging data are necessary when comparing finite element-calculated strain between individuals or groups. Using inaccurate participant-informed models generated from landmarks or height and sex as described in this analysis may lead to erroneous conclusions due to geometry errors influencing strain results. When geometry differs between groups but is not captured in the finite element mesh, differences in strain between groups could be over- or underestimated depending on the magnitude and direction of differences in applied loads between groups.

While participant-informed models should not be used to make comparisons between groups, they may still be useful to evaluate relative changes within individuals in response to interventions or conditions. Previous work observed strong agreement ($r^2$ = 0.96) in relative changes in strain resulting from neuromuscular fatigue during running between participant-informed and participant-specific models despite large absolute errors (Khassetarash et al. 2023). However, the analysis was limited to four participants. Further work with larger sample sizes and investigating possible geometry-applied load interactions is warranted to confirm whether

participant-informed models based on anthropometric or landmark data alone are adequate for within-participant comparisons.

Another limitation of this study was that we did not test the efficacy of incorporating a measure of density into the prediction algorithms. This study was focused on evaluating the accuracy of participant-informed meshes generated in the complete absence of medical imaging. Our previous work suggests that geometry varies to a greater degree and has a larger influence on bone strain than variations in density distribution in young active adults (Bruce, Baggaley, Khassetarash, et al. 2022). However, including a measure of bone density or cortical thickness from peripheral quantitative CT or high resolution peripheral quantitative CT scans, for example, would likely improve density distribution and strain predictions. Another approach worth investigating in future work is 2D to 3D reconstruction of the tibia and fibula from radiographs, which has shown excellent results for generating finite element models of the proximal femur (Väänänen et al. 2015; Grassi et al. 2017; Grassi et al. 2021).

### 6.5 Conclusions

In conclusion, skin-mounted landmarks were insufficient to accurately characterise tibial geometry and associated variations in density due to uncertainties in soft-tissue offsets and marker placement variability. Geometry and density distribution errors associated with generating models from landmarks or height and sex led to large errors in finite-element predicted bone strain. This approach for generating participant-informed finite element models should not be used when making comparisons between groups to avoid possible errors due to geometry variation. Some form of medical imaging is likely necessary to generate an accurate participant-informed model of the tibia and fibula.

# Chapter 7

# Discussion and Conclusions

## 7.1 Summary

The goal of this work was to develop a more nuanced understanding of the mechanical implications of tibial-fibular geometry and density variations present in young, active adults. To that end, I developed statistical shape and appearance models of the tibia and fibula to characterise how geometry and density distributions varied in this population. The statistical models were used in combination with biomechanical data and the finite element method to quantify the influence of these variations, sexual dimorphism, and landmark-based prediction errors on finite element-predicted bone strain. The four studies presented in this thesis identified key tibial features and sex-related differences influencing bone strain and highlight the necessity for medical imaging to accurately characterise participant-specific geometry and material properties.

The first and second studies in this thesis demonstrated that sex-related differences in bone geometry drive elevated bone strain and strained volume in the average female when compared to the average male. The first study illustrated a narrower tibia and greater cortical density in the average female. The greater cortical density reduced strain but was only able to partially offset the negative effects of the narrower tibial diaphysis. Encouragingly, the second study confirmed these findings in a separate cohort. While the sex-related differences in tibial geometry were subtle in

visual appearance, their large influence on strained volume (41-80% differences between the average male and female), considered together with data from mechanical testing and epidemiologic studies, indicate these differences are mechanically meaningful. The observed differences in strain confirm that bone geometry very likely contributes to the greater risk of stress fracture observed in females when compared to males.

The first study also identified key geometry and density distribution variations that had the greatest influence on bone strain. Again, geometry variations illustrated strong effects on bone strain. Sagittal plane curvature, with concomitant changes in diaphysis length and cortical thickness, and transverse diaphyseal geometry variations changed strained volume estimates by up to ± 95% and ± 66%, respectively. Transverse geometry included variations in both periosteal geometry and cortical thickness. These results highlight the importance of accurately characterizing participant-specific geometry and density when estimating and comparing strain between individuals or groups. Sagittal curvature and transverse geometry seem to be the most important features to accurately characterise, which informed the landmarks used in the final study.

Statistical shape and appearance models have been proposed as tools to generate estimates of individuals' bone geometries and density distributions in the absence of computed tomography (CT) imaging. This would improve access to and reduce the time and cost required for participant-specific musculoskeletal and finite element modeling approaches. The third study predicted tibial-fibular geometry from landmarks on the bone surface using a SSM with high accuracy. Unfortunately, the uncertainties introduced using skin-mounted landmarks in the final study increased errors in bone geometry. Furthermore, geometry and density errors from predictions using skin-mounted landmarks and the SAM developed in Chapter 3 resulted in very large errors in finite element-predicted bone strain (RMSE of 500 με and limits of agreement up to ±100-

200%). This indicates that some form of medical imaging, alone or in combination with landmarks, is necessary to adequately capture participant-specific bone geometry and material properties to avoid erroneous conclusions when evaluating comparisons between individuals or groups.

## 7.2 Tibial morphology and stress fracture risk

While the pathophysiology of stress fracture is not fully understood, it is believed to result from an imbalance between microdamage accumulation and microdamage repair (Hoenig et al. 2022). It is currently unknown if the accelerated accumulation of damage leading to fracture is due solely to increased loading or the combination of increased loading and a weakening of the tissue due to elevated remodeling in response to sudden increases in activity. Despite this uncertainty, bone strain plays a key role in the damage evolution of both pathways. Strained volume, i.e., the volume of bone experiencing high strain magnitudes, is also a strong predictor of fatigue life (Loundagin & Edwards 2020; Haider et al. 2021; Haider et al. 2022). Small changes in strain magnitude and/or strained volume are associated with much larger changes in the number of cycles a bone may withstand before failure. For example, in tests of whole rabbit tibiae under combined compression and torsional loads, decreasing strained volume by 41% was associated with a 2.7-fold increase in fatigue life (Haider et al. 2021). The differences in strained volume resulting from sexual dimorphism and geometry and density variations observed in this thesis (≥40%) indicate that variations in these parameters present in young active adults are likely meaningful risk factors for stress fracture.

The findings from Chapters 3 and 4 of this thesis strongly support the hypothesis that bone geometry, independent of allometric scaling, contributes to the disparity in stress fracture risk between females and males. Specifically, the average female illustrated a narrower tibia and thinner diaphyseal cortex when compared to the average male. The narrower tibial geometry

resulted in elevated strain and strained volume, explaining, in part, the greater risk of stress fracture observed in females. Although the difference in geometry through the tibial diaphysis was visually subtle, the consequent difference in strained volume indicates that the difference was mechanically meaningful. This conclusion is indirectly supported by evidence from *in vitro* and *ex vivo* testing (discussed above) and epidemiologic studies. Athletes and military recruits who experience stress fractures illustrate less robust tibial transverse cross-sectional geometry, adjusted for stature, when compared to controls (Beck et al. 2000; Popp et al. 2020; Koltun et al. 2022).

Typically, studies evaluating bone geometry and density as risk factors for stress fracture have measured only transverse cross-sectional parameters at discrete sites along the length of the tibia and/or simple measures of bone mineral density and bone mineral content (Beck et al. 2000; Koltun et al. 2022). These measures, obtained from dual-energy x-ray absorptiometry (DXA) and peripheral quantitative computed tomography (pQCT) scans, are more feasible for large cohort studies, but they lack important geometry variations that may influence stress fracture risk. In fact, the PC in the SAM that had the greatest influence on bone strain described variations in bone sagittal curvature (Chapter 3), which cannot be characterised using traditional DXA or pQCT. Greater sagittal curvature combined with a shorter diaphysis relative to tibial length and thinner cortex resulted in increased strained volume by up to 95%. The large increase in strained volume suggests that sagittal curvature may also be associated with stress fracture risk, but this has yet to be evaluated in epidemiologic studies.

### 7.3 Bone and body size

On average females have a smaller stature than males, although there is notable overlap between sexes (Figure 7.1) (Statistics Canada 2015a; Statistics Canada 2015b). The evidence for body size as a risk factor for stress fracture is mixed (Giladi et al. 1987; Winfield et al. 1997;

Välimäki et al. 2005; Shaffer et al. 2006; Knapik et al. 2012). On one hand, larger stature is associated with greater bone cross-sectional area and greater bone width (Sumnik et al. 2006). The first PC of the SAM developed in this thesis described allometric scaling and was strongly associated with height ($r^2$=0.82). While scaling was associated with a slight decrease in cortical thickness relative to diaphysis diameter, cortical area and bone diameter visibly increased with bone size (Appendix A, Figure A.1). As expected, when the applied loads were held constant increased bone size resulted in decreased strain. On the other hand, larger statures are also associated with greater muscle cross sectional area and joint moments (Sumnik et al. 2006; Unnikrishnan et al. 2021). These changes could increase strains and possibly completely offset changes due to allometric scaling. In fact, studies of young active females and males demonstrated that tibial strain was not affected by stature during unloaded running (Unnikrishnan et al. 2021; Tong et al. 2023).

Sex differences in joint contact and muscle forces during running are not well characterised, but forces applied to the tibia may not necessarily be larger in males when compared to females. Meardon et al. (2021) observed lower axial force and anterior-posterior bending moments but higher medial-lateral forces at the ankle joint in females when compared to males. Further work is needed to better characterise sex differences in loads applied to the tibia and their relationship with stature. The difference in stature between males and females may come into play in military populations where overstriding and differential adaptations to load carriage as a function of stature may increase strains by increasing the applied loads relative to body size in shorter individuals (Unnikrishnan et al. 2021; Hoenig et al. 2022). This may contribute to the greater disparity in stress fracture risk between sexes in military populations when compared to athletes (Kardouni et al. 2021; Hoenig et al. 2022).

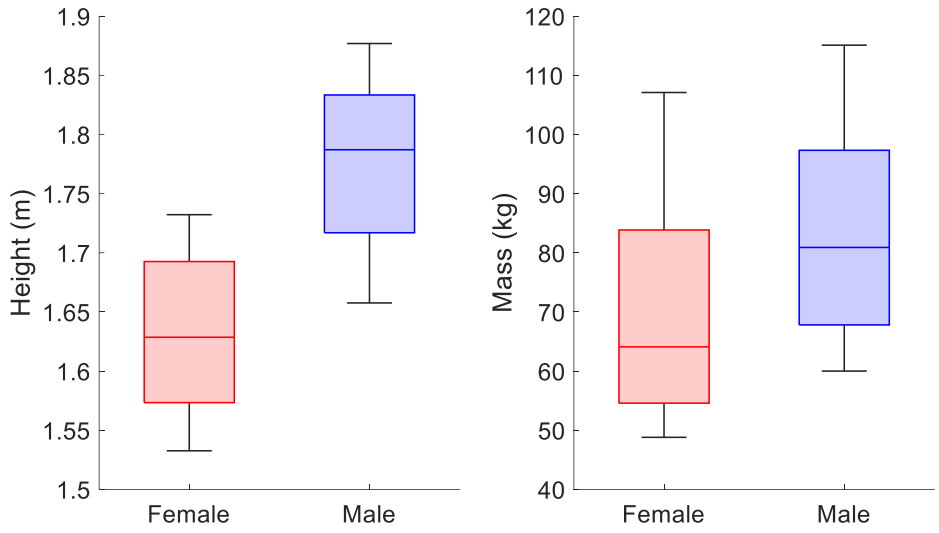


*Figure 7.1 Height (A) and mass (B) of Canadians aged 20-39 years. Whiskers represent the 5th and 95th percentiles. Data from:* (Statistics Canada 2015a; Statistics Canada 2015b)

Another factor that needs to be considered with respect to allometric scaling is the change in bone volume. When loads were kept constant, including allometric scaling in the average male and female models exacerbated the observed differences in both peak strain and strained volume. Theoretically, if loads were scaled one-to-one with bone size, peak strain and strain distribution across the bone may not change, but strained volume would. In this case, including the small-scale difference between the average female and male models (8%) diminishes, but does not eliminate, the difference in strained volume. Clearly, the question of how allometric scaling may affect bone strain, strained volume, and stress fracture risk depends on how applied loads scale with bone, body, and/or muscle size and any sex differences in those factors. As discussed in the previous paragraph, sex differences in joint kinetics are not well characterised and may not necessarily be larger in males. Further work is needed to address the many open questions in this area.

## 7.4 Towards predicting stress fractures

The etiology of stress fracture is multifactorial and not fully understood. As a result, it has been difficult to develop effective screening tools. There are many risk factors associated with stress fracture including: RED-S, exercise history, stage of training, kinematic parameters, nutritional deficiencies, and sex (Hoenig et al. 2022). These factors all influence the mechanical strain environment of the tibia. Thus, individualized finite element modeling approaches, which estimate bone strain, could play a role in screening and monitoring tools or the development thereof. For example, finite element-predicted strain may be used in combination with probabilistic modeling approaches to estimate fracture risk (Taylor et al. 2004; Firminger et al. 2017). In fact, a Weibull analysis accounting for both strain magnitude and strained volume was recently shown to provide accurate predictions of whole-bone fatigue life *in vitro* (Haider et al. 2022).

Individualized finite element modeling is currently costly, time consuming, and requires access to a clinical CT scanner. If modeling were to be used for risk assessment, generation of these models needs to be more accessible and automated. However, as demonstrated in this thesis it is crucial that streamlined methods to generate finite element models preserve accurate characterization of individuals' bone geometry and density. Unfortunately, skin-mounted landmarks were shown to be insufficient for this purpose (Chapter 6), indicating that medical imaging is necessary. Moving forward, approaches to characterise geometry and density distribution from less intensive imaging modalities than clinical CT could be explored. For example, 2D to 3D reconstruction algorithms using SAMs and DXA scans have been used to accurately characterise geometry and density distributions and predict fracture strength of the proximal femur (Väänänen et al. 2015; Grassi et al. 2017; Grassi et al. 2021). Alternatively, data from EOS (Illés & Somoskeöy 2012) or free-hand ultrasound techniques (Krysztoforski et al.

2011), or transverse cross-sections obtained at a handful of locations along the length of the tibia-fibula complex using pQCT or high resolution pQCT (HR-pQCT) might provide enough information to estimate whole-bone geometry and density distributions with reasonable accuracy, although this has yet to be tested.

In addition to bone geometry and density, HR-pQCT enables quantification of microarchitecture and micro-FE estimated bone strength, some of which may be associated with stress fracture risk (Schnackenburg et al. 2011; Schanda et al. 2019). If the pathophysiology of stress fracture involves a combination of mechanical fatigue and biological processes, where elevated remodeling following sudden increases in training volume accelerates microdamage accumulation, an increase in porosity could perhaps be captured with HR-pQCT. With a minimum isotropic voxel size of 61 μm (Manske et al. 2015), second-generation HR-pQCT scanners would be able to capture resorption canals (200 – 300 μm) (Cooper et al. 2016; Lassen et al. 2017). While this resolution would miss small pores, large pores have demonstrated a disproportionally large effect on fatigue life in material-level tests ( Loundagin & Edwards 2020; Loundagin et al. 2021). Measures of porosity could be combined with FE-estimated strained volume in a modified Weibull analysis to potentially improve predictions of fracture probability.

## 7.5 Towards preventing stress fractures

As previously discussed, stress fractures typically occur in the weeks following sudden, rapid increases in training loads and volume (Rizzone et al. 2017; Kardouni et al. 2021; Hoenig et al. 2022). Increased loading and associated remodeling may result in elevated bone strain and rates of microdamage accumulation (Hoenig et al. 2022). On the other hand, bone strain, or some consequence thereof, is also the key factor driving adaptation (Klein-Nulend et al. 2013). Stress fractures are thought to occur when microdamage accumulation outpaces the bone's ability to

repair and adapt (Hoenig et al. 2022). Management of training loads and volume to reduce imbalances between damage and repair should reduce stress fracture incidence, but training programs need to be personalized. As demonstrated in this thesis, individuals subjected to the same applied loads can have substantially different peak strains and strained volume due to bone geometry and density distribution variations. Characterizing geometry and density distribution in addition to loading patterns, and understanding how these factors influence bone strain, could improve stress fracture risk estimates (discussed in the previous section, 7.4) and guide the optimization of training programs. However, geometry and density characterization requires medical imaging, limiting the feasibility of personalized modeling across large populations or groups. Optimizing training loads is likely most important for those who are at high risk of fracture and may have less room for training errors. Therefore, efforts to optimize training should be focused on individuals at high risk of fracture identified through risk factor-based screening. In some populations such as elite runners and military recruits, obtaining simple measures of bone geometry and density with DXA, EOS, or pQCT as part of initial risk factor screening procedures may be beneficial to identify athletes/recruits for follow-up personalized modeling.

When gradual increases in training loads are not possible or in groups at heightened risk (e.g., individuals with narrower and/or curved tibiae and individuals with a history of stress fracture) strategies to reduce bone strain may be effective to mitigate stress fracture risk. Probabilistic modeling using loads representative of running suggest for every 10% increase in strain magnitude, the number of cycles the bone can withstand before fracture is halved (Edwards 2018). Of the interventions investigated in the literature, increasing running cadence is a promising strategy. Increased cadence, and concomitant decreased stride length, is associated with decreased joint loads, bone strain, and modeled risk of stress fracture (Edwards et al. 2009; Luedeke et al.

2016; Kliethermes et al. 2021). Cadence manipulation is easily implemented, and continuous monitoring is commercially available with wearable sensors.

Strategies to increase the tibia's loading capacity by improving bone geometry, density, and/or quality may also be effective. History of participation in activities involving impulsive multi-directional loading such as jumping and change of direction movements is associated with reduced stress fracture risk (Milgrom et al. 2000). Ideally, participation in these activities would begin before puberty, when loading encourages the development of greater bone size relative to body size through bone modeling (Allen & Burr 2019). Still, some gains in bone mass, geometry, and microstructure quality can be achieved after skeletal maturity is reached (Bhatia et al. 2015; Hughes et al. 2018). Significant improvements in a variety of parameters such as trabecular and cortical volumetric bone mineral density, trabecular thickness and cortical thickness have been observed in as little as eight weeks of intense training (O'Leary et al. 2022; Hughes et al. 2023). Thus, athletes and military recruits with bone geometry and/or density risk factors may benefit from an off-season or lead-in program aimed at improving bone mass and reducing the increase in training volume when the season or basic training begins.

## 7.6 Limitations and future work

An assumption underpinning my interpretations of whether the geometry and density distribution differences observed in this thesis are meaningful is that finite element-predicted bone strain is predictive of stress fracture risk. This assumption is based on the central role of bone strain in the hypothesized pathophysiology of stress fracture, supported by fatigue tests and associations observed in prospective epidemiologic studies. However, large prospective studies would be needed to confirm that finite element-predicted bone strain and strained volume are indeed predictive of stress fracture in a sport or military setting. Ideally, baseline CT scans including both

tibiae and fibulae with a phantom, and gait data, perhaps at multiple speeds, would be obtained prior to the start of a training season or the beginning of basic military training. This data would be used to generate personalized finite element models to predict peak strain, strained volume, and probability of fracture. Participants would be followed over time for stress fracture incidence and tracking activity. Probability of fracture could then be compared to clinical incidence to evaluate whether finite element-predicted bone strain is a useful predictive measure for stress fracture risk. Given the time, cost, advanced medical imaging, and expertise required to generate hundreds of personalized finite element models, a large prospective study like this is currently infeasible. That said, recent advances in automated image segmentation and generation of personalized models have addressed some of these limitations (Deng et al. 2022). Eventually, we will be able to test the validity of finite element-predicted bone strain as a surrogate for stress fracture risk.

Assuming finite element-predicted bone strain is indeed predictive of stress fracture risk, future work developing methods to accurately predict whole-bone geometry and density from more accessible imaging methods is warranted to improve the clinical applicability of finite element modelling. The use of SAMs in combination with DXA at the proximal femur was discussed in section 7.4. The next steps would be to validate this approach in the tibia and fibula and test the sensitivity of predictions to positioning variability and scanner. Other imaging modalities including free-hand ultrasound, pQCT, and HR-pQCT may also be explored. In the cohort of thirty participants analyzed in Chapters 4 and 6, I collected HR-pQCT scans at the distal tibia in addition to clinical CT and gait data. I plan to evaluate whether relationships between bone quality measures and PC scores exist and whether the geometry and density data provided by the scan improves predictions of whole-tibia geometry and density when combined with height and sex data.

The strain environment of bone is determined by the bone's geometry, density distribution, material properties, and the applied loads. This thesis deliberately focused on bone geometry and density distribution, isolating and parametrically evaluating variations in these two factors and their contributions to bone strain. However, applied loads and muscle attachment areas, which can affect muscle moment arms, may differ between sexes (Meardon et al. 2021; Kimata et al. 2022). It is unknown whether these differences would be sufficient to produce meaningful changes in strain or how applied loads interact with geometry and density distribution variations. Future work will systematically test the sensitivity of bone strain to applied loads and explore potential applied load-bone morphology interactions. Another study will quantify sex- and stature/mass-related differences in the applied loads and whether differences in bone strain between females and males still exist when sex-specific loads are applied.

Finally, there are some limitations to the generalizability of the SSM and SAM developed in this thesis. The models were trained using data from physically active adults aged 18-32 years. This is the most common population studied in sports biomechanics, and is a relevant age range for runners, athletes, and military recruits who experience stress fractures. However, the models may not be generalizable to older populations. This was demonstrated in Chapter 5, where the SSM underestimated transverse tibial size in elderly individuals. On the other end of the spectrum, these models trained on adults may also not generalize to children and adolescents less than 1.45 m tall (Davico et al. 2020). In addition, the SSM and SAM may not generalize well to some clinical populations. For example, the SAM may overestimate intracortical bone mineral density if applied to athletes with RED-S. Future work could expand the model to include these athletes and evaluate the contribution of low bone mineral density to differences in predicted bone strain when compared to healthy athletes.

## 7.7 Conclusions

Bone geometry and density are hypothesized risk factors for stress fracture and may contribute to the disparity in stress fracture risk between sexes. Previous studies were limited to two-dimensional transverse measures of geometry and density or three-dimensional analyses of periosteal geometry only. By leveraging statistical approaches in combination with the finite element method, this work is the first to characterize and quantify the mechanical implications of covariations in whole-bone tibial-fibular geometry and density distribution. Transverse diaphyseal geometry and sagittal curvature were identified as key features that likely influence stress fracture risk, demonstrating large effects on finite element-predicted bone strain. Most importantly, this work demonstrated and confirmed that sex-related differences in bone geometry meaningfully impact bone strain and likely explain, in part, the elevated risk of stress fracture observed in females when compared to males.

As we work towards improving predictive models and developing effective screening tools for stress fracture risk, this work provides insights into the role of bone geometry and density distribution and the key features that will need to be accurately characterised. Unfortunately, landmark- and anthropometric-based predictions were not sufficiently accurate to characterise geometry and density, leading to substantial errors in bone strain estimates when compared to participant-specific models generated from CT data. There are promising approaches that may enable accurate estimation of bone geometry and density from less intensive imaging modalities, but it is clear that some level of advanced medical imaging data will be necessary to generate personalized models or characterise geometry and density features associated with stress fracture risk.

# References


Allen MR, Burr DB. 2019. Bone Growth, Modeling, and Remodeling. In: Basic Appl Bone Biol. London: Elsevier; p. 85–100.

Ambellan F, Tack A, Ehlke M, Zachow S. 2019. Automated segmentation of knee bone and cartilage combining statistical shape knowledge and convolutional neural networks: Data from the Osteoarthritis Initiative. Med Image Anal. 52:109–118.

Arnold EM, Ward SR, Lieber RL, Delp SL. 2010. A Model of the Lower Limb for Analysis of Human Movement. Ann Biomed Eng. 38(2):269–279.

Audenaert EA, Pattyn C, Steenackers G, De Roeck J, Vandermeulen D, Claes P. 2019. Statistical Shape Modeling of Skeletal Anatomy for Sex Discrimination: Their Training Size, Sexual Dimorphism, and Asymmetry. Front Bioeng Biotechnol. 7:1–11.

Austman RL, Milner JS, Holdsworth DW, Dunning CE. 2008. The effect of the density–modulus relationship selected to apply material properties in a finite element model of long bone. J Biomech. 41(15):3171–3176.

Bah MT, Shi J, Browne M, Suchier Y, Lefebvre F, Young P, King L, Dunlop DG, Heller MO. 2015. Exploring inter-subject anatomic variability using a population of patient-specific femurs and a statistical shape and intensity model. Med Eng Phys. 37(10):995–1007.

Bahl JS, Zhang J, Killen BA, Taylor M, Solomon LB, Arnold JB, Lloyd DG, Besier TF, Thewlis D. 2019. Statistical shape modelling versus linear scaling: Effects on predictions of hip joint centre location and muscle moment arms in people with hip osteoarthritis. J Biomech. 85:164–172.

Ballock RT, O'Keefe RJ. 2003. The biology of the growth plate. J Bone Joint Surg Am. 85(4):715–26.

Bass SL, Saxon L, Daly RM, Turner CH, Robling AG, Seeman E, Stuckey S. 2002. The Effect of Mechanical Loading on the Size and Shape of Bone in Pre-, Peri-, and Postpubertal Girls: A Study in Tennis Players. J Bone Miner Res. 17(12):2274–2280.

Beck TJ, Ruff CB, Shaffer RA, Betsinger K, Trone DW, Brodine SK. 2000. Stress fracture in military recruits: Gender differences in muscle and bone susceptibility factors. Bone. 27(3):437–444.

Bellido T, Plotkin LI, Bruzzaniti A. 2019. Bone Cells. In: Basic Appl Bone Biol. London: Elsevier; p. 37–55.

Bennell K, Matheson G, Meeuwisse W, Brukner P. 1999. Risk Factors for Stress Fractures. Sport Med. 28(2):91–122.

Bennell KL. 1996. Models for the pathogenesis of stress fractures in athletes. Br J Sports Med. 30(3):200–204.

Bennell KL, Brukner PD. 1997. Epidemiology and site specificity of stress fractures. Clin Sports Med. 16(2):179–196.

Bennell KL, Malcolm SA, Thomas SA, Wark JD, Brukner PD. 1996. The Incidence and Distribution of Stress Fractures in Competitive Track and Field Athletes. Am J Sports Med. 24(2):211–217.

Bertram JEA, Biewener AA. 1988. Bone curvature: Sacrificing strength for load predictability? J Theor Biol. 131(1):75–92.

Bhatia VA, Brent Edwards W, Johnson JE, Troy KL. 2015. Short-Term Bone Formation is Greatest Within High Strain Regions of the Human Distal Radius: A Prospective Pilot Study. J Biomech Eng. 137(1):011001.

Bigley RF, Gibeling JC, Stover SM, Hazelwood SJ, Fyhrie DP, Martin RB. 2007. Volume effects on fatigue life of equine cortical bone. J Biomech. 40(16):3548–3554.

Bonaretti S, Seiler C, Boichon C, Reyes M, Büchler P. 2014. Image-based vs. mesh-based statistical appearance models of the human femur: Implications for finite element simulations. Med Eng Phys. 36(12):1626–1635.

Bro R, Smilde AK. 2014. Principal component analysis. Anal Methods. 6(9):2812–2831.

Bruce OL, Baggaley M, Khassetarash A, Haider IT, Edwards WB. 2022. Tibial-fibular geometry and density variations associated with elevated bone strain and sex disparities in young active adults. Bone. 161:116443.

Bruce OL, Baggaley M, Welte L, Rainbow MJ, Edwards WB. 2022. A statistical shape model of the tibia-fibula complex: sexual dimorphism and effects of age on reconstruction accuracy from anatomical landmarks. Comput Methods Biomech Biomed Engin. 25(8):875–886.

Brukner PD, Bennell KL. 1995. Stress fractures in runners.Wilder RP, O'Connor F, editors. J Back Musculoskelet Rehabil. 5(4):341–351.

Bryan R, Nair PB, Taylor M. 2012. Influence of femur size and morphology on load transfer in the resurfaced femoral head: A large scale, multi-subject finite element study. J Biomech. 45(11):1952–1958.

Brzobohatá H, Krajíček V, Horák Z, Velemínská J. 2015. Sex classification using the three-dimensional tibia form or shape including population specificity approach. J Forensic Sci. 60(1):29–40.

Brzobohatá H, Krajíèek V, Horák Z, Velemínská J. 2016. Sexual dimorphism of the human tibia through time: Insights into shape variation using a surface-based approach. PLoS One. 11(11):1–21.

Bulathsinhala L, Hughes JM, McKinnon CJ, Kardouni JR, Guerriere KI, Popp KL, Matheny RW, Bouxsein ML. 2017. Risk of Stress Fracture Varies by Race/Ethnic Origin in a Cohort Study of 1.3 Million US Army Soldiers. J Bone Miner Res. 32(7):1546–1553.

Burr D, Milgrom C, Boyd R, Higgins W, Robin G, Radin E. 1990. Experimental stress fractures of the tibia. Biological and mechanical aetiology in rabbits. J Bone Joint Surg Br. 72-B(3):370–375.

Burr DB. 2019. Bone Morphology and Organization. In: Basic Appl Bone Biol. London: Elsevier;

p. 3–26.

Burr DB, Forwood MR, Fyhrie DP, Martin RB, Schaffler MB, Turner CH. 1997. Bone Microdamage and Skeletal Fragility in Osteoporotic and Stress Fractures. J Bone Miner Res. 12(1):6–15.

Burr DB, Milgrom IC, Fyhrie D, Forwood M, Nyska M, Finestone A, Hoshaw S, Saiag E, Simkin A. 1996. In Vivo Measurement of Human Tibial Strains During Vigorous Activity. Bone. 18(5):405–415.

Burton WS, Sintini I, Chavarria JM, Brownhill JR, Laz PJ. 2019. Assessment of scapular morphology and bone quality with statistical models. Comput Methods Biomech Biomed Engin. 22(4):341–351.

Campbell JQ, Petrella AJ. 2016. Automated finite element modeling of the lumbar spine: Using a statistical shape model to generate a virtual population of models. J Biomech. 49(13):2593–2599.

Carbone V, van der Krogt MM, Koopman HFJM, Verdonschot N. 2012. Sensitivity of subject-specific models to errors in musculo-skeletal geometry. J Biomech. 45(14):2476–2480.

Carter DR, Caler WE, Spengler DM, Frankel VH. 1981a. Fatigue Behavior of Adult Cortical Bone: The Influence of Mean Strain and Strain Range. Acta Orthop Scand. 52(5):481–490.

Carter DR, Caler WE, Spengler DM, Frankel VH. 1981b. Uniaxial fatigue of human cortical bone. The influence of tissue physical characteristics. J Biomech. 14(7):461–470.

Cates J, Elhabian S, Whitaker R. 2017. ShapeWorks. In: Stat Shape Deform Anal. Elsevier; p. 257–298.

Chalmers J, Ray RD. 1962. The growth of transplanted foetal bones in different immunocological environments. J Bone Joint Surg Br. 44-B(1):149–164.

Chandran V, Maquer G, Gerig T, Zysset P, Reyes M. 2019. Supervised learning for bone shape and cortical thickness estimation from CT images for finite element analysis. Med Image Anal. 52:42–55.

Changstrom BG, Brou L, Khodaee M, Braund C, Comstock RD. 2015. Epidemiology of Stress Fracture Injuries Among US High School Athletes, 2005-2006 Through 2012-2013. Am J Sports Med. 43(1):26–33.

Chen TL, An WW, Chan ZYS, Au IPH, Zhang ZH, Cheung RTH. 2016. Immediate effects of modified landing pattern on a probabilistic tibial stress fracture model in runners. Clin Biomech. 33:49–54.

Clouthier AL, Borschneck D, Smith CR, Vignos MF, Thelen DG, Deluzio KJ, Rainbow MJ. 2022. Influence of Articular Geometry and Tibial Tubercle Location on Patellofemoral Kinematics and Contact Mechanics. J Appl Biomech. 38(1):58–66.

Clouthier AL, Smith CR, Vignos MF, Thelen DG, Deluzio KJ, Rainbow MJ. 2019. The effect of articular geometry features identified using statistical shape modelling on knee biomechanics. Med Eng Phys. 66:47–55.

Cooper DML, Kawalilak CE, Harrison K, Johnston BD, Johnston JD. 2016. Cortical Bone Porosity: What Is It, Why Is It Important, and How Can We Detect It? Curr Osteoporos Rep. 14(5):187–198.

Cootes TF, Taylor CJ. 2004. Statistical Models of Appearance for Computer Vision. https://personalpages.manchester.ac.uk/staff/timothy.f.cootes/models/app_models.pdf

Cosman F, Ruffing J, Zion M, Uhorchak J, Ralston S, Tendy S, McGuigan FEA, Lindsay R, Nieves J. 2013. Determinants of stress fracture risk in United States Military Academy cadets. Bone. 55(2):359–366.

Della Croce U, Cappozzo A, Kerrigan DC. 1999. Pelvis and lower limb anatomical landmark calibration precision and its propagation to bone geometry and joint angles. Med Biol Eng Comput. 37(2):155–161.

Dalstra M, Huiskes R, Odgaard A, van Erning L. 1993. Mechanical and textural properties of pelvic trabecular bone. J Biomech. 26(4–5):523–535.

Davico G, Pizzolato C, Killen BA, Barzan M, Suwarganda EK, Lloyd DG, Carty CP. 2020. Best methods and data to reconstruct paediatric lower limb bones for musculoskeletal modelling. Biomech Model Mechanobiol. 19(4):1225–1238.

Day GA, Jones AC, Wilcox RK. 2022. Using Statistical Shape and Appearance Modelling to characterise the 3D shape and material properties of human lumbar vertebrae: A proof of concept study. J Mech Behav Biomed Mater. 126:105047.

Delp SL, Loan JP, Hoy MG, Zajac FE, Topp EL, Rosen JM. 1990. An interactive graphics-based model of the lower extremity to study orthopaedic surgical procedures. IEEE Trans Biomed Eng. 37(8):757–767.

Deng Y, Wang L, Zhao C, Tang S, Cheng X, Deng H-W, Zhou W. 2022. A deep learning-based approach to automatic proximal femur segmentation in quantitative CT images. Med Biol Eng Comput. 60(5):1417–1429.

Ding Z, Tsang CK, Nolte D, Kedgley AE, Bull AMJ. 2019. Improving Musculoskeletal Model Scaling Using an Anatomical Atlas: The Importance of Gender and Anthropometric Similarity to Quantify Joint Reaction Forces. IEEE Trans Biomed Eng. 66(12):3444–3456.

Doblaré M, García JM, Gómez MJ. 2004. Modelling bone tissue fracture and healing: a review. Eng Fract Mech. 71(13–14):1809–1840.

Dong C. Liu, Jorge Nocedal. 1989. On the limited memory BFGS method for large scale optimization. Math Program. 45:503–528.

Du S, Zheng N, Ying S, Liu J. 2010. Affine iterative closest point algorithm for point set registration. Pattern Recognit Lett. 31(9):791–799.

Edama M, Onishi H, Kubo M, Takabayashi T, Yokoyama E, Inai T, Watanabe H, Nashimoto S, Koga Y, Kageyama I. 2017. Gender differences of muscle and crural fascia origins in relation to the occurrence of medial tibial stress syndrome. Scand J Med Sci Sports. 27(2):203–208.

Edwards WB. 2018. Modeling Overuse Injuries in Sport as a Mechanical Fatigue Phenomenon.

Exerc Sport Sci Rev. 46(4):224–231.

Edwards WB, Schnitzer TJ, Troy KL. 2013. Torsional stiffness and strength of the proximal tibia are better predicted by finite element models than DXA or QCT. J Biomech. 46(10):1655–1662.

Edwards WB, Simonian N, Troy KL, Schnitzer TJ. 2015. Reduction in Torsional Stiffness and Strength at the Proximal Tibia as a Function of Time since Spinal Cord Injury. J Bone Miner Res. 30(8):1422–1430.

Edwards WB, Taylor D, Rudolphi TJ, Gillette JC, Derrick TR. 2009. Effects of Stride Length and Running Mileage on a Probabilistic Stress Fracture Model. Med Sci Sport Exerc. 41(12):2177–2184.

Edwards WB, Taylor D, Rudolphi TJ, Gillette JC, Derrick TR. 2010. Effects of running speed on a probabilistic stress fracture model. Clin Biomech. 25(4):372–377.

Ekenman I, Halvorsen K, Westblad P, Fellãnder-Tsai L, Rolf C. 1998. Local Bone Deformation at Two Predominant Sites for Stress Fractures of the Tibia: An In Vivo Study. Foot Ankle Int. 19(7):479–484.

Ekenman I, Milgrom C, Finestone A, Begin M, Olin C, Arndt T, Burr D. 2002. The role of biomechanical shoe orthoses in tibial stress fracture prevention. Am J Sports Med. 30(6):866–870.

Evans RK, Negus C, Antczak AJ, Yanovich R, Israeli E, Moran DS. 2008. Sex differences in parameters of bone strength in new recruits: beyond bone density. Med Sci Sports Exerc. 40(11 Suppl).

Fehling PC, Alekel L, Clasey J, Rector A, Stillman RJ. 1995. A comparison of bone mineral densities among female athletes in impact loading and active loading sports. Bone. 17(3):205–210.

Feldman S, Capozza RF, Mortarino PA, Reina PS, Ferretti JL, Rittweger J, Cointry GR. 2012. Site and sex effects on tibia structure in distance runners and untrained people. Med Sci Sports Exerc. 44(8):1580–1588.

Firminger CR, Fung A, Loundagin LL, Edwards WB. 2017. Effects of footwear and stride length on metatarsal strains and failure in running. Clin Biomech. 49:8–15.

Fredericson M, Bergman AG, Hoffman KL, Dillingham MS. 1995. Tibial Stress Reaction in Runners. Am J Sports Med. 23(4):472–481.

Fuchs RK, Allen MR, Ruppel ME, Diab T, Phipps RJ, Miller LM, Burr DB. 2008. In situ examination of the time-course for secondary mineralization of Haversian bone using synchrotron Fourier transform infrared microspectroscopy. Matrix Biol. 27(1):34–41.

Fyhrie DP, Milgrom C, Hoshaw SJ, Simkin A, Dar S, Drumb D, Burr DB. 1998. Effect of fatiguing exercise on longitudinal bone strain as related to stress fracture in humans. Ann Biomed Eng. 26(4):660–665.

Galloway F, Kahnt M, Ramm H, Worsley P, Zachow S, Nair P, Taylor M. 2013. A large scale finite element study of a cementless osseointegrated tibial tray. J Biomech. 46(11):1900–1906.

Gerus P, Sartori M, Besier TF, Fregly BJ, Delp SL, Banks SA, Pandy MG, D'Lima DD, Lloyd

DG. 2013. Subject-specific knee joint geometry improves predictions of medial tibiofemoral contact forces. J Biomech. 46(16):2778–2786.

Giladi M, Milgrom C, Simkin A, Stein M, Kashtan H, Margulies J, Rand N, Chisin R, Steinberg R, Aharonson Z, et al. 1987. Stress fractures and tibial bone width. A risk factor. J Bone Joint Surg Br. 69-B(2):326–329.

Gmachowska AM, Żabicka M, Pacho R, Pacho S, Majek A, Feldman B. 2018. Tibial stress injuries – location, severity, and classification in magnetic resonance imaging examination. Polish J Radiol. 83:471–481.

Grant TM, Diamond LE, Pizzolato C, Killen BA, Devaprakash D, Kelly L, Maharaj JN, Saxby DJ. 2020. Development and validation of statistical shape models of the primary functional bone segments of the foot. PeerJ. 2020(2):1–19.

Grassi L, Fleps I, Sahlstedt H, Väänänen SP, Ferguson SJ, Isaksson H, Helgason B. 2021. Validation of 3D finite element models from simulated DXA images for biofidelic simulations of sideways fall impact to the hip. Bone. 142(October 2020):115678.

Grassi L, Väänänen SP, Ristinmaa M, Jurvelin JS, Isaksson H. 2017. Prediction of femoral strength using 3D finite element models reconstructed from DXA images: validation against experiments. Biomech Model Mechanobiol. 16(3):989–1000.

Gray HA, Taddei F, Zavatsky AB, Cristofolini L, Gill HS. 2008. Experimental validation of a finite element model of a human cadaveric tibia. J Biomech Eng. 130(3):1–9.

Hadid A, Epstein Y, Shabshin N, Gefen A. 2018. Biomechanical Model for Stress Fracture-related Factors in Athletes and Soldiers. Med Sci Sports Exerc. 50(9):1827–1836.

Haider IT, Baggaley M, Brent Edwards W. 2020. Subject-Specific Finite Element Models of the Tibia with Realistic Boundary Conditions Predict Bending Deformations Consistent with in Vivo Measurement. J Biomech Eng. 142(2):1–10.

Haider IT, Lee M, Page R, Smith D, Edwards WB. 2021. Mechanical fatigue of whole rabbit-tibiae under combined compression-torsional loading is better explained by strained volume than peak strain magnitude. J Biomech. 122:110434.

Haider IT, Pohl AJ, Edwards WB. 2022. The probability of whole-bone fatigue fracture can be accurately predicted using specimen-specific finite element analysis incorporating a stochastic failure model. J Biomech. 143:111273.

Hall BK. 2015. Growth and Morphogenesis of Long bones. In: Bones Cartil Dev Evol Skelet Biol. Elsevier Science & Technology.

Hame SL, LaFemina JM, McAllister DR, Schaadt GW, Dorey FJ. 2004. Fractures in the Collegiate Athlete. Am J Sports Med. 32(2):446–451.

Harris SE, Gluhak-Heinrich J, Harris MA, Yang W, Bonewald LF, Riha D, Rowe PSN, Robling AG, Turner CH, Feng JQ, et al. 2007. DMP1 and MEPE expression are elevated in osteocytes after mechanical loading in vivo: theoretical role in controlling mineral quality in the perilacunar matrix. J Musculoskelet Neuronal Interact. 7(4):313–5.

Herman BC, Cardoso L, Majeska RJ, Jepsen KJ, Schaffler M. 2010. Activation of bone remodeling after fatigue: Differential response to linear microcracks and diffuse damage. Bone. 47(4):766–772.

Hoenig T, Ackerman KE, Beck BR, Bouxsein ML, Burr DB, Hollander K, Popp KL, Rolvien T, Tenforde AS, Warden SJ. 2022. Bone stress injuries. Nat Rev Dis Prim. 8(1):26.

Hughes JM, Dickin DC, Wang H. 2019. The relationships between multiaxial loading history and tibial strains during load carriage. J Sci Med Sport. 22(1):48–53.

Hughes JM, Gaffney-Stomberg E, Guerriere KI, Taylor KM, Popp KL, Xu C, Unnikrishnan G, Staab JS, Matheny RW, McClung JP, et al. 2018. Changes in tibial bone microarchitecture in female recruits in response to 8 weeks of U.S. Army Basic Combat Training. Bone. 113:9–16.

Hughes JM, Taylor KM, Guerriere KI, Smith NI, Staab JS, Walker LA, Staab JE, Bartlett PM, Spiering BA, Nguyen VT, et al. 2023. Changes in Distal Tibial Microarchitecture During Eight Weeks of U.S. Army Basic Combat Training Differ by Sex and Race. JBMR Plus. 7(4):e10719.

Hutchinson L, Schwartz JB, Morton AM, Davis IS, Deluzio KJ, Rainbow MJ. 2018. Operator Bias Errors Are Reduced Using Standing Marker Alignment Device for Repeated Visit Studies. J Biomech Eng. 140(4):1–7.

Illés T, Somoskeöy S. 2012. The EOS$^{TM}$ imaging system and its uses in daily orthopaedic practice. Int Orthop. 36(7):1325–1331.

Jee WSS. 2001. Integrated bone tissue physiology: Anatomy and physiology. In: Bone Mech Handbook, Second Ed. CRC Press.

Kardouni JR, McKinnon CJ, Taylor KM, Hughes JM. 2021. Timing of Stress Fractures in Soldiers During the First 6 Career Months: A Retrospective Cohort Study. J Athl Train. 56(12):1278–1284.

Keast M, Bonacci J, Fox A. 2023. Geometric variation of the human tibia-fibula: a public dataset of tibia-fibula surface meshes and statistical shape model. PeerJ. 11:e14708.

Keyak JH, Meagher JM, Skinner HB, Mote CD. 1990. Automated three-dimensional finite element modelling of bone: a new method. J Biomed Eng. 12(5):389–397.

Khan M, Madden K, Burrus MT, Rogowski JP, Stotts J, Samani MJ, Sikka R, Bedi A. 2018. Epidemiology and Impact on Performance of Lower Extremity Stress Injuries in Professional Basketball Players. Sport Heal A Multidiscip Approach. 10(2):169–174.

Khassetarash A, Haider I, Baggaley M, Edwards WB. 2023. Tibial Strains During Prolonged Downhill Running: A Finite Element Analysis. J Biomech Eng. 145(4).

Kijowski R, Choi J, Shinki K, Del Rio AM, De Smet A. 2012. Validation of MRI classification system for tibial stress injuries. Am J Roentgenol. 198(4):878–884.

Kimata K, Otsuka S, Yokota H, Shan X, Hatayama N, Naito M. 2022. Relationship between attachment site of tibialis anterior muscle and shape of tibia: anatomical study of cadavers. J Foot Ankle Res. 15(1):54.

Klein-Nulend J, Bakker AD, Bacabac RG, Vatsa A, Weinbaum S. 2013. Mechanosensation and

transduction in osteocytes. Bone. 54(2):182–190.

Kliethermes SA, Stiffler-Joachim MR, Wille CM, Sanfilippo JL, Zavala P, Heiderscheit BC. 2021. Lower step rate is associated with a higher risk of bone stress injury: a prospective study of collegiate cross country runners. Br J Sports Med. 55(15):851–856.

Knapik J, Montain S, McGraw S, Grier T, Ely M, Jones B. 2012. Stress Fracture Risk Factors in Basic Combat Training. Int J Sports Med. 33(11):940–946.

Koltun KJ, Sekel NM, Bird MB, Lovalekar M, Mi Q, Martin BJ, Nindl BC. 2022. Tibial Bone Geometry Is Associated With Bone Stress Injury During Military Training in Men and Women. Front Physiol. 13.

Komatsu J, Mogami A, Iwase H, Obayashi O, Kaneko K. 2019. A complete posterior tibial stress fracture that occurred during a middle-distance running race: a case report. Arch Orthop Trauma Surg. 139(1):25–33.

Krysztoforski K, Krowicki P, Świątek-Najwer E, Będziński R, Keppler P. 2011. Noninvasive ultrasonic measuring system for bone geometry examination. Int J Med Robot Comput Assist Surg. 7(1):85–95.

Lanyon LE, Hampson WGJ, Goodship AE, Shah JS. 1975. Bone deformation recorded in vivo from strain gauges attached to the human tibial shaft. Acta Orthop. 46(2):256–268.

Lappe J, Cullen D, Haynatzki G, Recker R, Ahlf R, Thompson K. 2008. Calcium and Vitamin D Supplementation Decreases Incidence of Stress Fractures in Female Navy Recruits. J Bone Miner Res. 23(5):741–749.

Lassen NE, Andersen TL, Pløen GG, Søe K, Hauge EM, Harving S, Eschen GET, Delaisse J-M. 2017. Coupling of Bone Resorption and Formation in Real Time: New Knowledge Gained From Human Haversian BMUs. J Bone Miner Res. 32(7):1395–1405.

Li X, Zhang Y, Kang H, Liu W, Liu P, Zhang J, Harris SE, Wu D. 2005. Sclerostin Binds to LRP5/6 and Antagonizes Canonical Wnt Signaling. J Biol Chem. 280(20):19883–19887.

Loundagin LL, Edwards WB. 2020. Stressed volume around vascular canals explains compressive fatigue life variation of secondary osteonal bone but not plexiform bone. J Mech Behav Biomed Mater. 111:104002.

Loundagin LL, Pohl AJ, Edwards WB. 2021. Stressed volume estimated by finite element analysis predicts the fatigue life of human cortical bone: The role of vascular canals as stress concentrators. Bone. 143:115647.

Luedeke LE, Heiderscheit BC, Williams DSB, Rauh MJ. 2016. Influence of Step Rate on Shin Injury and Anterior Knee Pain in High School Runners. Med Sci Sport Exerc. 48(7):1244–1250.

Mahfouz M, Fatah EEHA, Bowers LS, Scuderi G. 2012. Three-dimensional morphology of the knee reveals ethnic differences. Clin Orthop Relat Res. 470(1):172–185.

Majeska RJ. 2001. Cell Biology of Bone. In: Cowin SC, editor. Bone Mech Handb. 2nd ed. CRC Press.

Manske SL, Zhu Y, Sandino C, Boyd SK. 2015. Human trabecular bone microarchitecture can be assessed independently of density with second generation HR-pQCT. Bone. 79:213–221.

Marchetti DC, Moatshe G, Phelps BM, Dahl KD, Ferrari MB, Chahla J, Turnbull TL, LaPrade RF. 2017. The proximal tibiofibular joint: A biomechanical analysis of the anterior and posterior ligamentous complexes. Am J Sports Med. 45(8):1888–1892.

Marieb EN, Hoehn K. 2013. Human Anatomy and Physiology. 9th ed. Glenview, IL: Pearson Education.

Martelli S, Valente G, Viceconti M, Taddei F. 2015. Sensitivity of a subject-specific musculoskeletal model to the uncertainties on the joint axes location. Comput Methods Biomech Biomed Engin. 18(14):1555–1563.

Martin R. Bruce, Burr DB, Sharkey NA, Fyhrie DP. 2015. Growth, Modeling and Remodeling of Bone. In: Skelet Tissue Mech. New York, NY: Springer New York; p. 95–173.

Martin R.B., Burr DB, Sharkey NA, Fyhrie DP. 2015. Mechanical Properties of Bone. In: Skelet Tissue Mech. 2nd ed. New York, NY: Springer; p. 355–422.

Matheson GO, Clement DB, Mckenzie DC, Taunton JE, Lloyd-Smith DR, Macintyre JG. 1987. Stress fractures in athletes. Am J Sports Med. 15(1):46–58.

McInnis KC, Ramey LN. 2016. High-Risk Stress Fractures: Diagnosis and Management. PM&R. 8(3S):S113–S124.

Meardon SA, Derrick TR, Willson JD, Baggaley M, Steinbaker CR, Marshall M, Willy RW. 2021. Peak and Per-Step Tibial Bone Stress During Walking and Running in Female and Male Recreational Runners. Am J Sports Med. 49(8):2227–2237.

Mei L, Figl M, Rueckert D, Darzi A, Edwards P. 2008. Sample sufficiency and number of modes to retain in statistical shape modelling. In: Metaxas D, Axel L, Fichtinger G, Szekely G, editors. Lect Notes Comput Sci. Berlin: Springer; p. 425–433.

Milgrom C. 2000. Do high impact exercises produce higher tibial strains than running? Br J Sports Med. 34(3):195–199.

Milgrom C, Burr D, Fyhrie D, Forwood M, Finestone A, Nyska M, Giladi M, Liebergall M, Simkin A. 1996. The Effect of Shoe Gear on Human Tibial Strains Recorded During Dynamic Loading: A Pilot Study. Foot Ankle Int. 17(11):667–671.

Milgrom C, Finestone A, Novack V, Pereg D, Goldich Y, Kreiss Y, Zimlichman E, Kaufman S, Liebergall M, Burr D. 2004. The effect of prophylactic treatment with risedronate on stress fracture incidence among infantry recruits. Bone. 35(2):418–424.

Milgrom C, Finestone A, Segev S, Olin C, Arndt T, Ekenman I. 2003. Are overground or treadmill runners more likely to sustain tibial stress fracture? Br J Sports Med. 37(2):160–163.

Milgrom C, Finestone A, Sharkey N, Hamel A, Mandes V, Burr D, Arndt A, Ekenman I. 2002. Metatarsal Strains Are Sufficient to Cause Fatigue Fracture During Cyclic Overloading. Foot Ankle Int. 23(3):230–235.

Milgrom C, Simkin A, Eldad A, Nyska M, Finestone A. 2000. Using bone's adaptation ability to lower the incidence of stress fractures. Am J Sports Med. 28(2):245–251.

Milner CE, Ferber R, Pollard CD, Hamill J, Davis IS. 2006. Biomechanical Factors Associated with Tibial Stress Fracture in Female Runners. Med Sci Sport Exerc. 38(2):323–328.

Modenese L, Renault J-B. 2021. Automatic generation of personalised skeletal models of the lower limb from three-dimensional bone geometries. J Biomech. 116:110186.

Mountjoy M, Sundgot-Borgen J, Burke L, Carter S, Constantini N, Lebrun C, Meyer N, Sherman R, Steffen K, Budgett R, Ljungqvist A. 2014. The IOC consensus statement: beyond the Female Athlete Triad—Relative Energy Deficiency in Sport (RED-S). Br J Sports Med. 48(7):491–497.

Murray SR, Reeder MT, Udermann BE, Pettitt RW. 2006. High-Risk Stress Fractures: Pathogenesis, Evaluation, and Treatment. Compr Ther. 32(1):20–25.

Myronenko A, Song X. 2010. Point set registration: Coherent point drifts. IEEE Trans Pattern Anal Mach Intell. 32(12):2262–2275.

Nattiv A, Kennedy G, Barrack MT, Abdelkerim A, Goolsby MA, Arends JC, Seeger LL. 2013. Correlation of MRI Grading of Bone Stress Injuries With Clinical Risk Factors and Return to Play. Am J Sports Med. 41(8):1930–1941.

Nicolella DP, Bonewald LF, Moravits DE, Lankford J. 2005. Measurement of microstructural strain in cortical bone. Eur J Morphol. 42(1–2):23–29.

Nicolella DP, Bredbenner TL. 2012. Development of a parametric finite element model of the proximal femur using statistical shape and density modelling. Comput Methods Biomech Biomed Engin. 15(2):101–110.

Nicolella DP, Moravits DE, Gale AM, Bonewald LF, Lankford J. 2006. Osteocyte lacunae tissue strain in cortical bone. J Biomech. 39(9):1735–1743.

Nieves JW, Formica C, Ruffing J, Zion M, Garrett P, Lindsay R, Cosman F. 2005. Males have larger skeletal size and bone mass than females, despite comparable body size. J Bone Miner Res. 20(3):529–535.

Nieves JW, Melsop K, Curtis M, Kelsey JL, Bachrach LK, Greendale G, Sowers MF, Sainani KL. 2010. Nutritional Factors That Influence Change in Bone Density and Stress Fracture Risk Among Young Female Cross-Country Runners. PM&R. 2(8):740–750.

Nolte D, Ko S-T, Bull AMJ, Kedgley AE. 2020. Reconstruction of the lower limb bones from digitised anatomical landmarks using statistical shape modelling. Gait Posture. 77(March 2019):269–275.

Nolte D, Tsang CK, Zhang KY, Ding Z, Kedgley AE, Bull AMJ. 2016. Non-linear scaling of a musculoskeletal model of the lower limb using statistical shape models. J Biomech. 49(14):3576–3581.

O'Brien FJ, Hardiman DA, Hazenberg JG, Mercy M V., Mohsin S, Taylor D, Lee TC. 2005. The behaviour of microcracks in compact bone. Eur J Morphol. 42(1–2):71–79.

O'Leary TJ, Izard RM, Tang JCY, Fraser WD, Greeves JP. 2022. Sex differences in tibial adaptations to arduous training: An observational cohort study. Bone. 160:116426.

Osis ST, Hettinga BA, Macdonald S, Ferber R. 2016. Effects of simulated marker placement deviations on running kinematics and evaluation of a morphometric-based placement feedback method. PLoS One. 11(1):1–13.

Papageorgiou M, Elliott-Sale KJ, Parsons A, Tang JCY, Greeves JP, Fraser WD, Sale C. 2017. Effects of reduced energy availability on bone metabolism in women and men. Bone. 105:191–199.

Pattin CA, Caler WE, Carter DR. 1996. Cyclic mechanical property degradation during fatigue loading of cortical bone. J Biomech. 29(1):69–79.

Pegrum J, Crisp T, Padhiar N. 2012. Diagnosis and management of bone stress injuries of the lower limb in athletes. BMJ. 344(7854):1–8.

Pettersson U, Nordstro P, Alfredson H. 2000. Effect of High Impact Activity on Bone Mass and Size in Adolescent Females : A Comparative Study Between Two Different Types of Sports. Calcif Tissue Int. 67:207–214.

Poelert S, Valstar E, Weinans H, Zadpoor AA. 2013. Patient-specific finite element modeling of bones. Proc Inst Mech Eng Part H J Eng Med. 227(4):464–478.

Pomidor BJ, Makedonska J, Slice DE. 2016. A landmark-free method for three-dimensional shape analysis. PLoS One. 11(3):1–18.

Popp KL, Frye AC, Stovitz SD, Hughes JM. 2020. Bone geometry and lower extremity bone stress injuries in male runners. J Sci Med Sport. 23(2):145–150.

Qin L, Liu W, Cao H, Xiao G. 2020. Molecular mechanosensors in osteocytes. Bone Res. 8(1):23.

Real R, Vargas JM. 1996. The Probabilistic Basis of Jaccard's Index of Similarity.Olmstead R, editor. Syst Biol. 45(3):380–385.

Reznikov N, Shahar R, Weiner S. 2014. Bone hierarchical structure in three dimensions. Acta Biomater. 10(9):3815–3826.

Rho J-Y. 1996. An ultrasonic method for measuring the elastic properties of human tibial cortical and cancellous bone. Ultrasonics. 34(8):777–783.

Rho J-Y, Kuhn-Spearing L, Zioupos P. 1998. Mechanical properties and the hierarchical structure of bone. Med Eng Phys. 20(2):92–102.

Rizzone KH, Ackerman KE, Roos KG, Dompier TP, Kerr ZY. 2017. The Epidemiology of Stress Fractures in Collegiate Student-Athletes, 2004–2005 Through 2013–2014 Academic Years. J Athl Train. 52(10):966–975.

Robling AG, Burr DB, Turner CH. 2001. Recovery periods restore mechanosensitivity to dynamically loaded bone. J Exp Biol. 204(Pt 19):3389–3399.

Robling AG, Hinant FM, Burr DB, Turner CH. 2002. Shorter, more frequent mechanical loading sessions enhance bone mass. Med Sci Sports Exerc. 34(2):196–202.

Robling AG, Niziolek PJ, Baldridge LA, Condon KW, Allen MR, Alam I, Mantila SM, Gluhak-Heinrich J, Bellido TM, Harris SE, Turner CH. 2008. Mechanical Stimulation of Bone in Vivo Reduces Osteocyte Expression of Sost/Sclerostin. J Biol Chem. 283(9):5866–5875.

Rolfe C, Westblad P, Ekenman I, Lundberg A, Murphy N, Lamontagne M, Halvorsen K. 1997. An experimental in vivo method for analysis of local deformation on tibia, with simultaneous measures of ground reaction forces, lower extremity muscle activity and joint motion. Scand J Med Sci Sport. 7:144–151.

Rubin CT, Lanyon LE. 1984. Regulation of bone formation by applied dynamic loads. J Bone Joint Surg Am. 66(3):397–402.

Rubin CT, Lanyon LE. 1985. Regulation of bone mass by mechanical strain magnitude. Calcif Tissue Int. 37(4):411–417.

Ruff CB, Hayes WC. 1988. Sex differences in age-related remodeling of the femur and tibia. J Orthop Res. 6(6):886–896.

Sarkalkan N, Weinans H, Zadpoor AA. 2014. Statistical shape and appearance models of bones. Bone. 60:129–140.

Schanda JE, Kocijan R, Resch H, Baierl A, Feichtinger X, Mittermayr R, Plachel F, Wakolbinger R, Wolff K, Fialka C, et al. 2019. Bone Stress Injuries Are Associated With Differences in Bone Microarchitecture in Male Professional Soldiers. J Orthop Res. 37(12):2516–2523.

Scheys L, Spaepen A, Suetens P, Jonkers I. 2008. Calculated moment-arm and muscle-tendon lengths during gait differ substantially using MR based versus rescaled generic lower-limb musculoskeletal models. Gait Posture. 28(4):640–648.

Schipilow JD, Macdonald HM, Liphardt AM, Kan M, Boyd SK. 2013. Bone micro-architecture, estimated bone strength, and the muscle-bone interaction in elite athletes: An HR-pQCT study. Bone. 56(2):281–289.

Schnackenburg KE, Macdonald HM, Ferber R, Wiley JP, Boyd SK. 2011. Bone Quality and Muscle Strength in Female Athletes with Lower Limb Stress Fractures. Med Sci Sport Exerc. 43(11):2110–2119.

Schneider P, Meier M, Wepf R, Müller R. 2010. Towards quantitative 3D imaging of the osteocyte lacuno-canalicular network. Bone. 47(5):848–858.

Schuler B, Fritscher KD, Kuhn V, Eckstein F, Link TM, Schubert R. 2010. Assessment of the individual fracture risk of the proximal femur by using statistical appearance models. Med Phys. 37:2560–2571.

Scott S, Winter DA. 1990. Internal forces of chronic running injury sites. Med Sci Sports Exerc. 22(3):357–369.

Seth A, Hicks JL, Uchida TK, Habib A, Dembia CL, Dunne JJ, Ong CF, DeMers MS, Rajagopal A, Millard M, et al. 2018. OpenSim: Simulating musculoskeletal dynamics and neuromuscular control to study human and animal movement. PLoS Comput Biol.

Shaffer RA, Rauh MJ, Brodine SK, Trone DW, Macera CA. 2006. Predictors of Stress Fracture

Susceptibility in Young Female Recruits. Am J Sports Med. 34(1):108–115.

Sherk VD, Bemben DA, Bemben MG, Anderson MA. 2012. Age and sex differences in tibia morphology in healthy adult Caucasians. Bone. 50(6):1324–1331.

Sintini I. 2017. Statistical Shape and Intensity Modeling of the Shoulder. University of Denver. https://digitalcommons.du.edu/etd/1478

Sintini I, Burton WS, Sade P, Chavarria JM, Laz PJ. 2018. Investigating gender and ethnicity differences in proximal humeral morphology using a statistical shape model. J Orthop Res. 36(11):3043–3052.

Smock AJ, Hughes JM, Popp KL, Wetzsteon RJ, Stovitz SD, KAUFMAN BC, Kurzer MS, Petit MA. 2009. Bone Volumetric Density, Geometry, and Strength in Female and Male Collegiate Runners. Med Sci Sport Exerc. 41(11):2026–2032.

Soucie JM, Wang C, Forsyth A, Funk S, Denny M, Roach KE, Boone D. 2011. Range of motion measurements: Reference values and a database for comparison studies. Haemophilia. 17(3):500–507.

Statistics Canada. 2015a. Table 23 Measured weight, by age and sex, household population, Canada, 2009 to 2011 [Data table] [Internet]. [accessed 2023 Mar 3]. https://www150.statcan.gc.ca/n1/pub/82-626-x/2013001/t024-eng.htm

Statistics Canada. 2015b. Table 22 Measured standing height, by age and sex, household population, Canada, 2009 to 2011 [Data table] [Internet]. [accessed 2023 Mar 3]. https://www150.statcan.gc.ca/n1/pub/82-626-x/2013001/t023-eng.htm#shr-pg0

Sumnik Z, Land C, Coburger S, Neu C, Manz F, Hrach K, Schoenau E. 2006. The muscle-bone unit in adulthood: influence of sex, height, age and gynecological history on the bone mineral content and muscle cross-sectional area. J Musculoskelet Neuronal Interact. 6(2):195–200.

Suwarganda EK, Diamond LE, Lloyd DG, Besier TF, Zhang J, Killen BA, Savage TN, Saxby DJ. 2019. Minimal medical imaging can accurately reconstruct geometric bone models for musculoskeletal models.Livesu M, editor. PLoS One. 14(2):e0205628.

Taghizadeh E, Terrier A, Becce F, Farron A, Büchler P. 2019. Automated CT bone segmentation using statistical shape modelling and local template matching. Comput Methods Biomech Biomed Engin. 22(16):1303–1310.

Taylor D. 1998. Fatigue of bone and bones: An analysis based on stressed volume. J Orthop Res. 16(2):163–169.

Taylor D, Casolari E, Bignardi C. 2004. Predicting stress fractures using a probabilistic model of damage, repair and adaptation. J Orthop Res. 22(3):487–494.

Taylor D, O'Brien F, Prina-Mello A, Ryan C, O'Reilly P, Lee TC. 1999. Compression data on bovine bone confirms that a "stressed volume" principle explains the variability of fatigue strength results. J Biomech. 32(11):1199–1203.

Tenforde AS, Brook EM, Broad E, Matzkin EG, Yang HY, Collins JE, Braun PW, Blauwet CA. 2019. Prevalence and Anatomical Distribution of Bone Stress Injuries in the Elite Para Athlete.

Am J Phys Med Rehabil. 98(11):1036–1040.

Tommasini SM, Nasser P, Jepsen KJ. 2007. Sexual dimorphism affects tibia size and shape but not tissue-level mechanical properties. Bone. 40(2):498–505.

Tong J, Subramani A V., Kote V, Baggaley M, Edwards WB, Reifman J. 2023. Effects of Stature and Load Carriage on the Running Biomechanics of Healthy Men. IEEE Trans Biomed Eng. February 2023:1–9.

Tümer N, Arbabi V, Gielis WP, de Jong PA, Weinans H, Tuijthof GJM, Zadpoor AA. 2019. Three-dimensional analysis of shape variations and symmetry of the fibula, tibia, calcaneus and talus. J Anat. 234(1):132–144.

Turner CH. 1998. Three Rules for Bone Adapation to Mechanical Stimuli. Bone. 23(5):399–407.

Umemura Y, Ishiko T, Yamauchi T, Kurono M, Mashiko S. 1997. Five Jumps per Day Increase Bone Mass and Breaking Force in Rats. J Bone Miner Res. 12(9):1480–1485.

Unnikrishnan G, Xu C, Baggaley M, Tong J, Kulkarni S, Edwards WB, Reifman J. 2021. Effects of body size and load carriage on lower-extremity biomechanical responses in healthy women. BMC Musculoskelet Disord. 22(1):219.

Väänänen SP, Grassi L, Flivik G, Jurvelin JS, Isaksson H. 2015. Generation of 3D shape, density, cortical thickness and finite element mesh of proximal femur from a DXA image. Med Image Anal. 24(1):125–134.

Välimäki V-V, Alfthan H, Lehmuskallio E, Löyttyniemi E, Sahi T, Suominen H, Välimäki MJ. 2005. Risk factors for clinical stress fractures in male military recruits: A prospective cohort study. Bone. 37(2):267–273.

Varzi D, Coupaud SAF, Purcell M, Allan DB, Gregory JS, Barr RJ. 2015. Bone morphology of the femur and tibia captured by statistical shape modelling predicts rapid bone loss in acute spinal cord injury patients. Bone. 81:495–501.

Vaughan CL, Davis BL, O'Conner JC. 1999. Dynamics of Human Gait. Human Kinetics.

Vlachopoulos D, Barker AR, Ubago-Guisado E, Williams CA, Gracia-Marco L. 2018. A 9-Month jumping intervention to improve bone geometry in adolescent male athletes. Med Sci Sports Exerc. 50(12):2544–2554.

de Vree JHP, Brekelmans WAM, van Gils MAJ. 1995. Comparison of nonlocal approaches in continuum damage mechanics. Comput Struct. 55(4):581–588.

Wang H, Kia M, Dickin DC. 2016. Influences of load carriage and physical activity history on tibia bone strain. J Sport Heal Sci. 8(5):478-485.

Warden SJ, Edwards WB, Willy RW. 2021a. Preventing Bone Stress Injuries in Runners with Optimal Workload. Curr Osteoporos Rep. 19(3):298–307.

Warden SJ, Edwards WB, Willy RW. 2021b. Optimal Load for Managing Low-Risk Tibial and Metatarsal Bone Stress Injuries in Runners: The Science Behind the Clinical Reasoning. J Orthop Sport Phys Ther. 51(7):322–330.

Winfield AC, Moore J, Bracker M, Johnson CW. 1997. Risk Factors Associated with Stress Reactions in Female Marines. Mil Med. 162(10):698–702.

Wise BL, Liu F, Kritikos L, Lynch JA, Parimi N, Zhang Y, Lane NE. 2016. The association of distal femur and proximal tibia shape with sex: The Osteoarthritis Initiative. Semin Arthritis Rheum. 46(1):20–26.

Wood AM, Hales R, Keenan A, Moss A, Chapman M, Davey T, Nelstrop A. 2014. Incidence and Time to Return to Training for Stress Fractures during Military Basic Training. J Sports Med. 2014:1–5.

Wright AA, Taylor JB, Ford KR, Siska L, Smoliga JM. 2015. Risk factors associated with lower extremity stress fractures in runners: a systematic review with meta-analysis. Br J Sports Med. 49(23):1517–1523.

Xu C, Reifman J, Baggaley M, Edwards WB, Unnikrishnan G. 2020. Individual Differences in Women During Walking Affect Tibial Response to Load Carriage: The Importance of Individualized Musculoskeletal Finite-Element Models. IEEE Trans Biomed Eng. 67(2):545–555.

Xu C, Silder A, Zhang J, Hughes J, Unnikrishnan G, Reifman J, Rakesh V. 2016. An Integrated Musculoskeletal-Finite-Element Model to Evaluate Effects of Load Carriage on the Tibia during Walking. J Biomech Eng. 138(10).

Xu C, Silder A, Zhang J, Reifman J, Unnikrishnan G. 2017. A cross-sectional study of the effects of load carriage on running characteristics and tibial mechanical stress: implications for stress-fracture injuries in women. BMC Musculoskelet Disord. 18(1):125.

Yang PF, Brüggemann GP, Rittweger J. 2011. What do we currently know from in vivo bone strain measurements in humans? J Musculoskelet Neuronal Interact. 11(1):8–20.

Yang PF, Sanno M, Ganse B, Koy T, Brüggemann GP, Müller LP, Rittweger J. 2014. Torsion and antero-posterior bending in the in vivo human tibia loading regimes during walking and running. PLoS One. 9(4).

Zhang J, Besier TF. 2017. Accuracy of femur reconstruction from sparse geometric data using a statistical shape model. Comput Methods Biomech Biomed Engin. 20(5):566–576.

Zhang J, Fernandez J, Hislop-Jambrich J, Besier TF. 2016. Lower limb estimation from sparse landmarks using an articulated shape model. J Biomech. 49(16):3875–3881.

Zhang J, Malcolm D, Hislop-Jambrich J, Thomas CDL, Nielsen PMF. 2014. An anatomical region-based statistical shape model of the human femur. Comput Methods Biomech Biomed Eng Imaging Vis. 2(3):176–185.

Zhang J, Sorby H, Clement J, Thomas CDL, Hunter P, Nielsen P, Lloyd D, Taylor M, Besier T. 2014. The MAP Client: User-Friendly Musculoskeletal Modelling Workflows. In: Int Symp Biomed Simul. Strasbourg; p. 182–192.

# Appendix A Supplemental Information for Ch. 3

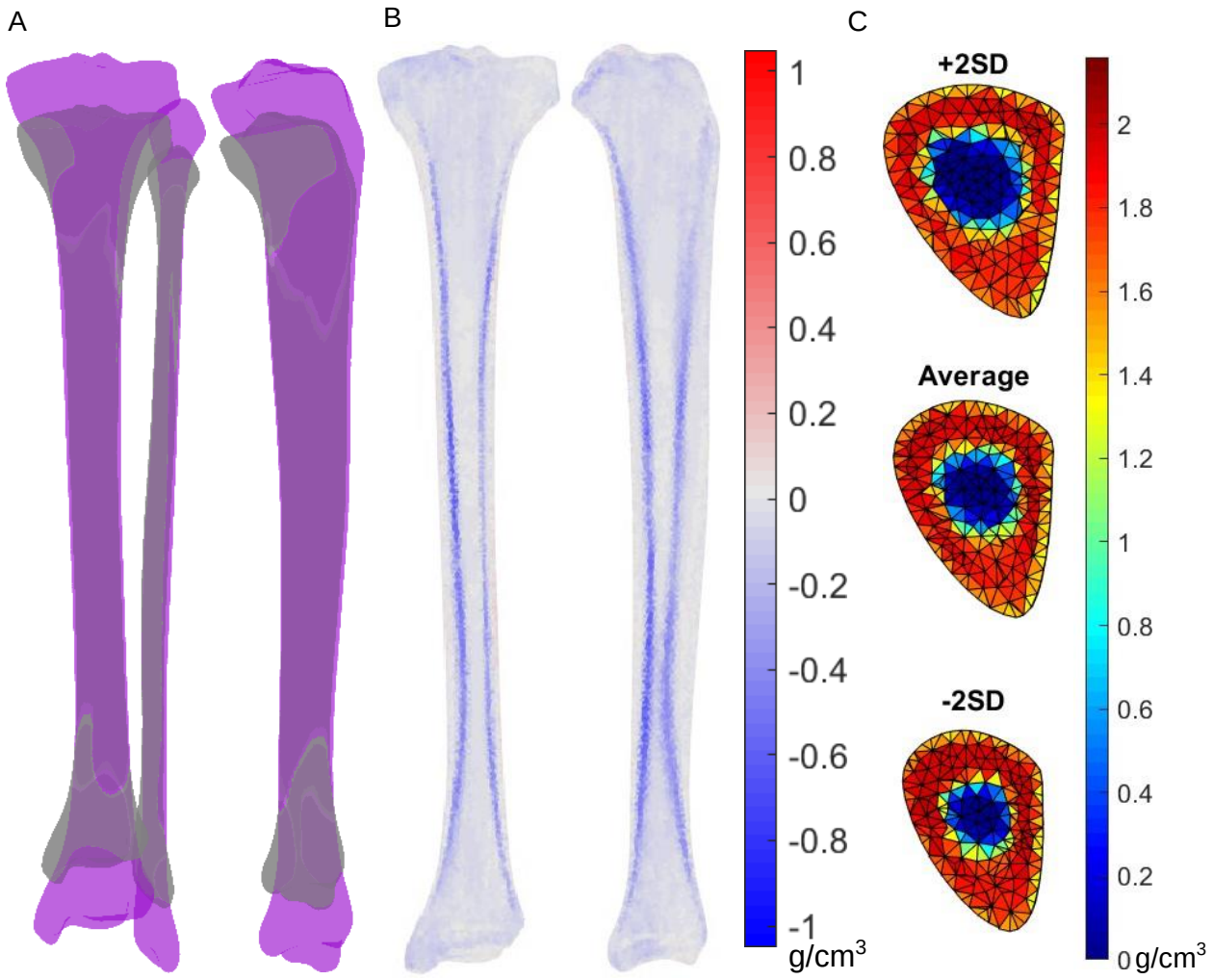


*Figure A.1 Geometry and density variations characterised by the first principal component. (A) Surface geometry of the tibia and fibula perturbed by +2 standard deviations (SD) (purple) and the average geometries (grey). (B) Frontal (left) and sagittal (right) cross-sections of the tibia illustrating differences in internal density distribution between +2 SD and average, where red indicates greater density in the model perturbed by +2 SD. (C) Axial cross-sections of the tibial diaphysis at 50% of total axial length.*

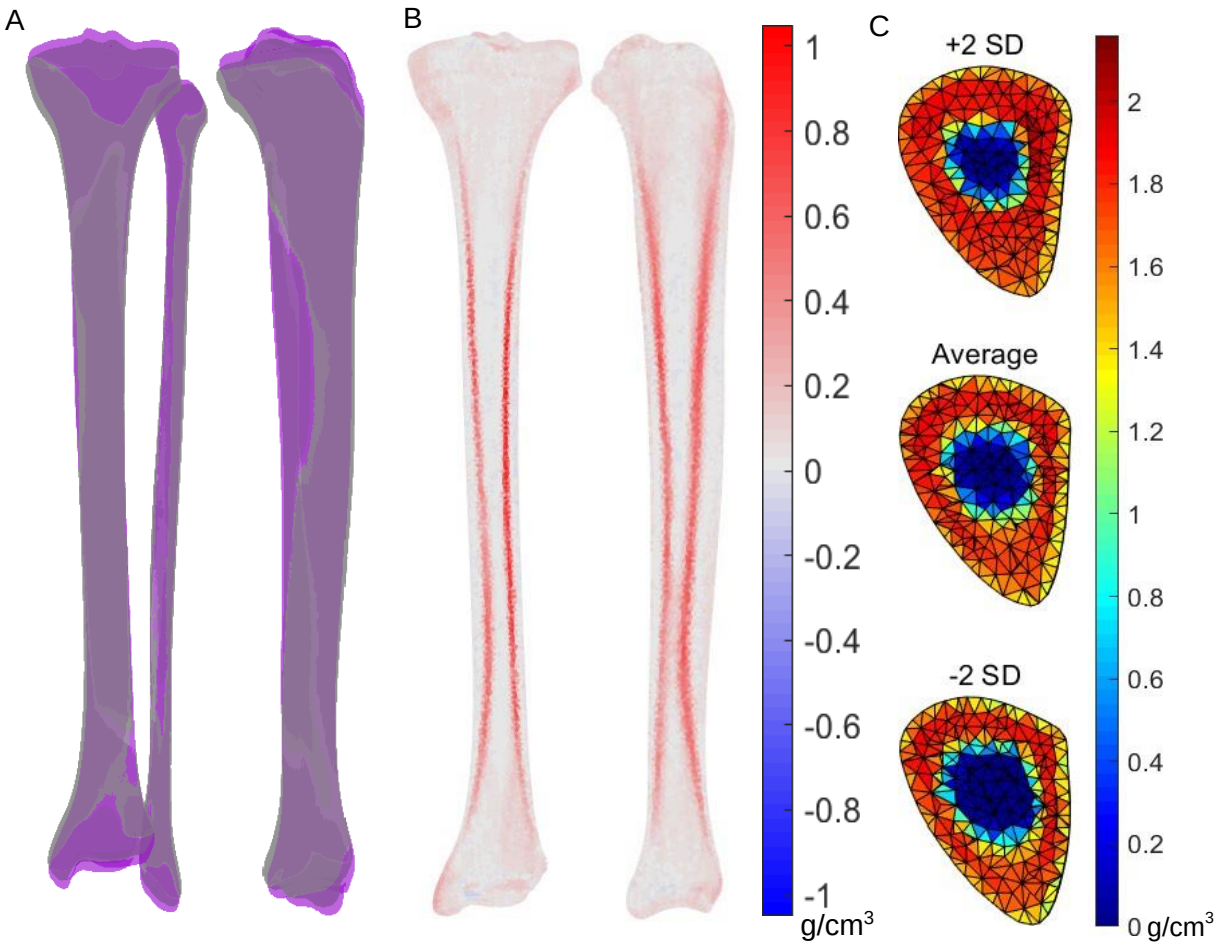


*Figure A.2 Geometry and density variations characterised by the second principal component (Presented in main article, Figure 1). Surface geometry of the tibia and fibula perturbed by +2 standard deviations (SD) (purple) and the average geometries (grey). (B) Frontal (left) and sagittal (right) cross-sections of the tibia illustrating differences in internal density distribution between +2 SD and average, where red indicates greater density in the model perturbed by +2 SD. (C) Axial cross-sections of the tibial diaphysis at 50% of total axial length.*

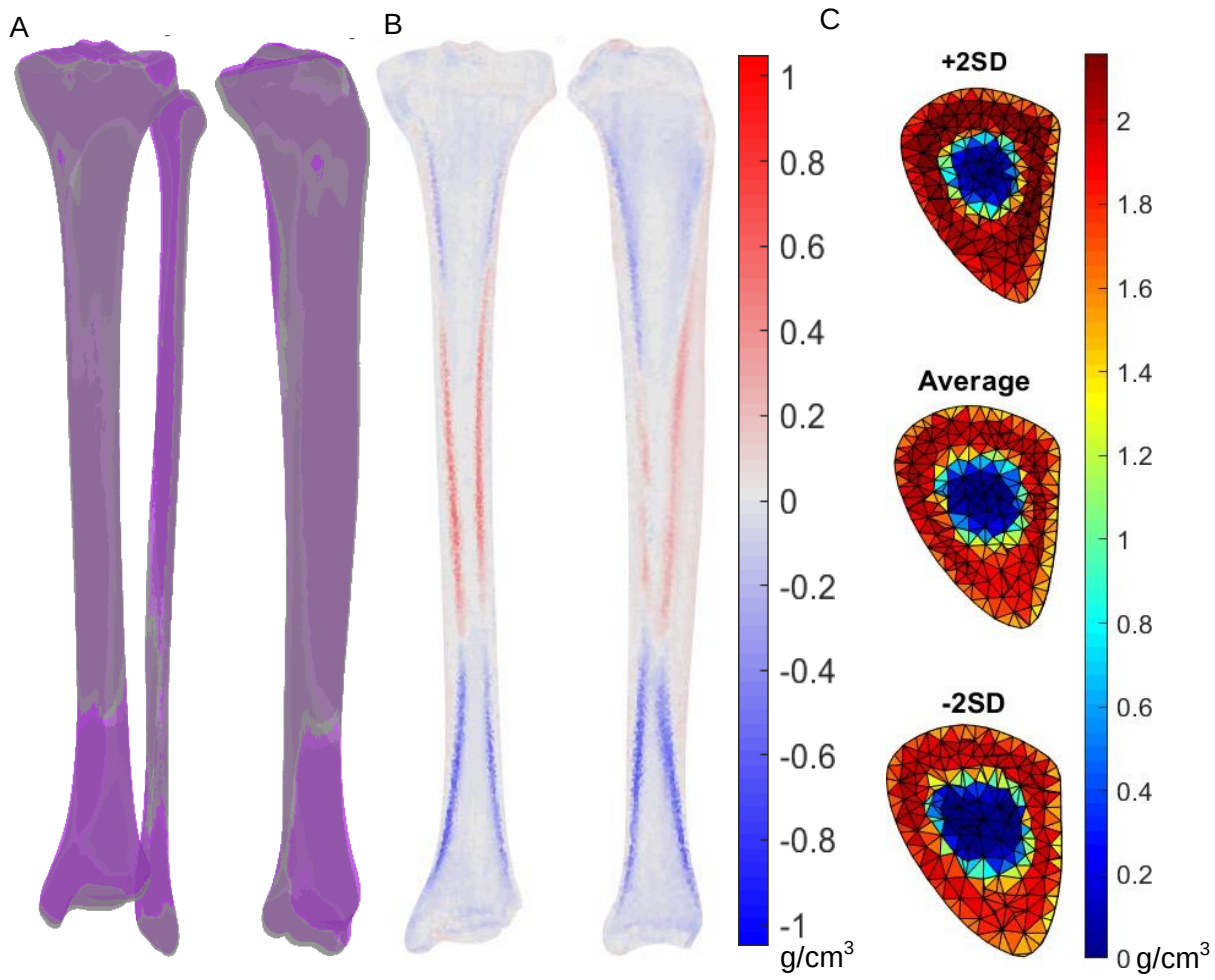


*Figure A.3 Geometry and density variations characterised by the third principal component. Surface geometry of the tibia and fibula perturbed by +2 standard deviations (SD) (purple) and the average geometries (grey). (B) Frontal (left) and sagittal (right) cross-sections of the tibia illustrating differences in internal density distribution between +2 SD and average, where red indicates greater density in the model perturbed by +2 SD. (C) Axial cross-sections of the tibial diaphysis at 50% of total axial length.*

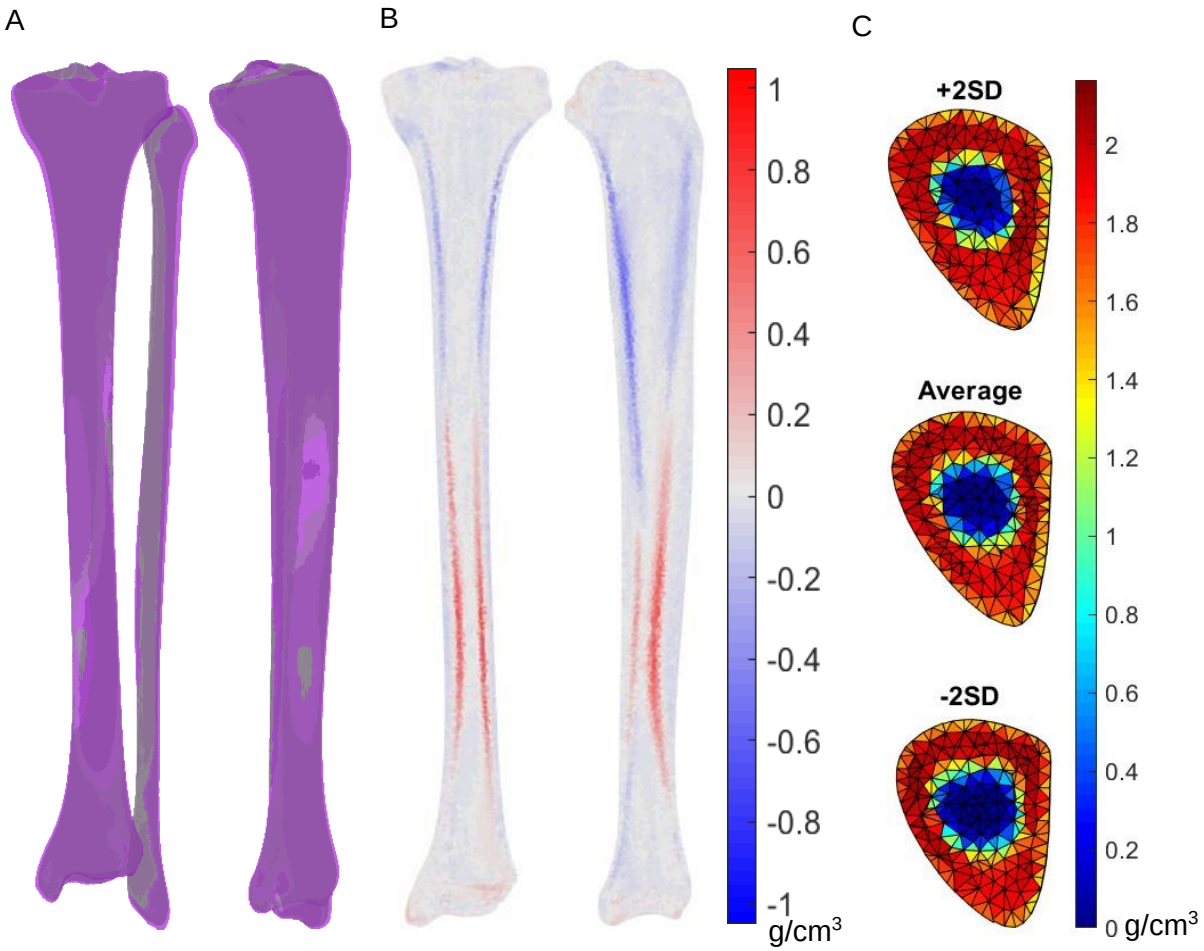


*Figure A.4 Geometry and density variations characterised by the fourth principal component. Surface geometry of the tibia and fibula perturbed by +2 standard deviations (SD) (purple) and the average geometries (grey). (B) Frontal (left) and sagittal (right) cross-sections of the tibia illustrating differences in internal density distribution between +2 SD and average, where red indicates greater density in the model perturbed by +2 SD. (C) Axial cross-sections of the tibial diaphysis at 50% of total axial length.*

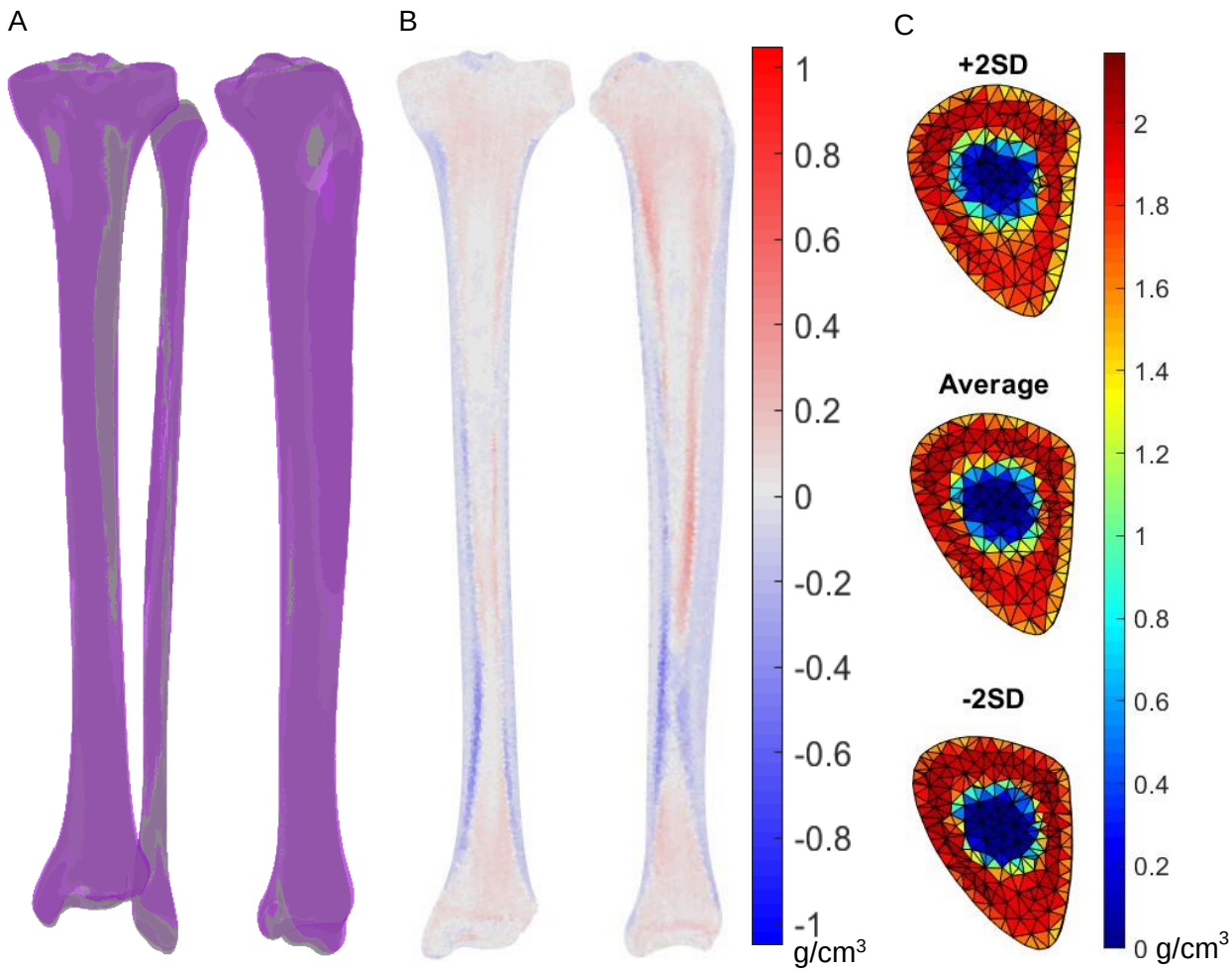


*Figure A.5 Geometry and density variations characterised by the fifth principal component. Surface geometry of the tibia and fibula perturbed by +2 standard deviations (SD) (purple) and the average geometries (grey). (B) Frontal (left) and sagittal (right) cross-sections of the tibia illustrating differences in internal density distribution between +2 SD and average, where red indicates greater density in the model perturbed by +2 SD. (C) Axial cross-sections of the tibial diaphysis at 50% of total axial length.*

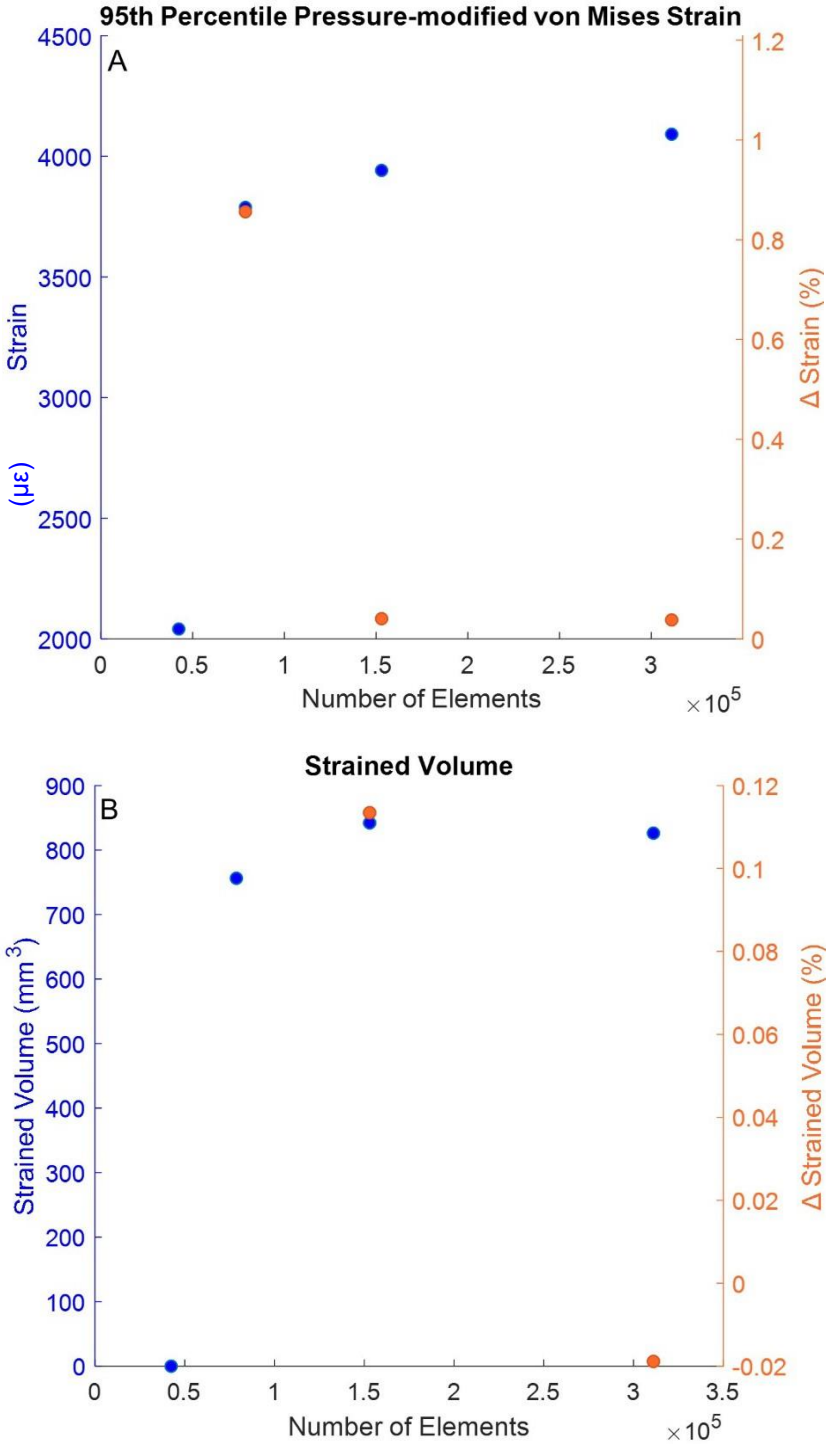


*Figure A.6 Mesh convergence analysis results. Blue dots show the peak strain (A) or strained volume (B) resulting from each mesh. Orange dots show the percentage change in peak strain or strained volume when compared to the previous (coarser) mesh. Strained volume resulting from the mesh with 42 413 elements was zero. As a result, the % change in strained volume between the 78 749 element mesh and the 42 413 element mesh was infinite and therefore not plotted*

*Table A.1 Muscles included in the musculoskeletal model attaching to the tibia or fibula* and the forces applied to the finite element model, calculated from one female participant at the time of peak resultant ankle joint contact force. The ankle joint contact force applied at the ankle center of rotation is also shown. +: medial, anterior, proximal*

| **Muscle** | **Muscle force applied to the tibia (N)** | | |
|---|---|---|---|
| | Medial/Lateral | Anterior/Posterior | Axial |
| **Semimembranosus** | -0.24 | -2.16 | 2.14 |
| **Semitendinosus** | 0.22 | -0.82 | 0.71 |
| **Biceps femoris long head** | 0.05 | -0.69 | 0.69 |
| **Biceps femoris short head** | -0.54 | -6.17 | 11.48 |
| **Sartorius** | 24.03 | -31.38 | 25.60 |
| **TFL** | -32.83 | -5.76 | 275.95 |
| **Gracilis** | 0.00 | -0.36 | 0.49 |
| **Soleus** | 238.08 | -272.39 | -1930.42 |
| **Tibialis posterior** | 17.84 | -5.28 | -83.25 |
| **Flexor digitorum** | 4.28 | -2.68 | -27.56 |
| **Flexor hallucis** | 68.25 | 9.22 | -242.60 |
| **Tibialis anterior** | 0.19 | 0.19 | -1.19 |
| **Peroneus brevis** | 25.34 | -20.92 | -261.79 |
| **Peroneus longus** | 51.63 | -25.42 | -453.93 |
| **Peroneus tertius** | 0.99 | 2.00 | -10.98 |
| **Extensor digitorum** | 2.29 | 2.01 | -17.45 |
| **Extensor hallucis** | 0.79 | 0.96 | -6.71 |
| **Patellar ligament** | 220.47 | 1679.08 | 3392.13 |
| **Ankle contact force** | 714.20 | -1087.17 | 6241.07 |

* Muscles included in the musculoskeletal model that do not attach to the tibia or fibula were: gluteus maximus, gluteus medius, gluteus minimus, adductor longus, adductor brevis, adductor magnus, pectineus, iliacus, psoas, quadratus femoris, gemellus, piriformis, rectus femoris, vastus lateralis, vastus medialis, vastus intermedius, medial gastrocnemius, lateral gastrocnemius.

Musculoskeletal model:
E.M. Arnold, S.R. Ward, R.L. Lieber, S.L. Delp, A model of the lower limb for analysis of human movement, Ann. Biomed. Eng. (2010). https://doi.org/10.1007/s10439-009-9852-5.

*Table A.2 Muscle and joint contact forces applied to the tibia and fibula calculated from one male participant at the time of peak resultant ankle joint contact force. +: medial, anterior, proximal*

| **Muscle** | **Muscle force applied to the tibia (N)** | | |
|---|---|---|---|
| | Medial/Lateral | Anterior/Posterior | Axial |
| **Semimembranosus** | 1.03 | -6.67 | 10.78 |
| **Semitendinosus** | 2.88 | -5.35 | 3.96 |
| **Biceps femoris long head** | 2.65 | -6.64 | 10.53 |
| **Biceps femoris short head** | 1.48 | -4.63 | 13.25 |
| **Sartorius** | 6.46 | -6.12 | 3.86 |
| **TFL** | 14.33 | -47.43 | 169.35 |
| **Gracilis** | 0.66 | -1.84 | 4.03 |
| **Soleus** | -97.87 | -207.19 | -1664.85 |
| **Tibialis posterior** | 0.04 | -0.27 | -13.79 |
| **Flexor digitorum** | -0.00 | 0.01 | -0.04 |
| **Flexor hallucis** | 173.05 | 775.55 | 1881.25 |
| **Tibialis anterior** | -0.13 | -0.14 | -2.46 |
| **Peroneus brevis** | 8.27 | 11.97 | -144.89 |
| **Peroneus longus** | -60.14 | -27.05 | -542.45 |
| **Peroneus tertius** | -74.92 | -18.52 | -773.04 |
| **Extensor digitorum** | -4.51 | 6.83 | -31.85 |
| **Extensor hallucis** | -9.19 | 14.22 | -95.53 |
| **Patellar ligament** | -0.88 | 1.33 | -7.50 |
| **Ankle contact force** | 820.00 | -952.08 | 6482.52 |

# Appendix B Supplemental Information for Ch. 4

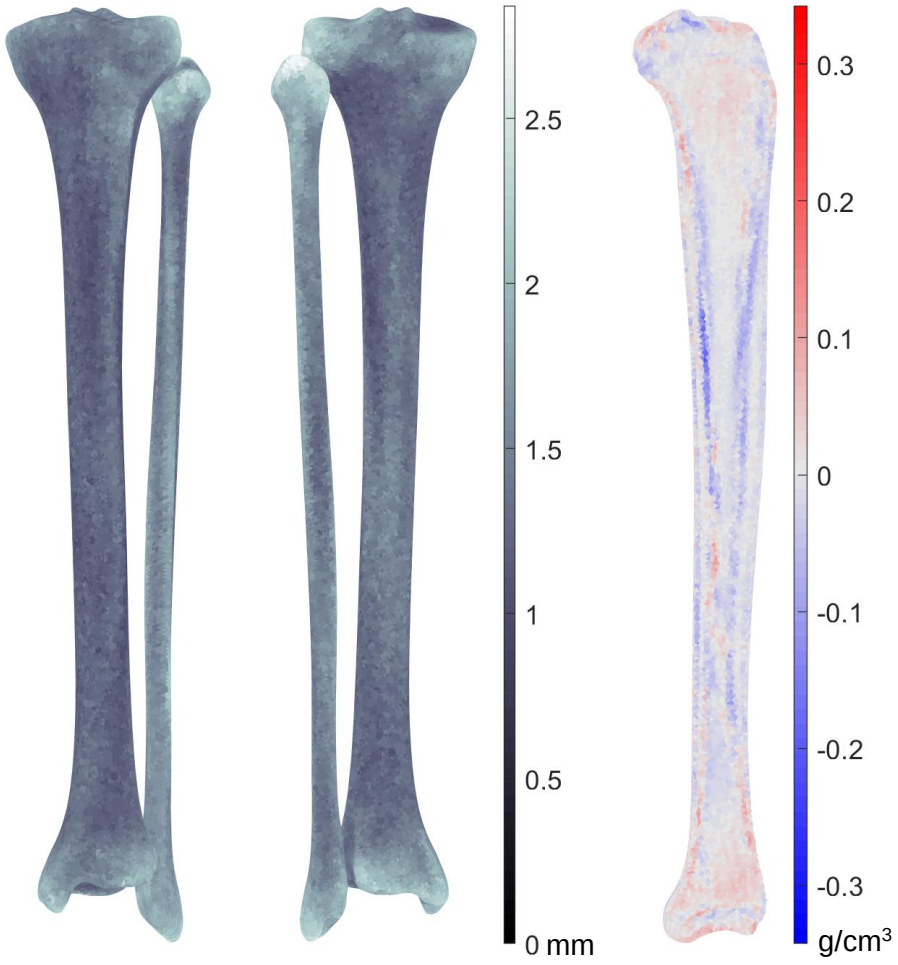


*Figure B.1 Mean surface geometry (A) and density (B) errors resulting from fitting the statistical appearance model to the validation cohort.*

Compactness, accuracy, and generalization of the tibia-fibula SAM

Compactness: the cumulative variance explained by *n* PCs.

Accuracy: a measure of how accurately the model reconstructs geometry and density of instances in the training set for a given number of PCs retained.

Generalization: a measure of how accurately the model predicts geometry and density of new individuals for a given number of PCs used to fit the model to the new data. A leave-one-out analysis and the fitting method described in Chapter 4.2.1 was performed to compute this measure.

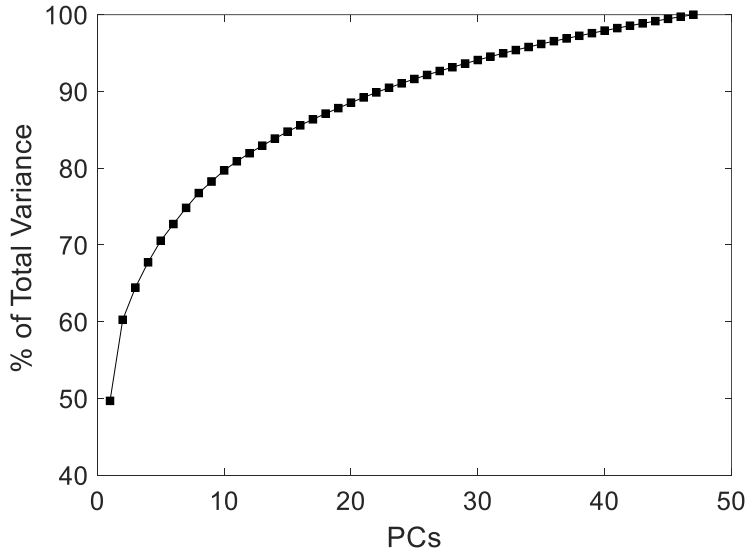


*Figure B.2 Cumulative variance by number of principal components.*

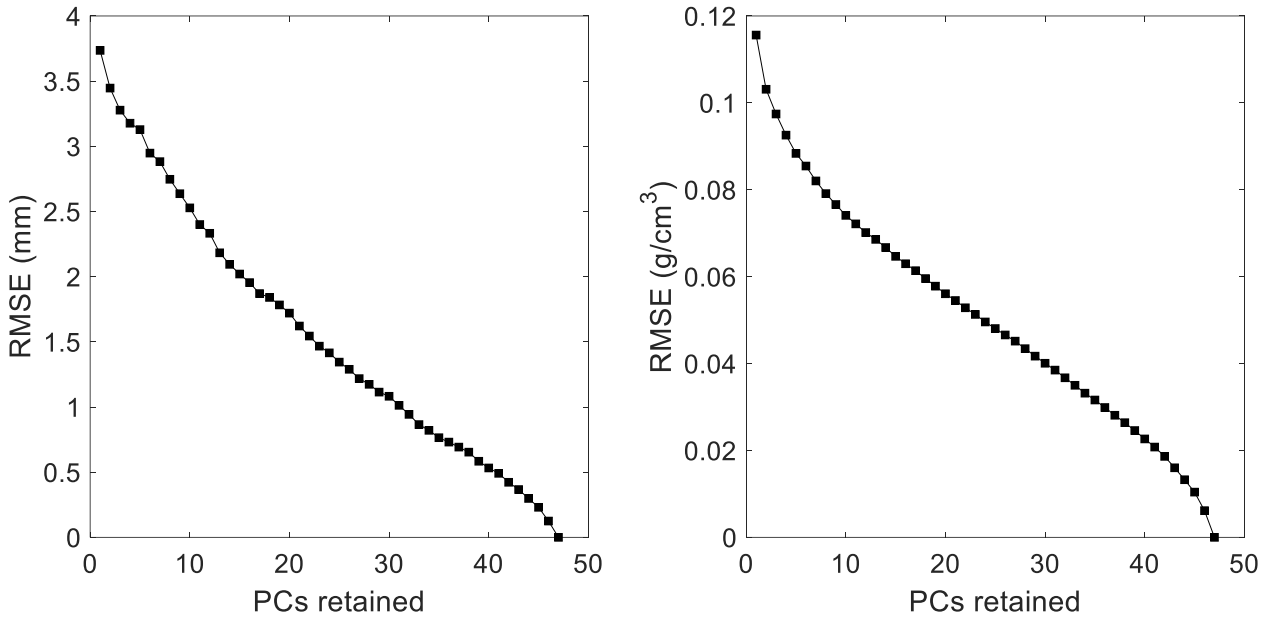


*Figure B.3 Accuracy (RMSE) of surface geometry (A) and density (B) reconstructions of individuals in the training set of the SAM by the number of PCs used to reconstruct.*

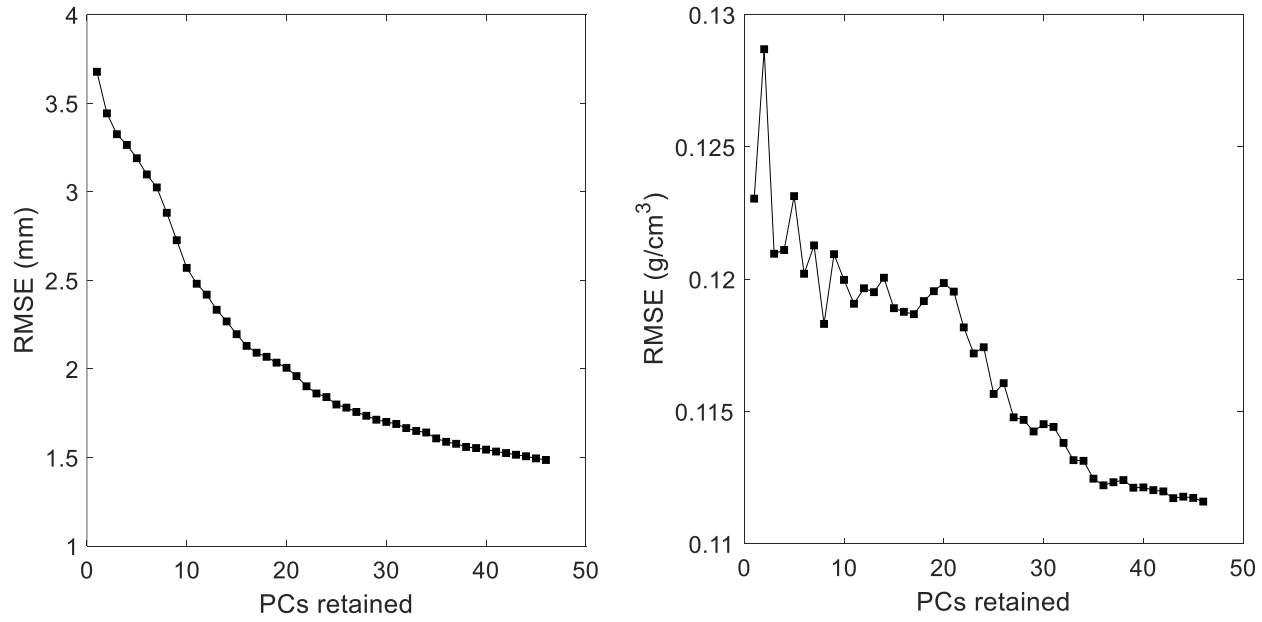


*Figure B.4 Generalization: surface geometry (A) and density (B) average prediction errors (RSME) by the number of PCs used to fit the model to new instances*

# Appendix C Supplemental Information for Ch 5

*Table C.1 Median (IQR) reconstruction error measures, calculated for the whole bone (all), or specific regions. Proximal is 0-20%, diaphysis is 20-80%, and distal is 80-100% of the length of the tibia or fibula. All Freidman ANOVAs except the proximal fibula maximum error were significant at family-wise error of p < 0.05 (critical p = 0.017). * significant difference to isotropic scaling at family-wise p < 0.05 (critical p = 0.006). ‡ significant difference between 9 and 14 landmark reconstructions at family-wise p < 0.05 (critical p = 0.006).*

| | | RMSE (mm) | | | Max (mm) | | | Jaccard | | |
|---|---|---|---|---|---|---|---|---|---|---|
| Bone(s) | Region | Scale | 9 landmarks | 14 landmarks | Scale | 9 landmarks | 14 landmarks | Scale | 9 landmarks | 14 landmarks |
| Tibia-fibula | All | 1.78 (0.62) | 1.62 (0.35) * | 1.51 (0.29) *‡ | 5.84 (2.62) | 5.12 (1.64) * | 4.82 (1.25) * | 0.792 (0.077) | 0.824 (0.038) * | 0.833 (0.034) *‡ |
| Tibia | All | 1.75 (0.72) | 1.56 (0.43)* | 1.39 (0.28)*‡ | 5.42 (2.77) | 4.86 (1.74) * | 4.57 (1.21) * | 0.835 (0.068) | 0.852 (0.043) * | 0.866 (0.035) *‡ |
| | Proximal | 1.79 (0.67) | 1.51 (0.42)* | 1.39 (0.33)* ‡ | 5.11 (1.72) | 4.41 (1.65) * | 4.1 (1.27) * | | | |
| | Diaphysis | 1.56 (0.75) | 1.41 (0.49)* | 1.32 (0.35)* ‡ | 3.73 (1.43) | 3.58 (1.28) * | 3.09 (1.10) * | | | |
| | Distal | 1.73 (1.08) | 1.35 (0.63)* | 1.34 (0.52)* | 4.53 (2.84) | 4.13 (1.64) * | 3.94 (1.50) * | | | |
| Fibula | All | 1.77 (0.62) | 1.54 (0.51) * | 1.51 (0.38) *‡ | 5.05 (1.77) | 4.57 (1.29) * | 5.59 (1.25) * | 0.627 (0.114) | 0.688 (0.122) * | 0.695 (0.091) *‡ |
| | Proximal | 1.97 (0.69) | 1.66 (0.54) * | 1.67 (0.57) * | 4.73 (1.62) | 4.32 (1.38) | 4.26 (1.26) * | | | |
| | Diaphysis | 1.67 (0.58) | 1.45 (0.64) * | 1.41 (0.45) *‡ | 3.83 (1.65) | 3.82 (1.25) | 3.5 (0.98) * | | | |
| | Distal | 1.57 (0.72) | 1.4 (0.50) * | 1.38 (0.42) * | 3.76 (1.80) | 3.66 (1.56) | 3.39 (1.43) * | | | |

*Table C.2 Mean (SD) reconstruction error measures, calculated for the whole bone (all), or specific regions. Proximal is 0-20%, diaphysis is 20-80%, and distal is 80-100% of the length of the tibia or fibula. a (RMSE), b (Max Error), c (Jaccard Index): significant ANOVA at a family-wise error of p < 0.05 (critical p = 0.017).* ***** *significant difference to isotropic scaling at family-wise p < 0.05 (critical p = 0.006). No significant difference between 9 and 14 landmark reconstructions at family-wise p < 0.05 (critical p = 0.006).*

| | | RMSE (mm) | | | Max (mm) | | | Jaccard | | |
|---|---|---|---|---|---|---|---|---|---|---|
| Bone(s) | Region | Scale | 9 landmarks | 14 landmarks | Scale | 9 landmarks | 14 landmarks | Scale | 9 landmarks | 14 landmarks |
| Tibia-fibula | All [a,b,c] | 2.78 (0.63) | 2.11 (0.31) | 2.17 (0.34) | 9.22 (2.36) | 6.91 (1.00) * | 7.04 (1.03) * | 0.672 (0.024) | 0.769 (0.010) * | 0.763 (0.012) * |
| Tibia | All [a,b,c] | 3.03 (0.69) | 2.15 (0.30) * | 2.17 (0.33) * | 9.16 (2.35) | 6.69 (0.98) * | 6.98 (1.08) * | 0.699 (0.023) | 0.799 (0.010) * | 0.796 (0.012) * |
| | Proximal [a,b] | 3.46 (0.86) | 2.34 (0.28) * | 2.38 (0.34) * | 9.16 (2.35) | 6.68 (0.99) * | 6.85 (1.10) * | | | |
| | Diaphysis [a] | 2.25 (0.66) | 1.94 (0.42) | 1.93 (0.38) | 6.09 (1.72) | 4.75 (0.98) | 4.58 (0.62) | | | |
| | Distal [a] | 3.07 (0.68) | 2.15 (0.37) * | 2.22 (0.38) * | 6.77 (1.59) | 5.69 (0.78) | 5.84 (0.93) | | | |
| Fibula | All | 2.24 (0.59) | 2.01 (0.40) | 2.13 (0.50) | 7.34 (2.16) | 6.02 (1.05) | 6.25 (0.97) | 0.526 (0.037) | 0.608 (0.020) | 0.596 (0.022) |
| | Proximal [b] | 2.55 (0.87) | 1.97 (0.42) | 2.00 (0.48) | 6.84 (2.55) | 4.76 (1.07) | 4.76 (1.05) | | | |
| | Diaphysis | 2.09 (0.66) | 1.91 (0.48) | 2.03 (0.68) | 4.75 (1.34) | 4.33 (1.15) | 4.62 (1.47) | | | |
| | Distal | 2.24 (0.55) | 2.21 (0.48) | 2.37 (0.46) | 6.17 (1.61) | 5.89 (1.13) | 5.94 (1.09) | | | |

*Table C.3 Median (IQR) Euclidian distance (mm) between muscle points on reconstructed and CT surfaces. ‡ significant difference between 9 and 14 landmark reconstructions for RMSE. No difference between SSM and isotropic scaling for RMSE of muscle points. No difference between any reconstruction method for older adults. Highlighted muscles result in non-zero moment arm differences.*

| | Young Adults | | | Old Adults | | |
|---|---|---|---|---|---|---|
| muscle | scale | 9 landmarks | 14 landmarks | scale | 9 landmarks | 14 landmarks |
| All muscle points RMSE | 5.79 (2.10) | 5.98 (3.62) | 5.36 (2.73) ‡ | 11.67 (4.55) | 11.97 (3.84) | 12.40 (3.44) |
| Semimembranosus | 4.56 (2.84) | 4.26 (3.08) | 3.41 (2.36) | 7.23 (5.86) | 7.53 (6.33) | 4.99 (6.39) |
| Semitendinosus | 3.89 (2.12) | 4.27 (2.83) | 4.02 (3.16) | 7.08 (4.16) | 8.83 (5.63) | 7.47 (5.52) |
| Biceps femoris long head | 4.20 (2.89) | 3.57 (2.04) | 3.69 (2.21) | 4.03 (3.19) | 4.12 (2.49) | 3.51 (1.60) |
| Biceps femoris short head | 4.82 (2.89) | 3.73 (2.42) | 3.98 (2.58) | 4.07 (3.27) | 3.88 (1.94) | 4.10 (1.16) |
| Sartorius | 5.37 (3.28) | 5.33 (4.35) | 4.36 (3.90) | 9.13 (6.59) | 10.22 (6.43) | 9.20 (7.01) |
| Tensor fasciae latae | 3.21 (2.51) | 2.99 (2.66) | 2.83 (2.41) | 7.31 (2.61) | 6.23 (2.48) | 6.08 (1.57) |
| Gracilis | 3.65 (2.06) | 4.03 (2.56) | 3.41 (2.20) | 6.68 (3.80) | 7.02 (6.81) | 6.53 (5.56) |
| Soleus | 3.47 (1.92) | 3.76 (3.41) | 3.38 (2.36) | 9.95 (6.11) | 11.46 (6.77) | 11.58 (6.11) |
| Tibialis posterior | 4.58 (3.00) | 5.10 (5.09) | 4.69 (4.74) | 17.20 (8.13) | 17.39 (6.26) | 18.49 (8.06) |
| Flexor digitorum | 5.04 (3.92) | 5.32 (6.65) | 4.75 (4.65) | 14.10 (9.34) | 11.22 (12.97) | 13.09 (8.63) |
| Flexor hallucis | 7.85 (6.14) | 7.52 (6.67) | 6.10 (5.32) | 10.02 (6.80) | 10.48 (7.32) | 10.89 (10.88) |
| Tibialis anterior | 5.74 (4.61) | 5.61 (4.15) | 5.41 (4.11) | 21.68 (10.84) | 20.00 (14.20) | 19.34 (14.37) |
| Peroneus brevis | 8.04 (3.92) | 6.54 (6.12) | 6.29 (4.50) | 5.14 (8.89) | 5.55 (10.75) | 5.59 (8.39) |
| Peroneus longus | 5.12 (5.06) | 6.64 (7.04) | 3.91 (3.88) | 9.59 (11.47) | 7.90 (12.18) | 14.62 (15.52) |
| Peroneus tertius | 7.52 (5.16) | 6.04 (7.43) | 6.57 (4.20) | 5.67 (13.80) | 6.37 (16.11) | 5.61 (12.72) |
| Extensor digitorum | 4.62 (4.16) | 6.06 (5.63) | 4.27 (4.19) | 8.48 (10.01) | 6.52 (11.06) | 13.67 (11.68) |
| Extensor hallucis | 5.09 (5.43) | 6.46 (6.55) | 4.54 (4.84) | 7.34 (13.63) | 5.59 (12.52) | 12.72 (15.56) |
| Patellar ligament | 3.95 (2.23) | 4.35 (3.22) | 3.79 (2.55) | 7.71 (3.50) | 8.36 (7.20) | 7.48 (4.91) |

*Table C.4 Median (IQR) of maximum difference (mm) in moment arm compared to CT-based subject-specific model through physiologic range of motion. [a] Freidman's ANOVA significant for the young adult group. [b] Repeated measures ANOVA significant for the old adult group. * significant difference to isotropic scaling at family-wise p < 0.05 (critical p = 0.008). ‡ significant difference between 9 and 14 landmark reconstructions.*

| | Young Adults | | | Old Adults | | |
|---|---|---|---|---|---|---|
| Muscle | Scale | 9 Landmarks | 14 Landmarks | Scale | 9 Landmarks | 14 Landmarks |
| Semimembranosus [a] | 3.47 (2.65) | 3.09 (2.24) | 2.61 (1.46) *‡ | 8.33 (4.92) | 7.98 (6.02) | 7.49 (3.58) |
| Biceps Femoris Long Head [a] | 3.65 (2.90) | 2.36 (1.90) * | 2.45 (2.08) * | 5.99 (6.43) | 4.76 (5.74) | 5.99 (5.12) |
| Biceps Femoris Short Head [a] | 3.99 (3.14) | 3.01 (2.06) * | 2.74 (2.34) * | 7.25 (8.20) | 6.04 (7.12) | 6.79 (6.52) |
| Tensor Fasciae Latae | 0.66 (0.73) | 0.63 (0.76) | 0.60 (0.80) | 1.02 (0.98) | 1.02 (1.54) | 1.32 (1.01) |
| Soleus | 0.13 (0.15) | 0.09 (0.17) | 0.10 (0.16) | 0.27 (0.30) | 0.25 (0.43) | 0.31 (0.37) |
| Patellar Ligament | 0.41 (0.41) | 0.44 (0.60) | 0.40 (0.55) | 1.10 (1.38) | 0.71 (0.93) | 0.70 (1.27) |

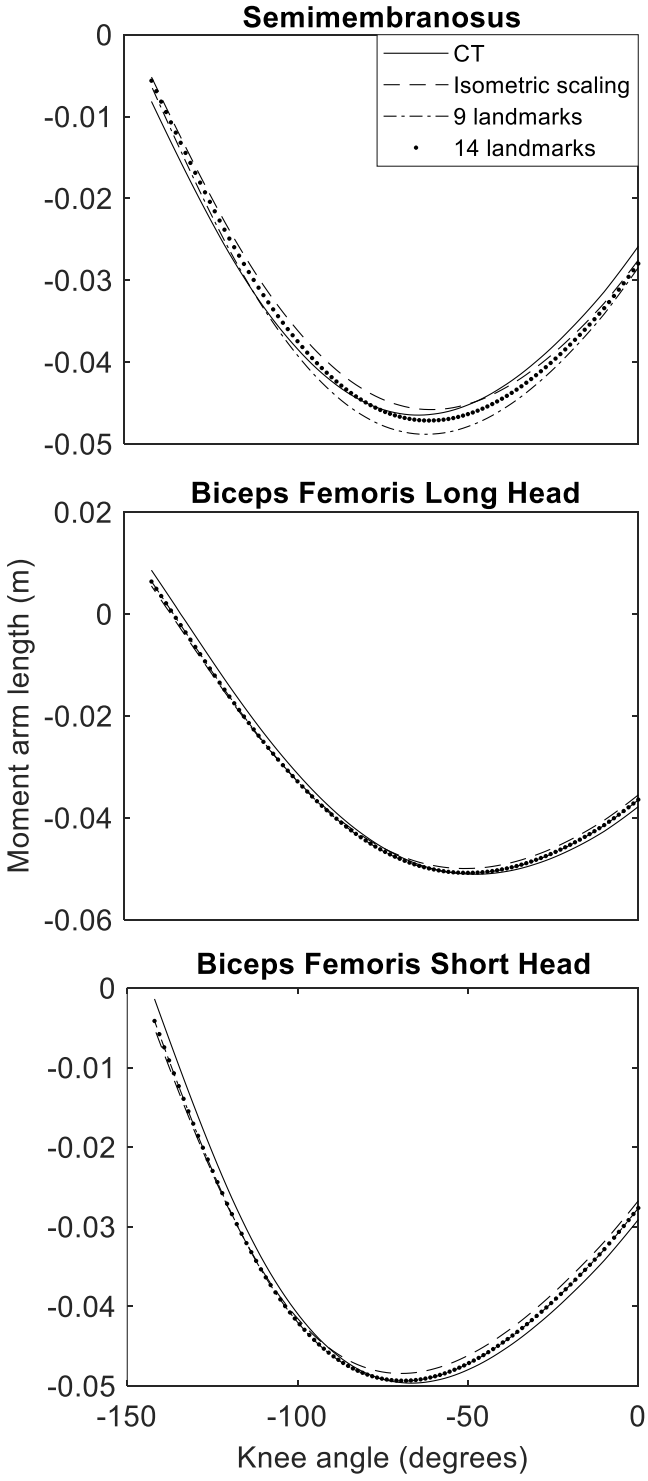


*Figure C.1 Comparison of muscle moment arms in the sagittal plane as a function of knee angle between models defined by CT, isotropically scaled average, and SSM reconstructed geometries (representative example).*

# Appendix D Supplemental Information for Ch 6

## D1. Characterizing the relationship between height and the first principal component score

A linear regression was calculated to characterise the relationship between participant height and the first principal component score for the statistical appearance model training set. The relationship was strong ($r^2 = 0.82$).

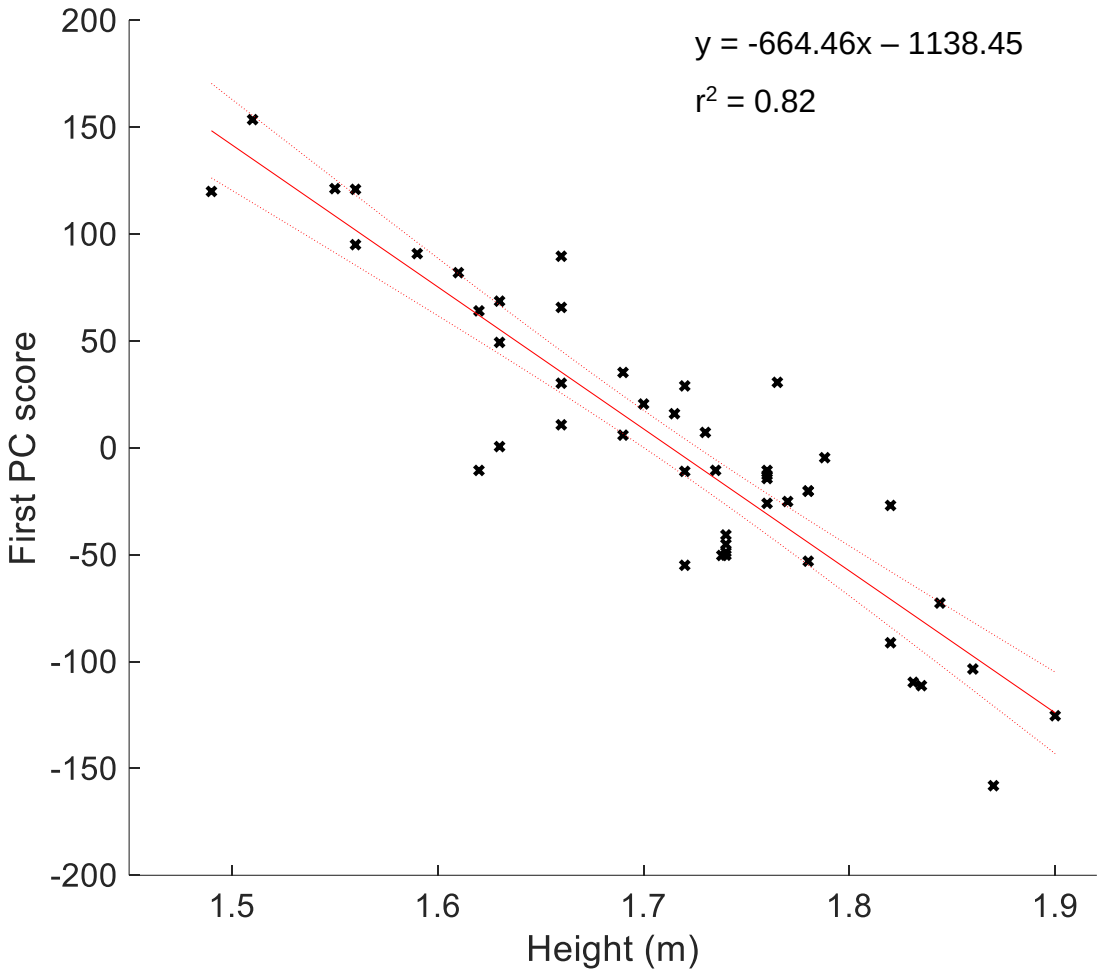


*Figure D.1 Relationship between height and the first principal component score. Negative principal component scores correspond with greater tibia and fibula size.*

**D2. Geometry and density prediction accuracy when participant-specific marker offsets are known**

Tibial-fibular geometry and density distribution were predicted from skin-mounted landmarks and one to five cumulative principal components. To enable use of exact offset vectors between skin mounted landmarks and corresponding landmarks on the bone surface, markers placed and imaged during the CT session were used. The statistical appearance model was morphed along the principal components and rigidly transformed to match the morphed model to the target landmarks. An initial guess for the first principal component was calculated from height. All other principal component scores were initialised as zeroes. The optimization minimized a negative log likelihood function of a Gaussian distribution:

$$D = -0.5log\sigma^2 \sum_{i=1} \frac{d_i^2}{2\sigma_i^2}$$

where σ is the standard deviation of skin-mounted marker offsets, and $d_i$ is the distance between the target landmark and the model landmark. The position of the model landmark was calculated as the position of the bone surface landmark on the model, projected along *the participant-specific offset vector*. Geometry and density distribution RMSEs relative to the participant-specific meshes were calculated.

Friedman tests were used to evaluate differences in RMSE between reconstructions from one through five principal components. When differences were found Wilcoxon signed-rank tests with Bonferroni corrections were used to test differences between pairs of reconstructions.

Geometry RMSE was statistically smaller in predictions from five principal components when compared to predictions using one and two principal components. Density RMSE was not different between predictions from one through five principal components ($p = 0.653$). Reducing soft tissue offset and marker placement uncertainties by using known personalized offset vectors

reduced prediction errors. However, the improvement from using principal components describing geometry changes (principal components 2-5) was so small as to be negligible. Some uncertainty in soft tissue offsets remained in this analysis due to the cost function used. The geometry information provided by the landmarks appears to be limited and insufficient to overcome even reduced uncertainties in soft tissue offsets.

*Table D.1 Median (IQR) RMSE for predictions from landmarks with personalized offset vectors.*

| *RMSE* | *1 PC* | *2 PCs* | *3 PCs* | *4 PCs* | *5 PCs* |
|---|---|---|---|---|---|
| *Geometry* | 3.75 | 3.73 | 3.76 | 3.74 | 3.71 |
| *(mm)* | (1.25)* | (1.15)* | (1.59) | (1.49) | (1.50) |
| *Density* | 0.152 | 0.157 | 0.159 | 0.156 | 0.159 |
| *($g/cm^3$)* | (0.036) | (0.055) | (0.040) | (0.037) | (0.043) |

* Significantly different than error from reconstructions using 5 cumulative principal components (PC) ($p \leq 0.001$, critical $p = 0.005$)

**D3. Between-day intra-rater reliability**

Participants attended two sessions: motion capture and CT. At both sessions markers were attached to the skin with tape at twelve landmarks on the tibia and fibula. In addition to the predictions from landmarks from the motion capture collection described in the paper, predictions were also generated using the landmark set from the CT session. Markers were segmented in the CT images and the centroid of each was calculated. CT and motion capture marker sets were aligned using a Procrustes analysis, excluding markers that were allowed to move (tibial crest markers, fibula diaphysis, and tibial notch). RMSE error between the aligned CT and motion capture marker sets was then calculated.

Tibial-fibular geometry was predicted using the same method described in the main study. Tibia-fibula geometry and density were predicted by morphing the statistical appearance model along the first one to five principal components and performing rigid-body transformations to match the morphed model to the target landmarks. An initial guess for the first principal component was calculated from height. All other principal component scores were initialised as zeroes. The optimization was performed using the BFGS algorithm in MATLAB, minimizing a negative log likelihood function of a Gaussian distribution (Nolte et al. 2020):

$$D = -0.5log\sigma^2 \sum_{i=1} \frac{d_i^2}{2\sigma_i^2}$$

where σ is the standard deviation of skin-mounted marker offsets, and $d_i$ is the distance between the target landmark and the model landmark. The position of the model landmark was calculated as the position of the bone surface landmark on the model, projected along the mean offset vector by the mean offset magnitude and marker radius.

Geometry and density distribution RMSEs relative to the participant-specific mesh and relative to the motion capture marker set-based prediction were calculated. Intra-class correlation

coefficients were calculated to evaluate the reliability of prediction errors relative to participant specific meshes between predictions based on the CT and motion capture marker sets.

Median (IQR) RMSE for landmark placement between days was 9.5 (4.4) mm. Variations in marker placement between days resulted in differences in predicted geometry and densities. Median RMSE between predicted geometries were 3.9 – 4.1 mm. Median RMSE between predicted apparent density distributions were 0.008 – 0.050 g/cm$^3$. Geometry and density RMSEs illustrated only moderate agreement between days (ICC $R^2$= 0.45 – 0.64).

*Table D.2 Median (IQR) RMSE for predictions from one through five principal components (PCs) using marker sets from the motion capture and CT sessions.*

| *RMSE* | *1 PC* | *2 PCs* | *3 PCs* | *4 PCs* | *5 PCs* |
|---|---|---|---|---|---|
| *Geometry (mm)* | | | | | |
| *Motion capture markers* | 4.39 (1.68) | 4.55 (1.45) | 4.63 (1.48) | 4.75 (1.78) | 4.67 (1.97) |
| *CT markers* | 4.15 (1.64) | 3.99 (1.41) | 4.67 (1.75) | 4.54 (1.20) | 4.48 (2.09) |
| *ICC* | 0.64 | 0.59 | 0.56 | 0.45 | 0.56 |
| *Density (g/cm$^3$)* | | | | | |
| *Motion capture markers* | 0.118 (0.046) | 0.127 (0.056) | 0.127 (0.049) | 0.135 (0.045) | 0.142 (0.054) |
| *CT markers* | 0.153 (0.036) | 0.155 (0.060) | 0.161 (0.045) | 0.164 (0.045) | 0.167 (0.049) |
| *ICC* | 0.60 | 0.49 | 0.45 | 0.59 | 0.47 |

# Appendix E Manuscript Publisher Rights and Permissions

The manuscript presented in Chapter 3 was published in an Elsevier journal. The manuscript presented in Chapter 4 has been submitted to the same Elsevier journal. These manuscripts do not require specific permission to be included in the thesis, per the guidelines below.

Overview | Author rights | Institution rights | Government rights | Find out more

| Author rights in Elsevier's proprietary journals | Published open access | Published subscription |
|---|---|---|
| Retain patent and trademark rights | √ | √ |
| Retain the rights to use their research data freely without any restriction | √ | √ |
| Receive proper attribution and credit for their published work | √ | √ |
| Re-use their own material in new works without permission or payment (with full acknowledgement of the original article):<br>1. Extend an article to book length<br>2. Include an article in a subsequent compilation of their own work<br>3. Re-use portions, excerpts, and their own figures or tables in other works. | √ | √ |
| Use and share their works for scholarly purposes (with full acknowledgement of the original article):<br>1. In their own classroom teaching. Electronic and physical distribution of copies is permitted<br>2. If an author is speaking at a conference, they can present the article and distribute copies to the attendees<br>3. Distribute the article, including by email, to their students and to research colleagues who they know for their personal use<br>4. Share and publicize the article via Share Links, which offers 50 days' free access for anyone, without signup or registration<br>5. Include in a thesis or dissertation (provided this is not published commercially)<br>6. Share copies of their article privately as part of an invitation-only work group on commercial sites with which the publisher has a hosting agreement | √ | √ |
| Publicly share the preprint on any website or repository at any time. | √ | √ |
| Publicly share the accepted manuscript on non-commercial sites | √ | √ using a CC BY-NC-ND license and usually only after an embargo |

The manuscript presented in Chapter 5 was published in a Taylor & Francis journal and does not require specific permission to be included in the thesis, per the guidelines below.

## Copyright at Taylor & Francis

To publish an article and make it available, we need publishing rights from you for that work. We therefore ask authors publishing in one of our journals to sign an author contract which grants us the necessary publishing rights. This will be after your manuscript has been through the peer-review process, been accepted and moves into production. Our Production team will then send you an email with all the details.

Expert tips and guidance on getting published and maximizing the impact of your research. Register now for weekly insights direct to your inbox.

Sign up to Research Insights today

## Standard articles in subscription journals

There are two main options for authors publishing a (non open access) article in a subscription journal. These are copyright assignment or exclusive license to publish.

## 1. Copyright assignment

In our standard author contract, you transfer – or "assign" – copyright to us as the owner and publisher of the journal (or, in the case of a society-owned journal, to that learned society).

After assigning copyright, you will still retain the right to:

- Be credited as the author of the article.
- Make printed copies of your article to use for a lecture or class that you are leading on a non-commercial basis.
- Share your article using your free eprints with friends, colleagues and influential people you would like to read your work.
- Include your article in your thesis or dissertation.
- Present your article at a meeting or conference and distribute printed copies of the article on a non-commercial basis.
- Post the Author's Original Manuscript (AOM)/Accepted Manuscript (AM) on a departmental, personal website or institutional repositories depending

on embargo period. To find the embargo period for any Taylor & Francis journal, please use the Open Access Options Finder.

- For more information about manuscript versions and how you can use them, please see our guide to sharing your work.

# Appendix F Figure reproduction permissions

Figure 2.1:

## Order Completed

Thank you for your order.

This Agreement between Olivia Bruce ("You") and Elsevier ("Elsevier") consists of your license details and the terms and conditions provided by Elsevier and Copyright Clearance Center.

Your confirmation email will contain your order number for future reference.

| | |
|---|---|
| License Number | 5503701099297 |
| License date | Mar 07, 2023 |

Printable Details

### Licensed Content

| | |
|---|---|
| Licensed Content Publisher | Elsevier |
| Licensed Content Publication | Medical Engineering & Physics |
| Licensed Content Title | Mechanical properties and the hierarchical structure of bone |
| Licensed Content Author | Jae-Young Rho,Liisa Kuhn-Spearing,Peter Zioupos |
| Licensed Content Date | Mar 1, 1998 |
| Licensed Content Volume | 20 |
| Licensed Content Issue | 2 |
| Licensed Content Pages | 11 |

### Order Details

| | |
|---|---|
| Type of Use | reuse in a thesis/dissertation |
| Portion | figures/tables/illustrations |
| Number of figures/tables/illustrations | 1 |
| Format | electronic |
| Are you the author of this Elsevier article? | No |
| Will you be translating? | No |

Figure 2.2:

Thank you for your order.

This Agreement between Olivia Bruce ("You") and Elsevier ("Elsevier") consists of your license details and the terms and conditions provided by Elsevier and Copyright Clearance Center.

Your confirmation email will contain your order number for future reference.

| | |
|---|---|
| License Number | 5503340876150 |
| License date | Mar 06, 2023 |

Printable Details

## Licensed Content

| | |
|---|---|
| Licensed Content Publisher | Elsevier |
| Licensed Content Publication | Journal of Biomechanics |
| Licensed Content Title | Uniaxial fatigue of human cortical bone. The influence of tissue physical characteristics |
| Licensed Content Author | Dennis R. Carter,William E. Caler,Dan M. Spengler,Victor H. Frankel |
| Licensed Content Date | Jan 1, 1981 |
| Licensed Content Volume | 14 |
| Licensed Content Issue | 7 |
| Licensed Content Pages | 10 |

## Order Details

| | |
|---|---|
| Type of Use | reuse in a thesis/dissertation |
| Portion | figures/tables/illustrations |
| Number of figures/tables/illustrations | 1 |
| Format | electronic |
| Are you the author of this Elsevier article? | No |
| Will you be translating? | No |

# Appendix G Manuscript Author Permissions

To whom it may concern,

I give permission to Olivia Bruce to include the manuscripts below, for which I am co-author, in her thesis: "*Tibial-fibular morphology: Variations, sexual dimorphism, and mechanical implications*."

- ✓ Bruce, O.L., Baggaley, M., Khassetarash, A., Haider, I.T., Edwards, W.B. (2022). Tibial-fibular geometry and density variations associated with elevated bone strain and sex disparities in young active adults. Bone. doi: 10.1016/j.bone.2022.116443

- ☐ Bruce, O.L., Edwards, W.B. Sex disparities in tibia-fibula geometry and density are associated with elevated bone strain in females: A cross- validation study. *Submitted to Bone.*

- ☐ Bruce, O.L., Baggaley, M., Welte, L., Rainbow, M.J., Edwards, W.B. (2021). A statistical shape model of the tibia-fibula complex: sexual dimorphism and effects of age on reconstruction accuracy from anatomical landmarks. Computer Methods in Biomechanics and Biomedical Engineering. doi: 10.1080/10255842.2021.1985111

- ☐ Bruce, O.L., Tu, J., Edwards, W.B. Predicting tibia-fibula geometry and density from anatomical landmarks: influence of errors on finite element-calculated bone strain. *In preparation for submission to the Journal of Biomechanics.*

Signatu[redacted]

Name: Arash Khassetarash

Date: March 8, 2023

To whom it may concern,

I give permission to Olivia Bruce to include the manuscripts below, for which I am co-author, in her thesis: "*Tibial-fibular morphology: Variations, sexual dimorphism, and mechanical implications*."

- ☐ Bruce, O.L., Baggaley, M., Khassetarash, A., Haider, I.T., Edwards, W.B. (2022). Tibial-fibular geometry and density variations associated with elevated bone strain and sex disparities in young active adults. Bone. doi: 10.1016/j.bone.2022.116443

- ☐ Bruce, O.L., Edwards, W.B. Sex disparities in tibia-fibula geometry and density are associated with elevated bone strain in females: A cross- validation study. *Submitted to Bone.*

- ☐ Bruce, O.L., Baggaley, M., Welte, L., Rainbow, M.J., Edwards, W.B. (2021). A statistical shape model of the tibia-fibula complex: sexual dimorphism and effects of age on reconstruction accuracy from anatomical landmarks. Computer Methods in Biomechanics and Biomedical Engineering. doi: 10.1080/10255842.2021.1985111

- ✓ Bruce, O.L., Tu, J., Edwards, W.B. Predicting tibia-fibula geometry and density from anatomical landmarks: influence of errors on finite element-calculated bone strain. *In preparation for submission to the Journal of Biomechanics.*

Signature: [redacted]

Name: Jean Tu

Date: March 9, 2023

To whom it may concern,

I give permission to Olivia Bruce to include the manuscripts below, for which I am co-author, in her thesis: "*Tibial-fibular morphology: Variations, sexual dimorphism, and mechanical implications*."

- ✓ Bruce, O.L., Baggaley, M., Khassetarash, A., Haider, I.T., Edwards, W.B. (2022). Tibial-fibular geometry and density variations associated with elevated bone strain and sex disparities in young active adults. Bone. doi: 10.1016/j.bone.2022.116443

- □ Bruce, O.L., Edwards, W.B. Sex disparities in tibia-fibula geometry and density are associated with elevated bone strain in females: A cross- validation study. *Submitted to Bone.*

- □ Bruce, O.L., Baggaley, M., Welte, L., Rainbow, M.J., Edwards, W.B. (2021). A statistical shape model of the tibia-fibula complex: sexual dimorphism and effects of age on reconstruction accuracy from anatomical landmarks. Computer Methods in Biomechanics and Biomedical Engineering. doi: 10.1080/10255842.2021.1985111

- □ Bruce, O.L., Tu, J., Edwards, W.B. Predicting tibia-fibula geometry and density from anatomical landmarks: influence of errors on finite element-calculated bone strain. *In preparation for submission to the Journal of Biomechanics.*

Signature: 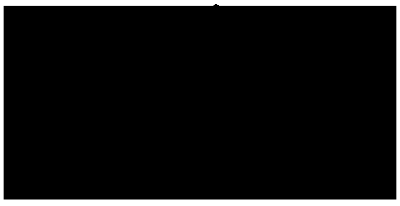

Name: Ifaz Haider

Date: March 13, 2023

To whom it may concern,

I give permission to Olivia Bruce to include the manuscripts below, for which I am co-author, in her thesis: “Tibial-fibular morphology: Variations, sexual dimorphism, and mechanical implications.”

-  Bruce, O.L., Baggaley, M., Khassetarash, A., Haider, I.T., Edwards, W.B. (2022). Tibial-fibular geometry and density variations associated with elevated bone strain and sex disparities in young active adults. Bone. doi: 10.1016/j.bone.2022.116443
-  Bruce, O.L., Edwards, W.B. Sex disparities in tibia-fibula geometry and density are associated with elevated bone strain in females: A cross- validation study. *Submitted to Bone.*
- ✓ Bruce, O.L., Baggaley, M., Welte, L., Rainbow, M.J., Edwards, W.B. (2021). A statistical shape model of the tibia-fibula complex: sexual dimorphism and effects of age on reconstruction accuracy from anatomical landmarks. Computer Methods in Biomechanics and Biomedical Engineering. doi: 10.1080/10255842.2021.1985111
-  Bruce, O.L., Tu, J., Edwards, W.B. Predicting tibia-fibula geometry and density from anatomical landmarks: influence of errors on finite element-calculated bone strain. *In preparation for submission to the Journal of Biomechanics.*

Signature:

Name: Lauren Welte

Date: March 13, 2023

To whom it may concern,

I give permission to Olivia Bruce to include the manuscripts below, for which I am co-author, in her thesis: "*Tibial-fibular morphology: Variations, sexual dimorphism, and mechanical implications.*"

- ✓ Bruce, O.L., Baggaley, M., Khassetarash, A., Haider, I.T., Edwards, W.B. (2022). Tibial-fibular geometry and density variations associated with elevated bone strain and sex disparities in young active adults. Bone. doi: 10.1016/j.bone.2022.116443

- ✓ Bruce, O.L., Edwards, W.B. Sex disparities in tibia-fibula geometry and density are associated with elevated bone strain in females: A cross- validation study. *Submitted to Bone.*

- ✓ Bruce, O.L., Baggaley, M., Welte, L., Rainbow, M.J., Edwards, W.B. (2021). A statistical shape model of the tibia-fibula complex: sexual dimorphism and effects of age on reconstruction accuracy from anatomical landmarks. Computer Methods in Biomechanics and Biomedical Engineering. doi: 10.1080/10255842.2021.1985111

- ✓ Bruce, O.L., Tu, J., Edwards, W.B. Predicting tibia-fibula geometry and density from anatomical landmarks: influence of errors on finite element-calculated bone strain. *In preparation for submission to the Journal of Biomechanics.*

Signature: 

Name: W. Brent Edwards

Date: March 15, 2023

To whom it may concern,

I give permission to Olivia Bruce to include the manuscripts below, for which I am co-author, in her thesis: "Tibial-fibular morphology: Variations, sexual dimorphism, and mechanical implications."

- ✓ Bruce, O.L., Baggaley, M., Khassetarash, A., Haider, I.T., Edwards, W.B. (2022). Tibial-fibular geometry and density variations associated with elevated bone strain and sex disparities in young active adults. Bone. doi: 10.1016/j.bone.2022.116443

- ☐ Bruce, O.L., Edwards, W.B. Sex disparities in tibia-fibula geometry and density are associated with elevated bone strain in females: A cross- validation study. *Submitted to Bone.*

- ✓ Bruce, O.L., Baggaley, M., Welte, L., Rainbow, M.J., Edwards, W.B. (2021). A statistical shape model of the tibia-fibula complex: sexual dimorphism and effects of age on reconstruction accuracy from anatomical landmarks. Computer Methods in Biomechanics and Biomedical Engineering. doi: 10.1080/10255842.2021.1985111

- ☐ Bruce, O.L., Tu, J., Edwards, W.B. Predicting tibia-fibula geometry and density from anatomical landmarks: influence of errors on finite element-calculated bone strain. *In preparation for submission to the Journal of Biomechanics.*

Signature: 

Name: Michael Baggaley

To whom it may concern,

I give permission to Olivia Bruce to include the manuscripts below, for which I am co-author, in her thesis: "Tibial-fibular morphology: Variations, sexual dimorphism, and mechanical implications."

- ☐ Bruce, O.L., Baggaley, M., Khassetarash, A., Haider, I.T., Edwards, W.B. (2022). Tibial-fibular geometry and density variations associated with elevated bone strain and sex disparities in young active adults. Bone. doi: 10.1016/j.bone.2022.116443

- ☐ Bruce, O.L., Edwards, W.B. Sex disparities in tibia-fibula geometry and density are associated with elevated bone strain in females: A cross- validation study. *Submitted to Bone.*

- ✓ Bruce, O.L., Baggaley, M., Welte, L., Rainbow, M.J., Edwards, W.B. (2021). A statistical shape model of the tibia-fibula complex: sexual dimorphism and effects of age on reconstruction accuracy from anatomical landmarks. Computer Methods in Biomechanics and Biomedical Engineering. doi: 10.1080/10255842.2021.1985111

- ☐ Bruce, O.L., Tu, J., Edwards, W.B. Predicting tibia-fibula geometry and density from anatomical landmarks: influence of errors on finite element-calculated bone strain. *In preparation for submission to the Journal of Biomechanics.*

Signature: [redacted]

Name: Michael Rainbow

Date: May 1, 2023